SYNTHESIS OF VINYL ACETATE ON
PALLADIUM-BASED CATALYSTS

A Dissertation

by

DHEERAJ KUMAR

Submitted to the Office of Graduate Studies of
Texas A&M University
in partial fulfillment of the requirements for the degree of

DOCTOR OF PHILOSOPHY

August 2006

Major Subject: Chemistry

SYNTHESIS OF VINYL ACETATE ON PALLADIUM-BASED CATALYSTS

A Dissertation

by

DHEERAJ KUMAR

Submitted to the Office of Graduate Studies of
Texas A&M University
in partial fulfillment of the requirements for the degree of

DOCTOR OF PHILOSOPHY

Approved by:

Chair of Committee,	David W. Goodman
Committee Members,	Simon W. North
	Michael P. Rosynek
	Donald G. Naugle
Head of Department,	Emile A. Schweikert

August 2006

Major Subject: Chemistry

ABSTRACT

Synthesis of Vinyl Acetate on Palladium-Based Catalysts. (August 2006)

Dheeraj Kumar,

B.S.; M.S., Indian Institute of Technology, Mumbai (India)

Chair of Advisory Committee: Dr. David W. Goodman

Vinyl acetate (VA) is an important monomer used in the production of paints, surface coatings and adhesives. Synthesis of VA is usually carried out over supported Pd alloy catalysts with a selectivity as high as 96% and described as

$$C_2H_4 + CH_3COOH + \frac{1}{2} O_2 \rightarrow C_2H_3OOCCH_3 + H_2O$$

Although the VA synthesis reaction has been industrially carried out for many years, the nature of the active sites and the reaction mechanism is still unclear. The goal of this study was to acquire a fundamental understanding of the VA reaction mechanism by carrying out detailed kinetic and spectroscopic investigations on single crystals and supported Pd catalysts, and to detail the role of alloying in optimizing the selectivity of this important industrial reaction.

A combination of surface science techniques and kinetic measurements has been used to address the mechanism. Supported catalysts, 1 wt% Pd/SiO_2 and 5 wt% Pd/SiO_2, and 1 wt% Pd–0.5 wt% Au/SiO_2, were prepared by an incipient wet-impregnation method and characterized using XRD and TEM. On Pd-only catalysts the reaction rates were found to be: Pd(100) < 5 wt% Pd/SiO_2 (d_{pd} = 4.2 nm) < 1 wt% Pd/SiO_2 (d_{pd} = 2.5 nm). Particle size-dependence of the reaction rates is evident for the Pd-only catalysts, which suggests a degree of structure sensitivity of the reaction. There is an increased availability of uncoordinated, edge atoms on small particles. With a Pd single crystal, fewer less-coordinated surface sites are present compared to a comparable area on a small Pd particle on a supported Pd catalyst.

The formation of Pd carbide (PdC_x) during the synthesis of VA was investigated over Pd/SiO_2 catalysts with two different Pd particle sizes, as well as over a $Pd-Au/SiO_2$ mixed-metal catalyst. XRD data indicate that smaller Pd particles show greater resistance to the formation of PdC_x. The alloying of Au with Pd is apparently very effective in preventing PdC_x formation in Pd-based catalysts for VA synthesis.

Addition of Au to Pd/SiO_2 catalysts significantly enhances the VA formation rate and selectivity. Infrared reflection absorption spectroscopy (IRAS) of CO on Pd/Au(100) and Pd/Au(111) confirms the presence of Pd as isolated monomers on a Au-rich surface. A pair of Pd monomers is the most favorable active site for the formation of VA. The spacing between the two active isolated Pd atoms is critical and is demonstrated by the relative rates of VA formation on Pd/Au model catalysts, i.e. Pd/Au(111) < Pd/Au(100). The role of Au is to isolate the surface Pd atoms and thus suppress the formation of by products, CO and CO_2. A pair of Pd monomers required for VA synthesis is further confirmed by the results from model studies of Sn-Pd.

ACKNOWLEDGEMENTS

When I began my Ph.D. I asked my friend his opinion of a doctorate degree. He said "Cold, long and dark roller-coaster tunnel". I would like to thank Dr. D.W. Goodman whose direction, light and insight made this "tunnel" a freeway. I value him not only for his constant support, confidence and counsel but also for his philosophy about many aspects of scientific endeavor. His enthusiasm and clarity to think ahead will always remain an inspiration to me.

I would like to express my gratitude to Dr. M.S. Chen (for his time, patience and support in solving numerous problems and methodical scientific writing), Dr. Y.-F. Han (for teaching me several aspects of heterogeneous catalysis), Dr. T.V. Choudhary (for the inspiration and constant support), T. Wei, Dr. C.-W. Yi, Dr. E. Ozensoy, K.K. Gath, K. Luo, F. Yang, S. Axnanda, Dr. W. Wallace, Z. Yan, Y. Cai, P. Boopalachandran, Dr. S. Lee, Dr. P. Han, M. Lundwall, Dr. J. Stultz, Dr. C. Sivadinarayana and Dr. B.K. Min for their help, support and camaraderie during this work. A special thanks to A. Liu, the administrative assistant of our group for making a lot of things very easy. Also, I would like to thank A. Montalbano and K. Greer of the machine-shop, M.L. Tullos of the electronics shop and W.C. Merka III of the glass-shop for their help.

I am indebted to my mom, dad, my brother Prasanna and his wife Aditi who have always been there for me through steady encouragement and total love. Finally, I would like to thank my wife Charu Agrawal for her energy, enthusiasm, unconditional love and many long fruitful discussions about everything. These people at all times gave me a good reason to smile and look forward with cheerful optimism.

TABLE OF CONTENTS

Page

INTRODUCTION....................1

- Heterogeneous and Model Catalysts....................1
- Vinyl Acetate Synthesis....................6

EXPERIMENTAL....................8

- Model Catalysts....................8
  - Ultrahigh Vacuum (UHV) Chamber....................8
  - Surface Science Techniques....................10
    - X-ray Photoelectron Spectroscopy (XPS)....................11
    - Auger Electron Spectroscopy (AES)....................14
    - Infrared Reflection Absorption Spectroscopy (IRAS)....................16
    - Low Energy Ion Scattering Spectroscopy (LEISS)....................19
    - Temperature Programmed Desorption (TPD)....................20
  - Sample Preparation, Performing Reactions and Gas Handling....................22
  - Gas Chromatography....................23
    - Flame Ionization Detector (FID)....................24
    - Thermal Conductivity Detector (TCD)....................26
    - Methanizer....................26
- Supported Catalysts....................28
  - Preparation and the Reactants....................28
  - Characterization Techniques....................29
    - X-ray Diffraction (XRD)....................29
    - Transmission Electron Microscopy (TEM)....................30
  - Calculations of the Reaction Rates and Selectivites....................33

RESULTS AND DISCUSSION....................35

- Palladium-only Catalysts....................35
  - Supported Pd Catalysts....................35
    - TEM and XRD of Fresh Catalysts....................37
    - VA Reaction Rate Measurements....................37
    - Catalyst Deactivation....................47
    - Origin of CO_2 By-product....................56
  - Palladium Single Crystal Catalysts....................63
    - VA Reaction Rate Measurements....................63
    - Catalyst Deactivation....................66
    - Ethylene Combustion Kinetics....................70
- Palladium Alloy Catalysts....................80
  - Supported Pd-Au Catalysts....................80

Page

TEM and XRD of Fresh Catalysts....81
VA Reaction Rate Measurements....81
Catalyst Deactivation....90
Planar Pd-Au Catalysts....108
Surface Structure and Composition....109
VA Reaction Rate Measurements on Pd/Au(100) and Pd/Au(111)....116
Identification and Properties of the Active Site....118
Planar Pd-Sn Catalysts....129
VA Reaction Rate Measurements on Pd-Sn/Rh(100)....132
Catalyst Deactivation....137

SUMMARY....141

REFERENCES....143

VITA....151

LIST OF FIGURES

Page

Fig. 1. Schematic highlighting the differences between different catalysts used in our studies in terms of surface area and operating pressure....................3

Fig. 2. Schematic of the experimental apparatus used in our studies....................9

Fig. 3. Energy level diagram depicting an X-ray photoemission process....................12

Fig. 4. Schematic illustrating the energy level diagram of Auger electron emission process....................15

Fig. 5. Schematic diagram of the Michelson interferometer used in IRAS....................18

Fig. 6. Figure depicting the change in desorption rate and coverage as a function of sample temperature....................21

Fig. 7. Schematic diagram of the flame ignition detector (FID) used in GC....................25

Fig. 8. Schematic diagram of the components in the thermal conductivity detector (TCD)....................27

Fig. 9. Diagram illustrating the X-ray diffraction process....................31

Fig. 10. Schematic diagram of the arrangement of various components used in transmission electron microscopy (TEM)....................32

Fig. 11. TEM micrographs of the reduced (a) Pd(5 wt%)/SiO_2 and (b) Pd(1 wt%)/SiO_2 catalysts and the corresponding particle size distributions (c) and (d)....................38

Fig. 12. (A) XRD of the Pd(5.0 wt%)/SiO_2 catalyst after reduction at 673 K in 20 ml/min O_2 (10%) / N_2, 30 min, then 573 K in 20 ml/min H_2 for 30 min; (B) after reaction for 10 hours, at $p_{C_2H_4}$ = 7.5 kPa, p_{O_2} = 1.0 kPa, p_{AcOH} = 2.0 kPa, with remainder N_2; flow rate: 60 ml/min, at 413 K; (C) XRD of the Pd(1.0 wt%)/SiO_2 catalyst after reduction; and (D) after reaction as mentioned above for 16.7 hours....................39

Fig. 13. Arrhenius plot of VA formation rate on Pd(100) (■), Pd(5 wt%)/SiO_2 (●) and Pd(1 wt%)/SiO_2 (▲) at various temperatures. For Pd(100) p_{O_2} = 2.0 Torr, $p_{C_2H_4}$ = 9.0 Torr, p_{AcOH} = 4.0 Torr; for Pd(5 wt%)/SiO_2 and Pd(1 wt%)/SiO_2 catalysts p_{O_2} = 7.6 Torr, $p_{C_2H_4}$ = 57.0 Torr, p_{AcOH} = 12.0 Torr, the remainder N_2 ; flow rate: 30 - 60 ml/min, catalyst weight: 0.1 - 1.6 g....................40

Page

Fig. 14. VA synthesis versus temperature over (●) Pd(1 wt%)/SiO_2 and (■) Pd(5 wt%)/SiO_2 catalysts. $p_{C_2H_4}$ = 7.5 kPa, p_{O_2} = 1.0 kPa, p_{AcOH} = 2.0 kPa, the remainder N_2; flow rate: 60 ml/min, catalyst weight = 1.2 g..44

Fig. 15. VA reaction rates (▲: Pd(1 wt%)/SiO_2 , ■: Pd(5 wt%)/SiO_2) and selectivities (△:Pd(1 wt%)/SiO_2, □: Pd(5 wt%)/SiO_2) as a function of the C_2H_4 partial pressure at 413 K. $p_{C_2H_4}$ = 5.0-15.0 kPa, p_{O_2} = 1.0 kPa, p_{AcOH} = 2.0 kPa, the remainder N_2; flow rate = 30-60 ml/min, catalyst: 1.2 – 2.0 45

Fig. 16. VA reaction rates (▲:Pd(1 wt%)/SiO_2, ■: Pd(5 wt%)/SiO_2) and selectivities (△:Pd(1 wt%)/SiO_2, □: Pd(5 wt%)/SiO_2) as a function of the O_2 partial pressure at 413 K. $p_{C_2H_4}$ = 7.5 kPa, p_{O_2} = 1.0 - 10.0 kPa, p_{AcOH} = 2.0 kPa, the remainder N_2; flow rate = 30 - 60 ml/min, catalyst: 1.2 – 2.0 g...46

Fig. 17. VA reaction rate as a function of time on Pd(100) catalyst at 413 (▲) and 433 K (▼); p_{O_2} = 5.2 Torr, $p_{C_2H_4}$ = 21.0 Torr, p_{AcOH} = 8.0 Torr; on Pd (1 wt%)/SiO_2 (■) and Pd(5 wt%)/SiO_2 (●) catalysts at 443 K; p_{O_2} = 7.6 Torr, $p_{C_2H_4}$ = 57.0 Torr, p_{AcOH} = 12.0 Torr, the remainder is N_2; flow rate: 30 - 60 ml/min; catalyst weight: 0.1 - 1.6 g...49

Fig. 18. TEM images of the Pd(5 wt%)/SiO_2 and Pd(1 wt%)/SiO_2 catalysts after VA synthesis reaction for 10 and 16.7 hours, respectively at $p_{C_2H_4}$ = 7.5 kPa, p_{O_2} = 1.0 kPa, p_{AcOH} = 2.0 kPa, with remainder N_2; flow rate: 60 ml/min, at 413 K...50

Fig. 19. XRD pattern of Pd(5 wt%)/SiO_2 catalysts. A: reduced; B: reacted; C: reacted with H_2 treatment at 623 K for 4 hours...52

Fig. 20. XRD pattern of Pd(1 wt%)/SiO_2 catalysts. A: reduced; B: reacted; C: reacted with H_2 treatment at 623 K for 4 hours...54

Fig. 21. Variation of reaction rates (VA (■) and CO_2 formation (●)) and selectivity of CO_2 (▲) with the partial pressure of O_2 at 413 K over Pd(5wt%)/SiO_2 catalyst, feed gas: $p_{C_2H_4}$ = 7.5 kPa, p_{O_2} = 1.0-10 kPa, p_{AcOH} = 2.0 kPa, rest N_2; flow rate: 60 ml/min; catalyst weight: 1.6 g...58

Fig. 22. Dependence of CO_2 formation rate on partial pressure of C_2H_4 in the presence of acetic acid: (□) at 413 K, (○) 433 K and (△) 453 K, feed gas: p_{O_2} = 6.3

kPa, $p_{C_2H_4}$ = 5.0-15.0 kPa, p_{AcOH} = 2.0 kPa, rest N_2, flow rate: 60 ml/min, catalyst weight: 1.6 g; in the absence of acetic acid: (■) at 413 K, (●) at 433 K, (▲) at 453 K, feed gas: p_{O_2} = 6.3 kPa, $p_{C_2H_4}$ = 5.0-15.0 kPa, rest N_2, flow rate: 60 ml/min, catalyst weight: 1.2 g..59

Fig. 23. Dependence of CO_2 formation rate on partial pressure of O_2 in the presence of acetic acid: (□) at 413 K, (○) 433 K and (△) 453 K, feed gas: $p_{C_2H_4}$ = 7.5 kPa, p_{O_2} = 1.0-10.0 kPa, p_{AcOH} = 2.0 kPa, rest N_2, flow rate: 60 ml/min, catalyst weight: 1.6 g; in the absence of acetic acid: (■) at 413 K, (●) at 433 K, (▲) at 453 K, feed gas: $p_{C_2H_4}$ = 7.5 kPa, p_{O_2} = 1.0-10.0 kPa, rest N_2, flow rate: 60 ml/min, catalyst weight: 1.2 g..60

Fig. 24. Dependence of VA formation TOF on partial pressure of O_2 at 413 K (■), 423 K(●), 433 K (▲) on Pd(100); $p_{C_2H_4}$ = 9.0 Torr, p_{AcOH} = 4.0 Torr..........................64

Fig. 25. Dependence of VA formation rate on partial pressure of C_2H_4 at 433 K (■) on Pd(100); p_{O_2} = 2.0 Torr, p_{AcOH} = 4.0 Torr..65

Fig. 26. Upper panel is the C_{1s} XPS spectrum after VA reaction on Pd(100) at 433 K; p_{O_2} = 2.0 Torr, $p_{C_2H_4}$ = 9.0 Torr, p_{AcOH} = 4.0 Torr; Lower panel is the C_{1s} XPS spectrum of saturated coverage of CO on Pd(100) at 300 K................................68

Fig. 27. (A) C_{1s} XPS spectra on Pd(100) after reaction at 433 K and after annealing to temperatures as indicated; p_{O_2} = 2.0 Torr, $p_{C_2H_4}$ = 9.0 Torr, p_{AcOH} = 4.0 Torr; (B) C_{1s} XPS peak intensity for CH_x (●), CO (▲) and acetate (▼) species plotted against the annealing temperature..69

Fig. 28. Reaction rate as a function of O_2:C_2H_4 ratio at various temperatures on Pd(100); total pressure = 15.0 Torr; 428 K (■), 443 K (●), 458 K (▲), 473 (▼)........71

Fig. 29. Reaction rate as a function of O_2:C_2H_4 ratio at various temperatures on Pd(5 wt%)/SiO_2. Total pressure of C_2H_4 and O_2 = 131 Torr; remainder N_2. Flow rate: 60 ml/min, catalyst weight: 1.2 g; 433 K (■), 453 K (●), 473 K (▲)..................74

Fig. 30. Reaction rate as a function of O_2:C_2H_4 ratio at various temperatures on Pd(1 wt%)/SiO_2. Total pressure of C_2H_4 and O_2 = 131 Torr; remainder N_2; flow rate: 60 ml/min, catalyst weight: 2.0 g. 433 K (■), 453 K (●), 473 K (▲)..................75

Fig. 31. Comparison of the reaction rates for Pd(100), Pd(1 wt%)/SiO_2, and Pd(5 wt%)/SiO_2 catalysts. Pd(1 wt%)/SiO_2 (▲) and Pd(5 wt%)/SiO_2 (●) at 453 K and Pd(100) (■) at 458 K..76

Page

Fig. 32. Apparent activation energies as a function of the O_2:C_2H_4 ratio. Pd(1 wt%)/SiO_2 (▲), Pd(5 wt%)/SiO_2 (●) and Pd(100) (■)....77

Fig. 33. (A) C 1s XPS spectra at various O_2/C_2H_4 ratios on Pd(100) at 458 K. (B) C 1s/Pd 3d5/2 peak intensity as a function of the O_2:C_2H_4 ratio at 458 K on Pd(100) catalyst....78

Fig. 34. Comparison of C 1s XPS signal on Pd(100) after reaction at 458 K, O_2:C_2H_4 = 0.94:1.0; total pressure = 15.0 Torr and C 1s XPS signal on Pd(100) after CO saturation at room temperature. Saturation coverage of CO (solid line), carbon region after reaction (dashed line)....79

Fig. 35. TEM image of Pd-Au clusters for the reduced Pd-Au catalyst, atomic ratio of Pd/Au in region A = 2/1, at particle B = 2.2/1 and C = 1.9/1. The Pd-Au cluster size distribution is shown in the bottom panel....82

Fig. 36. XRD pattern of Pd-Au/SiO_2 catalysts. A: reduced; B: reacted; C: reacted with H_2 treatment at 623 K for 4 hours....83

Fig. 37. $p_{C_2H_4}$-dependent reaction rate for VA synthesis (A) and selectivity (C) at feed gas of $p_{C_2H_4}$ = 5.0-14.0 kPa, p_{O_2} = 1.0 kPa, p_{AcOH} = 2.0 kPa, the remainder N_2; p_{O_2}-dependent reaction rate for VA synthesis (B) and selectivity (D) at feed gas of $p_{C_2H_4}$ = 7.5 kPa, p_{O_2} = 1.0-8.4 kPa, p_{AcOH} = 2.0 kPa, remainder N_2. Reaction conditions: 0.1-1.0 g of the Pd-Au catalyst, 30 - 60 ml/min of flow rate, temperatures of 433 K (▲), 413 K (■) and 393 K (●)....87

Fig. 38. Arrhenius plots for VA synthesis on the Pd-Au catalysts. Region I: 393 – 413 K, II: 413 -433 K. Varying p_{O_2} at 1.0 kPa (■), 2.2 kPa (▲), 4.2 kPa (▼), 6.3 kPa (♦) and 8.4 kPa (●) while keeping $p_{C_2H_4}$ = 7.5 kPa, p_{AcOH} = 2.0 kPa, remainder N_2....88

Fig. 39. Catalytic stability of Pd(1 wt%)-Au(0.4 wt%)/SiO_2 catalyst in the absence of VA, feed gas: $p_{C_2H_4}$ = 7.5 kPa, p_{O_2} = 6.3 kPa, rest N_2; flow rate: 60 ml/min, at 413 K....91

Fig. 40. TEM image of Pd-Au clusters for the reacted Pd-Au catalyst (top, for VA synthesis in a mixture of C_2H_4 = 7.5 kPa, O_2 = 1.0 kPa, AcOH = 2.0 kPa,

Page

remainder N_2, at 413 K for 100 hours), atomic ratio of Pd/Au in region A = 1.5/1, at particle B = 1.1/1 and C = 1.3/1; the Pd-Au cluster distribution is shown at the bottom..94

Fig. 41. C1s spectroscopy of reduced Pd-based catalysts. A: Pd(1 wt%)/SiO_2; B: Pd(5 wt%)/SiO_2; C: Pd-Au/SiO_2..95

Fig. 42. XPS C1s spectroscopy of reacted Pd-based catalysts. A: Pd(1 wt%)/SiO_2; B: Pd(5 wt%)/SiO_2; C: Pd-Au/SiO_2...96

Fig. 43. XPS C1s spectroscopy of reacted Pd-based catalysts with H_2 treatment at 623 K for 4 hours. A: Pd(1 wt%)/SiO_2; B: Pd(5 wt%)/SiO_2; C: Pd-Au/SiO_2......................97

Fig. 44. VA synthesis in the presence of CO at 413 K in the feed gas of $p_{C_2H_4}$ = 7.5 kPa, p_{O_2} = 1.0 kPa, p_{AcOH} = 2.0 kPa, remainder N_2, p_{CO} : 0 (■), 0.1 kPa (▼), 0.5 kPa (▲), 1.0 kPa (●)..100

Fig. 45. VA reaction rates as a function of catalyst reduction temperature. (■): reaction rates and (●): selectivity for VA formation. $p_{C_2H_4}$ = 7.5 kPa, p_{O_2} = 1.0 kPa, p_{AcOH} = 2.0 kPa, remainder N_2; flow rate: 60 ml/min, reaction temperature: 413 K, flow rate: 60 ml/min..102

Fig. 46. SEM images of Pd-Au/SiO_2 catalysts reduced at various temperatures......................103

Fig. 47. Size distribution of metal particles on catalysts reduced at various temperatures..104

Fig. 48. XPS of Pd 3d region as a function of the reduction temperature of Pd-Au/SiO_2..106

Fig. 49. Pd/Au ratio determined by EDX and XPS as a function of the catalyst reduction temperature..107

Fig. 50. Surface concentration of Pd (●) for Au-Pd thin films on Mo(110) after annealing to 800 K, (■) after Au (0.1 – 1.0 ML) deposition on 1.0 ML Pd/SiO_2 and annealing to 800 K and the dashed line is calculated Pd concentration..112

Fig. 51. In situ atomic resolution STM images of PdAu alloys electrodeposited on Au(111) for (A) $Pd_{07}Au_{93}$; and (B) $Pd_{15}Au_{85}$. Pd atoms appear larger and, depending on tunneling conditions, brighter or darker than Au atoms. (C) Surface coverages of Pd monomers, dimers, and trimers, as obtained from atomically resolved STM images..114

Page

Fig. 52. IRAS spectra after CO adsorption at 90 K on 4 ML Pd/Au(100) and 4 ML Pd/Au(111). Pd was deposited on Au(100) and Au(111) at 90 K and subsequently annealed to 300 and 600 K for 10 minutes each............................115

Fig. 53. TPD of CO on: a) 10 ML Pd/Mo(110) and b) 5 ML Pd/5 ML Au/Mo(110) annealed to 800 K for 20 minutes..117

Fig. 54. CO_2 formation rates as a function of Pd coverage on Au(111). $CO:O_2$ = 2:1, with total pressure of 5 Torr. The reaction was carried out at 523 K with a total reaction time of two hours. The data show that isolated Pd monomers have similar activity for CO oxidation at contiguous Pd sites..................119

Fig. 55. VA formation rates as a function of Pd coverage. The TOF's are computed with respect to the (1 x 1) surface unit. The VA synthesis was carried out at 453 K for 3 hours, with acetic acid, ethylene and O_2 pressures of 4, 8 and 2 Torr, respectively. The error bars are based on background rate data...120

Fig. 56. Simulation of the number of surface Pd monomers as a function of Pd coverage on Au(100) surface. The data were simulated by Z. Dohnalek at Pacific Northwest National Laboratories, USA...122

Fig. 57. VA formation rates as a function of Pd coverage. The TOFs are computed with respect to the Pd atom concentration. Pd was deposited on the respective surface at 300 K and annealed to 600 K for 10 min. C_2H_4 = 8 Torr, O_2 = 2 Torr, CH_3COOH = 4 Torr, reaction temperature = 453 K, reaction time = 3 hours. The error bars are based on background rate data. The inserts show Pd monomers and monomer pairs on the Au(100) and Au(111)...123

Fig. 58. Simulation of the number of surface Pd monomer pairs as a function of Pd coverage on Au(100) surface. The Pd monomer pairs are encircled by red ellipses in the insert. The data were simulated by Z. Dohnalek at Pacific Northwest National Laboratories, USA...124

Fig. 59. HREELS spectra of : (A) Acetic acid adsorption on a) Pd/Au(111) with only isolated Pd sites, b) Pd/Au(111) with continuous Pd sites, and c) 1 ML Pd/Au(111) after VA synthesis reaction for 3 hours. (B) Ethylene adsorption on a) Pd/Au(111) with only isolated Pd sites, and b) Pd/Au(111) with continuous Pd sites. Acetic acid was dosed into the chamber with a background pressure of 2×10^{-8} Torr and cooling the sample from 350 K to 210 K. Ethylene was dosed into the chamber with a background pressure of 2×10^{-8} Torr and cooling the sample from 300 K to 170 K..................................127

Page

Fig. 60. Schematic for VA synthesis from acetic acid and ethylene. The optimized distance between the two active centers for the coupling of surface ethylene and acetate species to form VA is 3.3 Å. Coupling of an ethylene and acetate species on a Pd monomer pair is possible on the Au(100), but not so facile on the Au(111)..128

Fig. 61. TPD of ethylene (C_2D_4) from supported Pd and Pd-Au alloy clusters.......................130

Fig. 62. Schematic depicting the changes in the surface coverage leading to the formation of a c(2 x 2) structure with the surface coverage of both Sn and Pd at 0.5 ML due to annealing the Sn/Pd(100) surfaces to temperatures higher than 600 K. The distance between two Pd atoms on the surface is 3.89 Å as illustrated in the diagram...131

Fig. 63. (A) Calibration of Pd doser on Rh(100) at 300 K. (B) Calibration of Sn doser on Pd(100) at 300 K..133

Fig. 64. VA formation rate on Sn/4.0 ML Pd/Rh(100) system annealed to 600 K for 60 sec at different coverages of Sn. Reaction at 450 K; p_{O_2} = 2.0 Torr; $p_{C_2H_4}$ = 9.0 Torr; p_{AcOH} = 4.0 Torr; Time = 3 hours..134

Fig. 65. VA formation rate normalized to per Pd site basis on Sn/ 4.0 ML Pd/Rh(100) annealed to 600 K for 60 sec. Reaction at 450 K; p_{O_2} = 2.0 Torr; $p_{C_2H_4}$ = 9.0 Torr; p_{AcOH} = 4.0 Torr; Time = 3 hours...136

Fig. 66. VA formation rate as a function of time on 0.5 ML Sn/4.0 ML Pd/Rh(100) annealed to 600 K for 60 sec. Reaction at 450 K; p_{O_2} = 2.0 Torr; $p_{C_2H_4}$ = 9.0 Torr; p_{AcOH} = 4.0 Torr...138

LIST OF TABLES

Page

Table 1. Pd particle sizes measured by TEM before and after VA synthesis reaction................41

Table 2. List of all the catalysts used in the experiments and the corresponding kinetic data obtained for VA synthesis reaction..42

Table 3. Kinetic parameters for ethylene combustion in the presence and absence of acetic acid according to the power rate law: $r_{CO_2} = k \cdot p_{C_2H_4}^{a} \cdot p_{O_2}^{\beta}$ 62

Table 4. Kinetic parameters for the synthesis of VA over Pd-Au/SiO_2 catalyst, power law functionality: $r_{VA} = k \cdot p_{C_2H_4}^{a} \cdot p_{O_2}^{\beta}$ 85

INTRODUCTION

Heterogeneous and Model Catalysts

The demand and the usage of modern synthetic products have increased tremendously in the past few decades. Large scale production of these end products has been possible industrially due to the use of heterogeneous catalysts. Other than the synthesis of organic derivatives, modern catalysts are employed in diverse fields, such as, oil refining, pollution control, gas sensors, etc [1,2]. The preparation methods, the composition of the active components and the conditions employed govern the behavior of the catalysts which is described in terms of activity, selectivity and deactivation [3,4]. The best performance of a heterogeneous catalyst can be achieved by varying the preparation procedures, the operating conditions and the catalysts constituents [1]. A general idea about the particle size can be acquired using microscopic techniques, but the effect of the variation of particle size on the atomic structure and electronic properties is difficult to discern. It is also extremely difficult to understand the role/effect of the components, additives, pretreatment conditions, etc., at the atomic/molecular level. The sintering mechanisms of the nanometer range clusters, the type of support employed, the interaction between the metal and the support, etc., further extend the complexity of these systems. What can be obtained from the characterization and investigation of heterogeneous catalyst systems is limited knowledge relating the overall average properties to the external behavior of the catalysts.

This thesis follows the style of Topics in Catalysis.

A molecular level understanding of surfaces and adsorbates has been made possible during the past few decades due to the development of many surface sensitive spectroscopic techniques [2,5]. Ultra high vacuum (UHV) conditions have made it possible to study chemical reactions, surface adsorbates, adsorbate-adsorbate interactions, and other processes in great detail in a contamination-free environment. The catalyst metal systems employed by the surface scientists consists of the so called "model catalysts" consisting of metal single crystals, multi-metallic thin film surfaces, and thin oxide supported metal catalysts. Over the past decades it has been established that in numerous instances studies using these model systems correlate with chemical processes occurring on heterogeneous catalysts and the seemingly vast differences between the model and heterogeneous catalyst systems in terms of the operating pressures and surface area have narrowed [2-11]. Before discussing the development and properties of the model systems, it will be appropriate to familiarize the reader with the differences between the model catalysts and heterogeneous "real world" catalysts.

As mentioned earlier, the utilization of surface science spectroscopies and the maintenance of a clean surface on a model catalyst require operating under a UHV environment. The industrial catalysts on the other hand are operated at elevated pressures higher than the atmospheric pressure. The vast difference in the operating pressures of the two applications, also called "pressure gap" (see Fig.1) is one of the problems that a surface scientist would like to resolve in order to relate the investigations on model catalysts to that of the industrial catalysts [10,12]. One method used to address this issue is the design of systems capable of performing reactions at high pressures in a reactor system contiguous to a UHV system [12,13]. The huge difference in the pressures in different parts of the system does not disturb the UHV conditions. In fact, kinetic measurements performed using this setup allow us to do reactions on clean

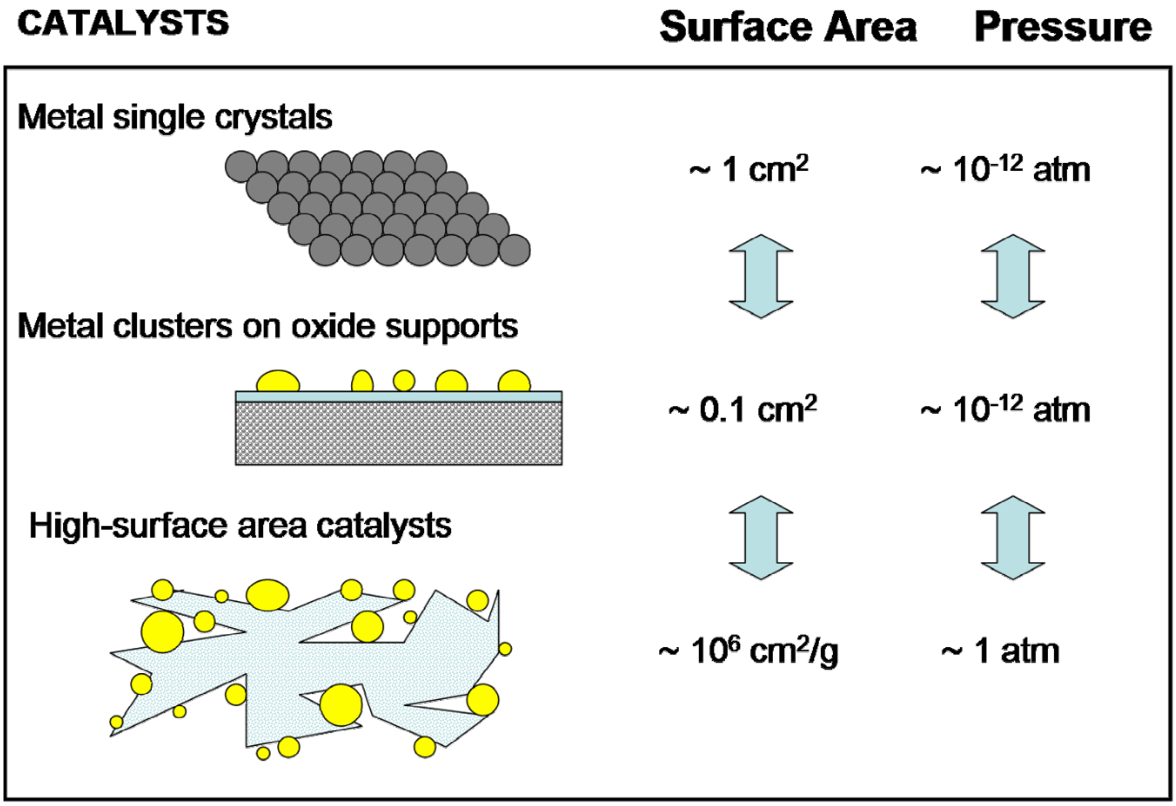

Fig. 1. Schematic highlighting the differences between different catalysts used in our studies in terms of surface area and operating pressure.

surfaces by characterizing the surface before and after reactions using various surface science techniques.

The other perceptible difference between the model and industrial catalysts is in terms of the “material gap” [9,10,14,15]. Industrial catalysts have oxides as supports, and have high porosity and surface area to finely disperse the precious metal particles. These catalysts involve the use of ceramic substrates with similarly spaced and sized channels with round, square, hexagonal and triangular pore structures for effective mass transport. These ceramic monoliths with a low surface area (~ 0.5 m^2/gm) are coated on a high surface area (~ 100 m^2/gm) support. Catalytically active metals and promoters are then added by different methods.

Low-index single crystals are the simplest and most commonly used model surfaces to elucidate the fundamental phenomena that occur on a commercial catalyst [6,10,16,17]. Single crystals have surface atoms in a highly homogenous and ordered configuration. This allows the investigation of the effect of the surface structure, and the adsorption/desorption properties of active sites with greater accuracy. A logical step in addressing the concerns related to the special properties of multimetallic systems and in extending the simplicity of the single crystals towards more complex heterogeneous catalysts is the synthesis of mixed-metal systems. Bimetallic systems find extensive applications in catalysis, semiconductors, electrochemistry, etc. For example, these catalysts were extensively used in hydrocarbon reforming in the 1960’s and 70’s [18]. Due to this many surface science investigations have endeavored to unravel the chemical, electronic and physical properties of these systems [19-25]. The modern surface scientist is confronted with these questions and knowledge of these systems is required to design and understand the complex heterogeneous catalysts. There are two methods of production of the bimetallic surfaces [19]. The first one involves vapor deposition of one metal onto a clean well-defined single crystal surface in UHV. The second method consists of cutting and polishing an alloy single-crystal followed by cleaning in UHV. The former method has been popular and has produced exciting results. Using these crystalline alloy films one can study structure-function relationships by correlating the atomic structure with the electronic and chemical properties.

Single crystal surfaces and even bimetallic surfaces do not accurately mimic the complexity of the real world catalysts. Issues related to the particle size and metal oxide support and particle interaction need to be addressed and cannot be answered using single crystals as model catalysts. Metal oxide supports are used in industrial catalysts to disperse the catalytic metal on the surface yielding a high surface area. Bulk oxide crystals, such as, TiO_2 can also be used as model oxide supports. Model supports can be prepared by two methods; cleaving the bulk oxide single crystals in air or in UHV is one of the approaches [26-28]. These systems need to be cleaned by sputtering and annealing techniques in UHV. Although these metal oxide single crystal supports exhibit excellent thermal stability, there are significant differences in the structure of these model systems in terms of number of defects depending on the method of cleavage. Also, electrical conductivity of these bulk oxide systems does not make them amenable to surface science methods. The utilization of metal oxide supports in model catalysts helps a surface scientist in elucidating the complex phenomena of a working catalyst related to particle size and morphology effect, the metal-support interaction, etc. [9,14,27,29]. One of the disadvantages associated with these films is that they might not be very stable at higher temperatures due to the mobility of the oxide ions. However, a number of thin metal oxide films have been prepared in the past two to three decades, such as, Al_2O_3 [30-32], SiO_2 [33-36], MgO [37-41], NiO [42-45], Cr_2O_3 [46-48], Ti_xO_y [49,50], $Fe_{3x}O_y$ [51-53] and many others [26-28].

Integrating the modern ultrahigh vacuum surface science and kinetic studies of heterogeneous catalysts is a challenge aimed at simplifying the complexity of industrial catalysts. Well-defined systems, such as single crystals can be actively targeted to obtain specific information about the electronic structure and chemisorption phenomena. Kinetic measurements and physical characterization techniques are important for high surface area catalysts. In this regard, the present study examines vinyl acetate reaction and utilizes single crystal surfaces and high surface area palladium based catalysts.

Vinyl Acetate Synthesis

VA is a very important monomer for the synthesis of polyvinyl alcohol and polyvinyl acetate, and is used in paints, surface coatings and adhesives. The annual production of VA in USA is about 1.3 million ton. VA reaction has been studied both in gas phase and in liquid phase. Moiseev *et al*. in 1960 had used $[PdCl_2(C_2H_4)]_2$ complex catalyst [54] with sodium acetate as promoter and was commercially used at ICI and others [55-58].

VA synthesis catalysts consisted of three components – Pd-acetate, Cd-acetate and K-acetate impregnated evenly on SiO_2 support (5-mm spheres). The catalysts were reduced to Pd metal prior to the reaction [59]. Unlike the Bayer catalyst which was further developed by Dupont [60], Pd and Au were impregnated as their chlorides salts and reduced to yield thin layers of metals around a spherical silica pellet; this was followed by impregnation of K-acetate homogenously on the catalyst. VA is primarily obtained by the reaction of ethylene, oxygen and acetic acid in the temperatures ranging from 413 to 473 K and pressures from 600 to 1000 kPa.

$$C_2H_4 + CH_3COOH + \frac{1}{2}O_2 \rightarrow C_2H_3OOCCH_3 + H_2O \qquad (1)$$

Currently, Pd-based catalysts and Pd-based alloys, such as, Pd-Au, Pd-Cd are commercially used to produce vinyl acetate by selective oxidation of ethylene in presence of acetic acid. The selectivity of the reaction is as high as 96 % [61]. Two contending mechanisms have been proposed based on Pd(0) and Pd(2+) centers. Moiseev *et al.* have suggested that the active site consists of Pd(0) centers [62]. The subsequent reaction of acetic acid with the vinyl intermediate is a fast process yielding the final product, VA. Wacker-like process over Pd(2+) [63,64] was the alternative mechanism suggested. The process followed initial adsorption of acetic acid and ethylene, ethylene inserting into surface acetate, activation of β C-H bond of the ethyl acetate intermediate and finally desorption of VA [65]. The rate limiting steps in this mechanism have been suggested to be the ethylene insertion into surface acetate and β C-H bond activation of the intermediate. Evidence has been reported for both mechanisms and no mechanism has not been distinctly ruled out. Also, the secondary decomposition steps leading to the combustion of acetate, ethylene and VA have also not been clearly established. Though some basic research regarding the kinetic and mechanistic parameters [62,63,66-69] has been reported on different Pd-based catalysts, a consensus about the mechanism, the role of additives, the nature of the active sites and the intermediates involved during the formation of VA is not established.

EXPERIMENTAL

Model Catalysts

Ultrahigh Vacuum (UHV) Chamber

To ensure the cleanliness of the surface under investigation and to prevent contamination from the background gas molecules, most of the surface science studies are conducted under ultrahigh vacuum (UHV) conditions. Operating at UHV pressures, for example, at 1.0 x 10^{-10} Torr, a surface becomes completely covered by one layer of gas molecules in more than 3 hours, which gives us a sufficient amount of time to do an experiment on a clean surface. A UHV environment also allows the usage of low energy electron- and ion- incidence spectroscopies by limiting the scattering of the electrons with the background gas and reducing the interference. The mean free path of the electrons and ions are significantly enhanced and are reflective of the properties of the surfaces from which they are emitted.

In our experimental setup, as shown in Fig. 2, a commercial PHI 5500 system is integrated with a standard belljar type preparation chamber. Both systems are capable of 10^{-10} Torr pressures and are bakeable. The surface analysis section is ion pumped and houses an X-ray source with a dual Mg/Al anode, a monochromator, an Auger electron gun, a quadrupole mass spectrometer, a differential ion gun and a hemispherical analyzer. The preparation chamber is turbo pumped and is equipped with a gas beam doser and metal dosers. Contiguous to the preparation chamber is a catalytic reactor which is custom built and uses a retraction bellows to support the catalyst and allows translation of the catalyst in vacuo from the reactor to the surface analysis region. In surface analysis section, the surface chemical composition and

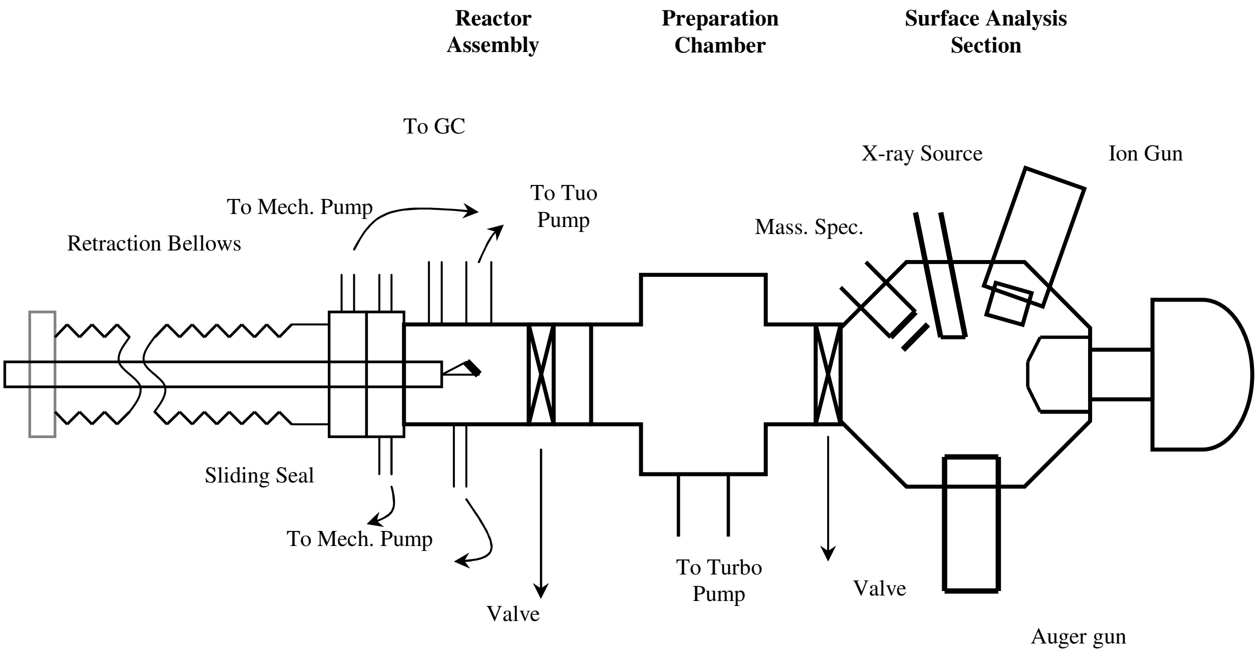

Fig. 2. Schematic of the experimental apparatus used in our studies.

cleanliness is determined using X-ray photoelectron spectroscopy (XPS) or Auger electron spectroscopy (AES), and the sample can be sputtered using the differentially pumped ion gun. In the preparation chamber, the sample is cleaned or dosed with gases using a gas beam dosing array or catalytically relevant metals using metal dosers. The gas beam doser is a 1 mm diameter pipe attached to a leak valve with the tip to sample surface distance of about 5 mm. The metal dosers are made by wrapping a clean wire of the metal to be dosed (Pd, Au, Ti, etc.) onto a tantalum wire. The filaments of metals thus made are physically separated from each other and a uniform dosage of metals can be obtained by heating the filament resistively. The catalyst can be retracted to the catalytic reactor which is capable of admitting gases at the total pressures up to ~2 atmospheres and could be pumped down to 2×10^{-10} Torr. The reactor is evacuated using a turbo pump following a reaction at high pressures and the catalyst is moved forward in to the preparation chamber and surface analysis section for surface analysis. Thus, surface analysis can be done before and after the reaction.

Surface Science Techniques

The development of many surface spectroscopies dates back to more than 50 years [2,70]. Over time relatively new techniques were developed and most complex surface properties of catalysts could be probed using these methods. In this section only a few common techniques which were primarily employed in the experiments will be introduced. For a thorough understanding of the development and the features of many surface spectroscopies the reader is directed to some excellent reviews in this field [2,70-74]. These techniques are X-ray photoelectron spectroscopy (XPS), Auger electron spectroscopy (AES), infrared reflection absorption spectroscopy (IRAS), low energy ion scattering spectroscopy (LEISS) and temperature programmed desorption (TPD).

X-ray Photoelectron Spectroscopy (XPS)

XPS, also called electron spectroscopy for chemical analysis (ESCA), is a widely used surface chemical analysis technique. This surface science technique is used to obtain information regarding the elemental composition and chemical states of the atoms in the surface. The probing depth of XPS is about 1 - 5 nm (4 to 20 atomic monolayers) and concentrations up to 0.1 to 1.0 atomic % can be determined by using this technique [2,70]. A monochromatic X-ray beam is used to bombard the surface to induce core level ionizations in the atoms. The process is schematically expressed in Fig. 3. The kinetic energy of the ejected core level electron is determined as follows:

$$E_{kin} = h\nu - E_b - \Phi \qquad (2)$$

where, E_{kin} is the kinetic energy of the ejected core level electron, $h\nu$ is the energy of the incident beam of photons from the X-ray source, E_b is the binding energy and Φ is the work function of the spectrometer. The binding energy is determined by referencing to the Fermi level and every element has a characteristic binding energy feature. All elements, except H and He, can be analyzed using XPS. Low energy charge neutralization is used to analyze non-conducting samples.

XPS can also be used to obtain information regarding the chemical state and the electronic structure of an element. Core-level binding energy is dependent not only on the level from which the photoemission is occurring, but also on other factors such as, the oxidation state of the atoms, the hybridization and the local chemical and physical environment of the atoms.

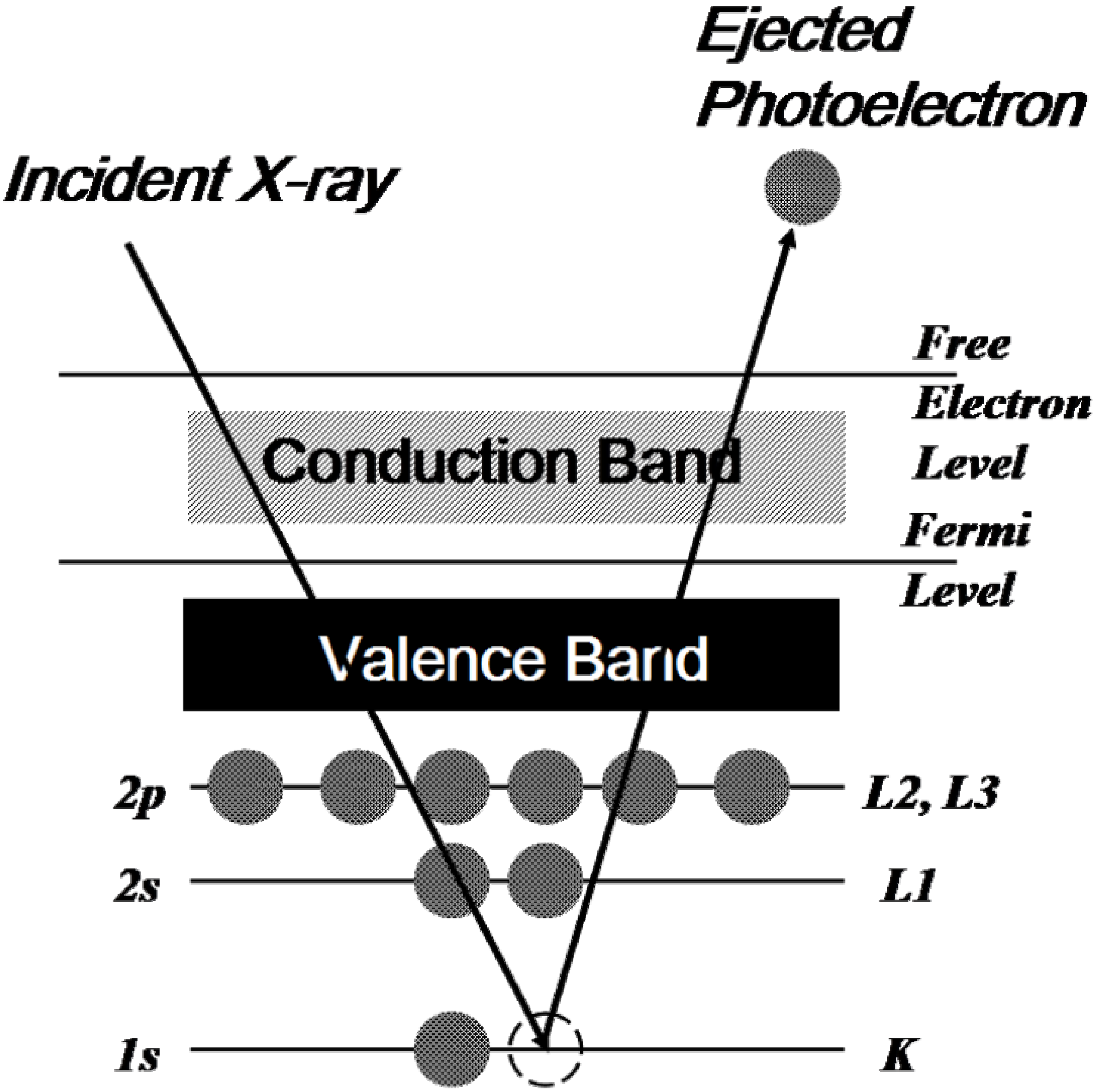

Fig. 3. Energy level diagram depicting an X-ray photoemission process.

Any changes in these factors are reflected as shifts in the core-level binding energies (in the order of a few eV). These effects are collectively referred to as "initial state" effects. In other words, the initial state effects are those factors which control the oxidation state of the atom prior to the bombardment by the X-ray photons. Higher binding energy is observed for atoms in a higher positive oxidation state due to a greater coulombic interaction between the ejected photoelectron and the ion core.

Shifts in the core-level binding energy are also observed due to the relaxation of an ionized atom. These shifts called "final state" effects are reflective of the screening process of the core-level electron vacancy. In other words, the final state effects are those factors which control the charge of the atom after the bombardment by the X-ray photons. Relaxation is a rapid process and can be due to intra-atomic or inter-atomic charge transfer. Increase in the relaxation is reflected in a shift of the core-level binding energy to a lower value. It is usually very difficult to ascertain the core-level binding energy shift due to final state effects. Apparently it is also very difficult to distinguish and differentiate between the initial and final state effects and their contributions to the overall core-level binding energy shift.

XPS is also regularly used to determine the thickness of a film from the attenuation of the underlying substrate signal. The following equation can be used in the process.

$$d = \tau \cdot t = \lambda \cdot \ln\left(\frac{I_o}{I}\right) \tag{3}$$

where, d is the thickness of the film, τ is rate of evaporation of the element, t is the evaporation time, λ is the mean free path of the electron from the substrate, I_0 is the XPS intensity for the clean substrate and I is the XPS intensity of the film covered substrate.

In the current study, XPS measurements were performed using a PHI 5500 spectrometer, using Mg-K_α radiation (300 W, pass energy 58.7 eV). The binding energy was calibrated using

Pd $3d_{5/2}$ peak at 334.9 eV. Also, the instrument was calibrated using cleanly sputtered Au and Cu foils. The background contribution caused due to inelastic processes was subtracted using Shirley method and the curve fitting was performed using Lorentzian-Gaussian by attached software.

Auger Electron Spectroscopy (AES)

AES is a most commonly used surface science technique which provides information regarding the surface specific elemental composition of metals and metal-oxide thin films. In this process an accelerated beam of electrons with kinetic energy adjusted to be within 1-10 keV is used to bombard the surface [2,70]. Due to the collision of the electrons with the core level electrons, a photo electric effect ensues and a core level electron is emitted forming a core hole. This process is followed by two main processes, X-ray fluorescence and Auger transition, which help the system relax to a stable energy state. In the X-ray fluorescence process the core hole is filled with an electron from a higher shell. As illustrated in Fig. 4, the energy emitted due to the filling of the core level hole is used in the emission of a second electron called Auger electron and the process is called Auger process. The kinetic energy of the Auger electron is calculated from the differences between the electronic levels involved in the core level filling and Auger relaxation processes. The kinetic energy of the emitted electron is calculated by

$$E_{KLM} \approx E_K - E_L - E_M - \delta E - \varphi \tag{4}$$

where, E_{KLM} is the kinetic energy of the Auger electron, $E_{K,\,L,\,M}$ are the binding energies of the electrons in the K, L, M shells, δE is the energy shift caused by relaxation effects and φ is the work function of the sample. The kinetic energy values thus recorded are characteristic for each element and can differentiate between elements. The emission of secondary electrons due to the

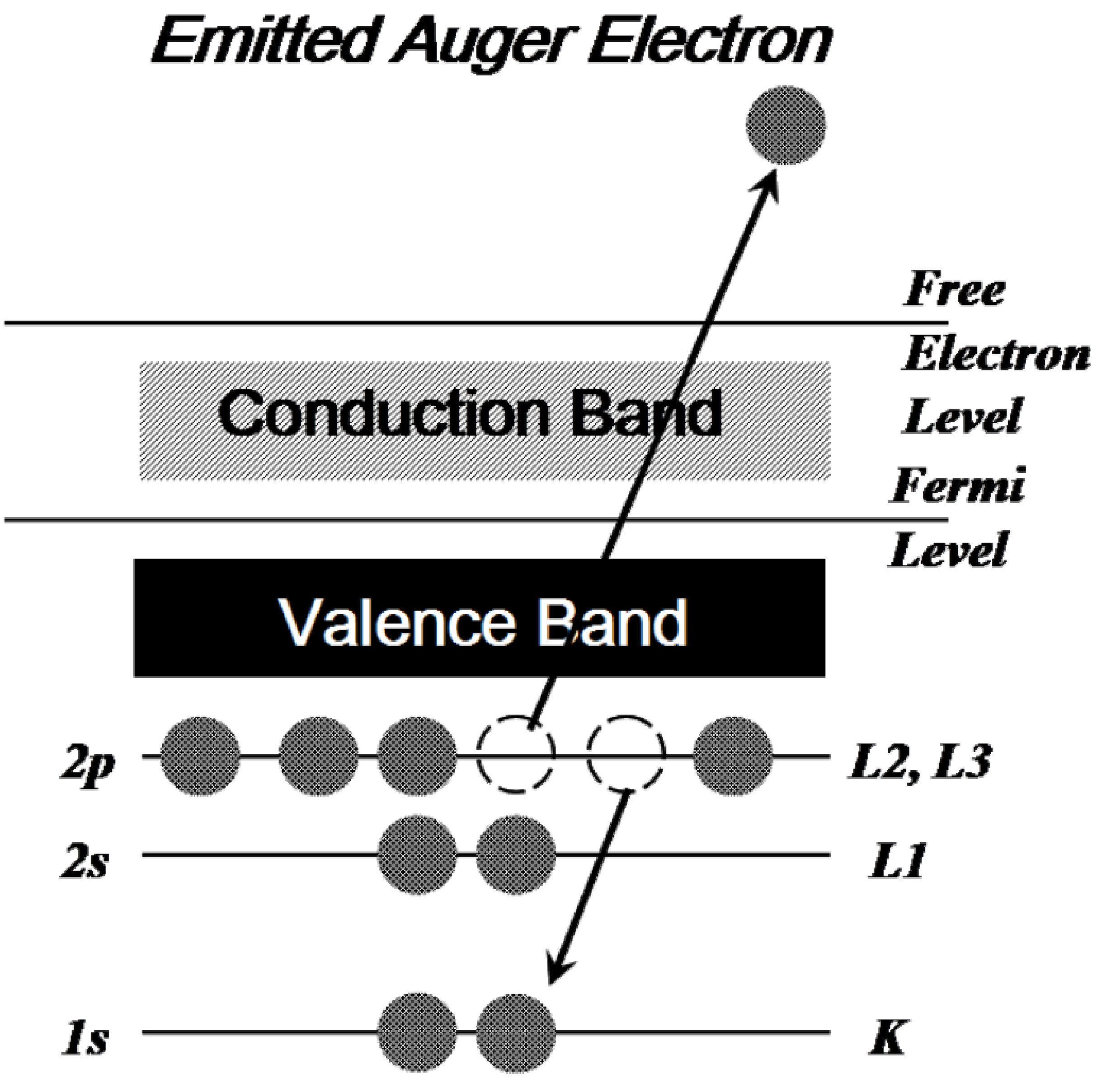

Fig. 4. Schematic illustrating the energy level diagram of Auger electron emission process.

incidence of the high energy primary beam leads to the formation of high background signal. Hence, the AES signal is plotted as a 1st derivative of the curve with respect to the energy (dN/dE) giving sharp spikes at different AES transition binding energies. AES transition energies are thus reported using the energies at the center of the negative peaks in the 1st derivative curve.

AES is a surface sensitive tool which can probe up to a depth of top few atomic layers of the sample surface. This is possible because of the fact that the Auger transitions have energies less than 1 keV, and hence, the mean free path of the electrons is relatively small and is limited to only a few nanometers. AES is also conventionally used to determine the thickness of the metal and metal oxide films grown on conducting surfaces. The film thickness can be determined using the attenuation of AES signal of the substrate during the growth of the film as below:

$$I_S = I_S^o\ (\exp(-d\ /\ \lambda_i^s \cos \alpha) \qquad (5)$$

where, I_S and I_S^o are the intensities of the AES signals of the clean and film grown substrate, d is the film thickness, λ_i^s is the effective attenuation length of electrons in the film and α is the electron emission angle with respect to the surface normal.

Infrared Reflection Absorption Spectroscopy (IRAS)

When a molecule is adsorbed on the surface it vibrates. Such vibrations can be closely monitored and studied using infrared light. Infrared reflection absorption spectroscopy (IRAS) is a commonly used technique in the surface science studies [2]. High resolution electron energy loss spectroscopy (HREELS) is also another common technique with very high sensitivity (1/1000 ML of CO is detectable). On the other hand, IRAS has a very good resolution (at least

10 times better). The other significant advantage of using IRAS is that light can be used in gaseous environment (in situ conditions) and the operating pressures can be varied from UHV to atmospheric pressure. The main disadvantage of IRAS is that the spectral region is restricted. Vibrational spectra from 5000 to 400 cm^{-1} can be investigated using this technique in conjunction with appropriate IR windows. The sensitivity is comparable to that of HREELS and hence finds applications in the studies related to heterogeneous catalysts. IRAS can provide information pertaining to the adsorption geometry, adsorption sites and the surface composition.

When an infrared beam reflects from the surface of a metal, the electrical field near the surface can be evaluated using Fresnel equations [75]. The selection rules for the vibrations in IRAS are similar to that of dipole scattering in HREELS. For the s-polarized light (polarized perpendicular to the plane of incidence, the reflectivity is high for all angles of incidence and due to reflection the phase is reversed. This results in a small signal due to the interference of the incident and reflecting beam. However, for p-polarized light the signal intensity is strongly dependent on the angle. For p-polarized light the phase difference remains small for a wide range of incident angles ($0 < \varphi < 85^o$) and at grazing incidence angles the phase difference increases to 180^o. In contrast to the s-polarized light, the p-polarized light interferes constructively to result in an enhancement in the field normal to the surface. Hence, only p-polarized light interacts with the surface and can be used to probe the molecular vibrations on a metal surface.

Infrared spectroscopy has gained in popularity since the development of Fourier transform spectrometers. As shown in Fig. 5, the Michelson interferometer involves the use of a beamsplitter, B. The IR source supplies the incident beam which is split due to B and one part gets reflected from the fixed mirror. The other part of the beam is passed onto a movable mirror.

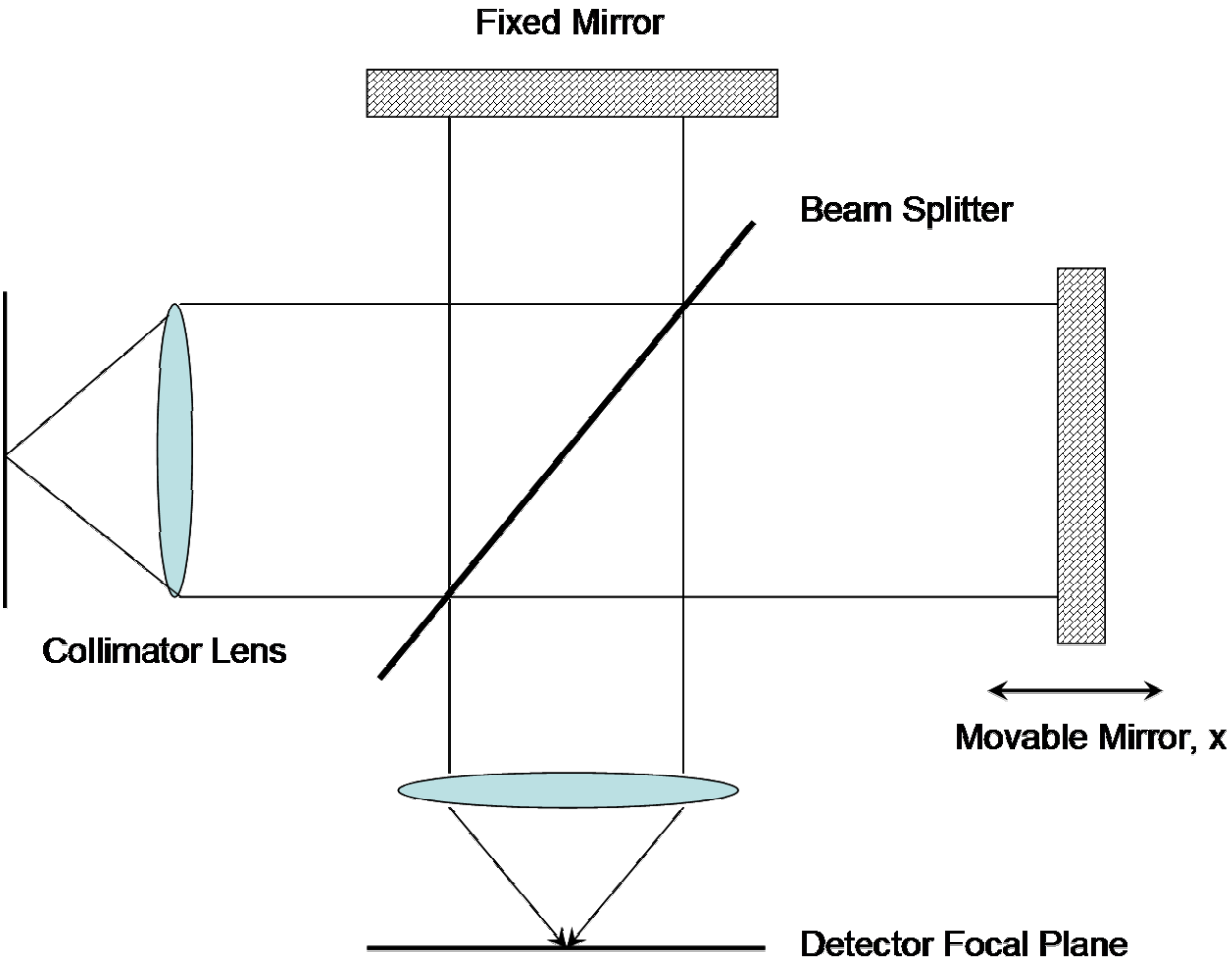

Fig. 5. Schematic diagram of the Michelson interferometer used in IRAS.

The resulting intensity is then measured by a detector as a function of the displacement of the movable mirror, x. By using a simple Fourier transform the spectral distribution is then evaluated. The whole setup is housed next to a UHV chamber with the sample.

When a gas molecule, such as CO, is adsorbed on a metal surface, the rotational degree of freedom is restricted and the local geometry of the atoms in the molecule also changes. The interaction between the electronic energy levels of the molecule and the surface leads to the observed changes in the vibrational modes. Usually for CO a red shift (shift to a lower frequency) is observed when adsorbed on a metal surface due to the weakening of the C-O bond. The shifts in the vibrational frequencies of adsorbed CO molecule on a metal surface could be because of dipole coupling and/or chemical effects. CO molecule experiences an electric field due to the surrounding dipoles and hence leads to the shift. Chemical effects are due to the attractive and repulsive forces that affect the bonding of CO on a metal surface.

Low Energy Ion Scattering Spectroscopy (LEISS)

Low energy ion scattering spectroscopy (LEISS) involves the bombardment of the surface with a beam of ions and some of these projectiles are scattered back after colliding with the atoms on the top most layer of the surface [76]. The energy of these backscattered ions is measured to recognize the mass of the target atoms in the surface. This surface science technique is extremely surface sensitive and usually ions of inert gases such as, He, Ne and Ar, in the energy range of a few hundred eV to a few keV are used in the process. Apart from determining the composition of the surface, this technique is widely used to determine the structure of the surface.

The scattering of the ions from the surface is treated as classical elastic two-body collision model since the time of collision is small with respect to the time period of phonon frequencies in a solid. Hence, the conservation of energy and momentum principles are applied to the collision system. The following equation governs the behavior of such collision model.

$$\frac{E_1}{E_0} = \frac{1}{(1+A)^2}\left(\cos\theta \pm \sqrt{A^2 - \sin^2\theta}\right)^2 \qquad (6)$$

where, an incident ion with an energy of E_0 and mass, M_1, impinges on a surface atom of mass, M_2, the energy of the scattered ion is given by E_1 and the scattered angle of θ, $A = M_2/M_1$ and if $A > 1$ then '+' and if $A < 1$ then '-' is used.

Temperature Programmed Desorption (TPD)

Temperature programmed desorption (TPD) is one of the most widely used surface science techniques to identify the adsorbates and the reactions happening on the surfaces and to detail the kinetic and thermodynamic properties during the desorption process. TPD is done using a mass spectrometer (MS). MS can also be used for residual gas analysis (RGA) to analyze the gases in the UHV chamber. As the name implies, TPD is performed by increasing the temperature of a sample at a linear rate due to which desorption of the molecules/atoms on the surface is achieved, and the partial pressures and the composition of these molecules/atoms is measured [2,70]. As shown in Fig. 6, the linear change in the temperature shows variation in the desorption rate and coverage as a function of time.

Polyani-Wigner equations are used to describe the dynamics of a thermal desorption process.

$$r_{des}(\Theta) = -\frac{d\Theta}{dt} = v_n(\Theta)\cdot \exp\left(-\frac{\Delta E_{des}}{RT}\right)\cdot \Theta^n \qquad (7)$$

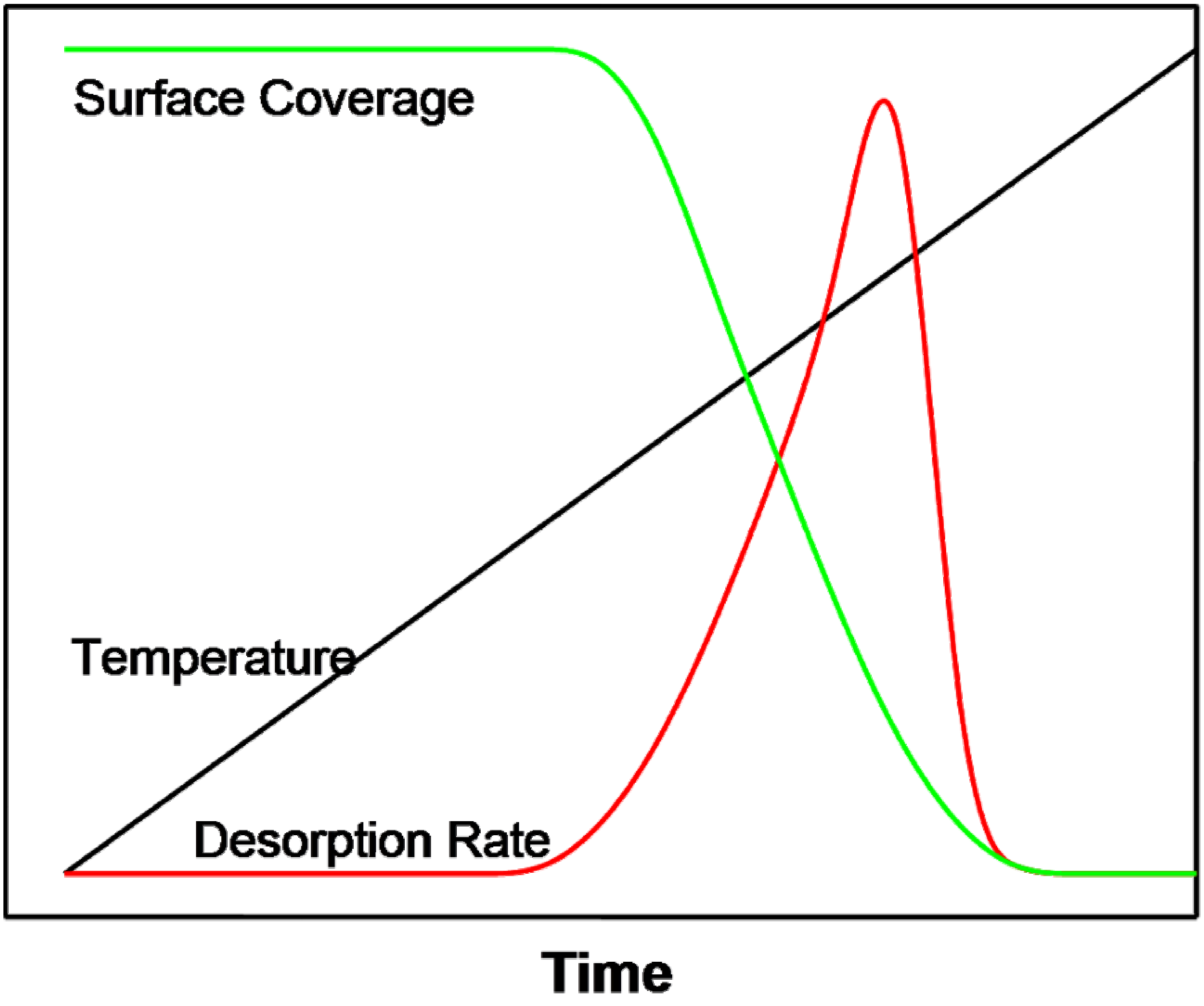

Fig. 6. Figure depicting the change in desorption rate and coverage as a function of sample temperature.

where, r_{des} is the desorption rate, Θ is the adsorbate coverage, t is the time, ν is the pre-exponential factor for desorption, n is the order of desorption, E_{des} is the activation energy of desorption, R is the universal gas constant and T is the temperature. There are numerous approximation methods available to simplify the above equation, such as, the Redhead and the leading edge analysis. In the Redhead analysis the activation parameters are assumed to be independent of the surface coverage and the desorption is supposed to follow first order kinetics. These approximations gives the following equation:

$$\Delta E_{des} = RT_{\max}\left(\ln\frac{v_1 \cdot T_{\max}}{\beta} - \ln\frac{\Delta E_{des}}{RT_{\max}}\right) \tag{8}$$

where, T_{max} is the temperature of the desorption rate maximum and β is the heating rate. On the other hand, leading edge analysis lets us determine the activation parameters depending on the temperature and coverage. A small section of the leading edge of the desorption spectra is used for analysis, which allows us to hold T and Θ constant. This leads us to the following equation:

$$\ln r_{des} = -\frac{\Delta E_{des}}{RT} + \ln v_n + n \cdot \ln \Theta \tag{9}$$

The slope of the Arrhenius plot can be used to calculate ΔE_{des}.

Sample Preparation, Performing Reactions and Gas Handling

The metal single crystals used as catalysts were cleaned by a variety of methods including Ar-ion sputtering, oxidation and annealing cycles. A W/5% Re-W /26% Re thermocouple spot welded to the back of the sample was used to monitor the temperature; the sample was resistively heated via Ta leads. Cleanliness of the sample was confirmed using XPS and AES. Low energy electron diffraction (LEED) was used to confirm and establish the long range order of the cleaned single crystal. After cleaning and performing the surface analysis, the catalyst is retracted into the reaction chamber. The catalyst is then isolated by closing the valves. The reactant gases are let into the reactor and the catalyst is slowly heated and maintained at a desired temperature. The reaction is usually done at pressures less than 20 Torr. A gas chromatograph (GC) is attached to the reactor and the gases are let into the GC after short time intervals. A six-port valve employing a 5.0 ml sample loop is utilized in between the reactor and the GC. The assembly is repeatedly pumped using a mechanical pump before admitting the gas from the reactor into the sample loop. Hydrocarbon analysis was calibrated with regular gas mixtures and was established to be linear over the concentration range of concern.

For VA experiments research grade ethylene (99.999 %) and ultra-high purity oxygen (99.98 %) were obtained from Matheson and were further purified by triple distillation method using cold liquid nitrogen trap. Similarly 99.98 % pure acetic acid was obtained from Aldrich and purified by distillation. For CO oxidation experiments, research grade CO gas (99.999 %) was obtained from Matheson and was further purified by condensation in liquid nitrogen. The purity of the gases was further ascertained by GC and mass spectroscopy techniques. The turnover frequencies (TOF's) (molecules of the product produced per surface metal site per second) were calculated from the number of product molecules produced during the reaction (total conversion < 0.5 %) using the atom density for that particular single crystal.

Gas Chromatography

Chromatography involves the separation of components using a stationary phase and a mobile phase. The mobile phase in the column carries the components of the mixture and these components are attracted towards the stationary phase with varying intensity, and hence, get separated. The separated components are then analyzed using detectors. In gas chromatography, gases such as, hydrogen, helium, nitrogen, etc., are usually used as the mobile carrier gas. In our experiments helium was used. For VA reaction Haysep-R and Poropaq-Q columns were connected in series and used to achieve necessary separation. For CO oxidation experiments a Molecular Sieve 5A column was selected. A six way valve was used to condense, trap and inject the products into the columns. Flame ionization detector (FID) and thermal conductivity detector (TCD) were used to analyze gases. Additionally a methanizer was used to convert low amounts of CO and CO_2 to methane for analysis using FID.

Flame Ionization Detector (FID)

As the name suggests, FID involves the burning of the compound using a small flame of hydrogen and air. The product is usually carried by the carrier gas (helium in our experiments). As, shown in Fig. 7, a small jet is situated in a cylindrical electrode and a few hundred volts is applied between the sample jet and the electrode. Due to the combustion of the compounds a small current consisting of stream of electrons or ions is produced and is collected at the cylindrical electrode. The current is then amplified and fed to a recorder. Obviously the application of this technique is limited to the detection of hydrocarbons, etc. Although FID has the above limitation, the advantage of using FID is that analytes in extremely low concentrations can be detected very easily. The background signal (current) due to the electrons or ions from the hydrogen flame is usually very small compared to the signal of the compounds.

In our experiments, a Varian 3400 Cx series gas chromatograph was used and helium was used with a flow rate of 30 ml/min, oxygen at 200 ml/min and hydrogen at 30 ml/min. The detector assembly was always maintained at 250 ^{o}C. A HP 3390 integrator was used to record the signal.

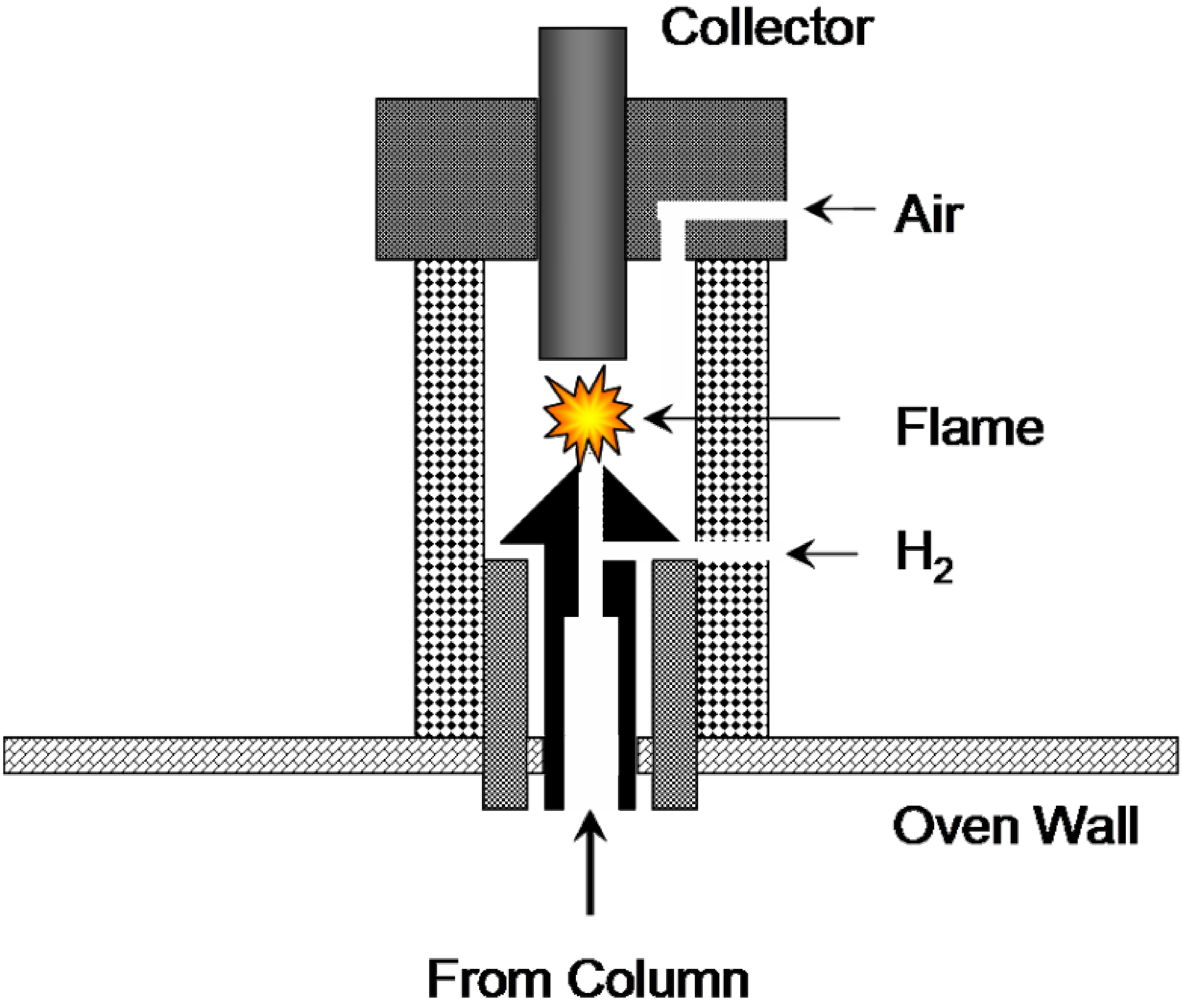

Fig. 7. Schematic diagram of the flame ignition detector (FID) used in GC.

Thermal Conductivity Detector (TCD)

As depicted in Fig. 8, four electrically heated tungsten-rhenium filaments are arranged in a Wheatstone bridge configuration is used in TCD. This configuration allows amplification of the changes in the resistance due to the change in the temperature of the filaments. Helium is usually used as the carrier gas as it has very high thermal conductivity. The flow of helium across the filaments removes heat from the filaments at a constant rate. While two of the filaments are exposed to the reference helium gas, the other two filaments are exposed to the sample also carried by the carrier helium gas. The sample after exiting the column passing through the filaments removes less heat across the filaments if its thermal conductivity is lower than helium. The temperature of the filaments depends on the thermal conductivity of the gas flowing around it. The rise in temperature is apparent from the change in the resistance and is recorded as a peak using a recorder. TCD is not a very sensitive detector (concentration of 100 % to 100 ppm) but it is non-destructive and can be applied for the detection of almost any gas.

In our experiments, a Varian Star 3400 CX series GC was used with TCD operated typically at 390 ^{o}C. Helium was used as carrier and reference gas. TCD was mainly used to detect gases such as CO and CO_2 which are not detectable using FID.

Methanizer

To detect very low concentration of CO and CO_2, methanizer is used along with a FID. As the name suggests, methanizer converts these gases to methane by reacting with hydrogen. A nickel catalyst typically heated to ~ 300 ^{o}C catalyzes CO and CO_2 hydrogenation to methane and the retention times remain unchanged.

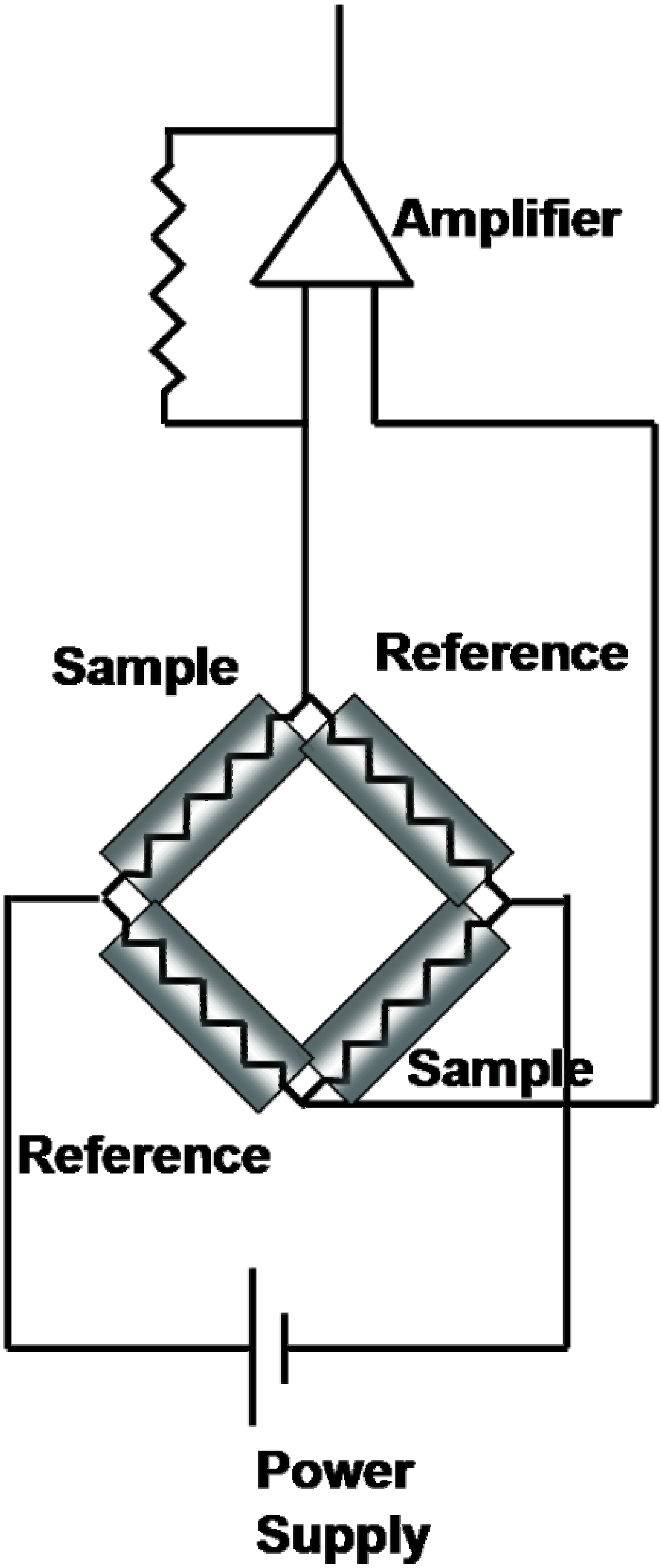

Fig. 8. Schematic diagram of the components in the thermal conductivity detector (TCD).

Methane gas is then passed into FID for detection. Hydrocarbons remain unaffected. A four way valve is employed before the methanizer to pass the gases either through the methanizer or directly to FID.

Supported Catalysts

Preparation and the Reactants

Pd/SiO_2 catalysts with a loading of 5.0 wt% and Pd 1.0 wt% metal were prepared by the incipient wet-impregnation method [77,78,79,80]. High surface area (600 m^2/g) SiO_2 (Aldrich No. 7631-86-9), with a mesh size of 230 - 400 and a pore volume of 1.1 ml/g, was used as support. A Pd^{2+} solution was prepared by dissolving $Pd(NO_3)_2$ (C.P., commercial sources) in deionized water and mixed with an equal volume of SiO_2 powder while stirring. The impregnated catalyst was left in a covered beaker for 4 hours. Finally, the precursor was dried under vacuum at 393 K overnight. To remove trace amount of impurities, such as, water and hydrocarbons, the reactant gases, C_2H_4, O_2(10%)/N_2, and air (Messer MG Industries) were purified with gas filters (Chrompack). The partial pressure of AcOH was 2.0 to 3.5 kPa, and was achieved by bubbling the reactant gas stream through AcOH (Aldrich C.P.).

All kinetics measurements were carried out at atmospheric pressure in a quartz tube micro-reactor, with 0.8 cm inner diameter and a catalyst bed (1 - 2 cm length) containing approximately 0.1 - 1.0 g. The reactants and products were analyzed with an online HP 5890 GC. A HayeSep R column, 80/100 mesh and 2 m long, connected to a FID, was used to detect VA and acetic acid. A Porapak column RT, 80/100 mesh and 1.5 m long, connected to a TCD, was used to detect CO_2, C_2H_4, VA and mixtures of O_2 and N_2. The flow rates of the gases were controlled by mass flow meters.

The catalysts were preconditioned by calcination in a 10% O_2/N_2 mixture at 673 K (30 min, 20 ml/min), followed by reduction in 100% H_2 at 573 K. Subsequently the reactor was cooled to reaction temperature in N_2. The kinetics measurements were performed under differential flow conditions, with the conversion of ethylene kept below 5%.

Characterization Techniques

X-ray Diffraction (XRD)

When an X-ray beam interacts with a structure whose repeat distance is comparable to the wavelength of X-rays, diffraction is observed. X-rays have wavelengths of a few angstroms, and hence are useful in analysis of crystalline solids. The schematic for the working of XRD is represented in Fig. 9. The principle is simple and involves the use of two parallel X-ray beams, A and B, which are incident on parallel planes P1 and P2, separated by an interplanar spacing 'd'. The resulting waves can interfere constructively to form waves A' and B' when certain geometric requirements are met. The difference in pathlength between A to A' and B to B' should be an integral number of wavelengths, λ. In 1912, W.L. Bragg recognized this relationship and deduced the Bragg's law:

$$2d \sin \theta = n \lambda \tag{10}$$

where, θ is the angle of diffraction and n is an integer.

The particle size of palladium in the heterogeneous catalysts was calculated from the line broadening of the intense peaks using the Scherrer formula:

$$D = k\lambda / \Delta \cos \theta \tag{11}$$

where, k is the Scherrer constant, λ is the wavelength of the X-rays, Δ is the full width at half-maximum (FWHM) and θ is the Bragg angle of the peak maximum. Brucker D8 diffractometer using Cu-K_α radiation was used in our studies.

Transmission Electron Microscopy (TEM)

The transmission electron microscope was developed in the 1930's after it was realized that the electron waves could be used to image a surface. The primary advantages of using electrons over X-rays are due to the properties of electron beams which make them refractable in a magnetic field and can be accelerated using electrical potential. The de Broglie equation states that the shorter the wave length better is the resolution. The resolution offered by most of the TEMs these days using electron beam traveling at 75 kV is less than 5 pico meters. Optical lenses are used in the microscopes operated by light and similarly magnetic lenses are used to focus, shape and guide the beam of electrons in TEM.

After a beam of electrons is emitted by the source (see Fig. 10), it is focused using condenser lenses and condenser apertures. The electron stream is then focused on the sample and some part of the beam is transmitted. Objective lens and objective apertures focuses the transmitted signal into an image. This is then directed towards the main phosphor screen using projector lens to obtain a viewable image.

There are several disadvantages associated with using electron microscopes. Electrons are high energy particles and interaction with any matter will result in the loss of signal along with the emission of secondary electrons, X-rays, etc. Hence, the microscope needs to be operated in high vacuum conditions and a thin specimen needs to be used to ensure penetration and transmission of electrons. This is also a destructive technique.

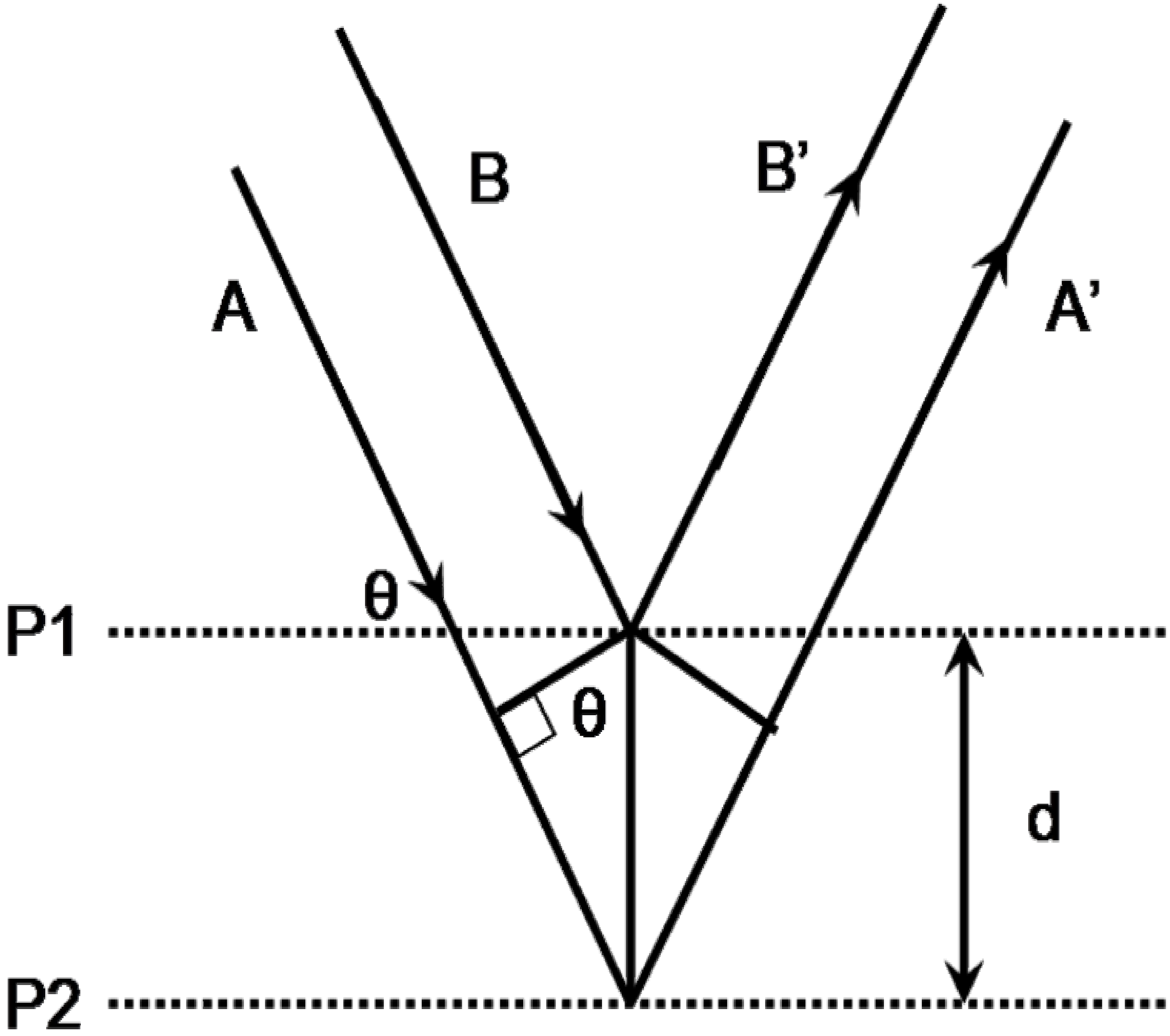

Fig. 9. Diagram illustrating the X-ray diffraction process.

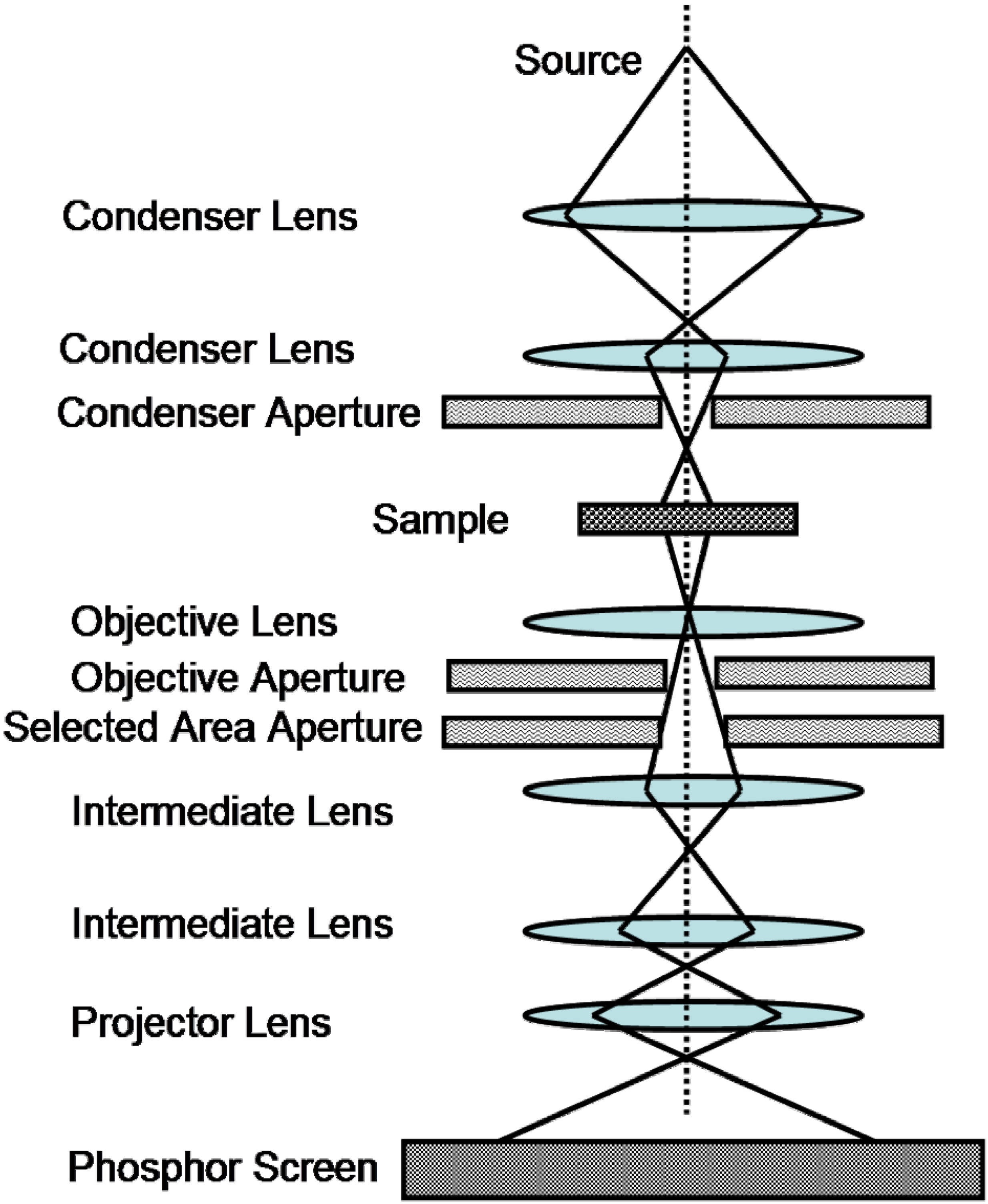

Fig. 10. Schematic diagram of the arrangement of various components used in transmission electron microscopy (TEM).

In our experiments, JOEL 2100 TEM instrument was used for the analysis of samples and typically 200 particles were counted to determine the average particle size of the metal particle. The sample was deposited and dried on a carbon grid using ethanol solvent.

Calculations of the Reaction Rates and Selectivities

C_2H_4 conversion, $X_{C_2H_4} = \frac{p_{C_2H_4,in} - p_{C_2H_4,out}}{p_{C_2H_4,in}}$, was calculated [79] from the CO_2 concentration at the reactor exit:

$$X_{C_2H_4 \rightarrow CO_2} = \frac{0.5 \cdot p_{CO_2,out}}{p_{C_2H_4,in}} \tag{12}$$

The average C_2H_4 partial pressure $\overline{p_{C_2H_4}}$ at the entrance and exit of the reactor can be used to calculate the reaction rate of ethylene by:

$$r_{C_2H_4} = \frac{\overline{p_{C_2H_4}} \cdot X_{C_2H_4} \cdot \dot{V}_{tot}}{p_0 \cdot m_{Me}} \qquad [\text{mol s}^{-1}\ \text{g}_{\text{Me}}^{-1}] \tag{13}$$

where, p_0 is the atmospheric pressure p_0, m_{Me} is the mass of the metal in the catalyst bed and the total molar flow rate is $\dot{V}_{tot}$.

Therefore, $r_{C_2H_4 \rightarrow CO_2} = \frac{\overline{p_{C_2H_4}} \cdot X_{C_2H_4 \rightarrow CO_2} \cdot \dot{V}_{tot}}{p_0 \cdot m_{Me}}$ $[\text{mol s}^{-1}\ \text{g}_{\text{Me}}^{-1}]$ (14)

the VA formation rate is given by:

$$r_{C_2H_4 \rightarrow VA} = \frac{\overline{p_{C_2H_4}} \cdot X_{C_2H_4 \rightarrow VA} \cdot \dot{V}_{tot}}{p_0 \cdot m_{Me}} \tag{15}$$

while $X_{C_2H_4 \rightarrow VA} = \frac{p_{VA,out}}{p_{C_2H_4,in}}$ (16)

During the synthesis of VA, the selectivity (S) to CO_2 formation, expressed as the fraction of C_2H_4 consumed for CO_2 formation *vs.* the total amount of C_2H_4 consumed, is shown in eq. (8):

$$S = \frac{0.5 \cdot p_{CO_2,out}}{p_{C_2H_4,in} - p_{C_2H_4,out}} = \frac{r_{C_2H_4 \rightarrow CO_2}}{r_{C_2H_4}} \qquad (17)$$

The turnover frequencies, s^{-1}, were calculated from the mass based reaction rates according to eq. (9):

$$r_{TOF} = \frac{r_{mass\,based} \cdot M_{Me}}{D} \ [s^{-1}] \qquad (18)$$

where M_{Me} is the weight of the metal and D is the dispersion of active metal. The dispersion of Pd, D, of the fresh reduced 5wt% Pd/SiO_2 catalyst was estimated to be approximately 40%, corresponding to a Pd average particle size of 3.8 nm, from the broadening of the Pd (111) diffraction line ($2\theta = 40.2^{o}$).

RESULTS AND DISCUSSION

Palladium-only Catalysts

Supported Pd Catalysts

In 1960 Moiseev et al. investigated the homogenous liquid-phase production of VA using a $[PdCl_2(C_2H_4)]_2$ complex catalyst [54]. The same was studied by vapor phase oxidation of ethylene and acetic acid by Samanos et al. in 1971 on Pd catalysts supported by SiO_2 and Al_2O_3 [63]. In this study, various parameters such as, the effect of Pd dispersion, the partial pressures of the reactants and water vapor were evaluated. The proposed mechanism recognized the importance of the formation of CO_2 through the combustion of ethylene (first step of the mechanism) along with the formation of VA (second step). The synthesis of VA itself comprised of two steps; first, where palladium acetate was formed due to the oxidation of metallic palladium, and second, where ethylene reacts with palladium acetate forming VA and metallic palladium. The requirement of presence of sodium acetate was also mentioned. This was one of the initial studies aimed at elucidating the mechanistic aspects of the reaction. In summary, the mechanistic route was:

i. $Pd + ½ O_2 + 2 AcOH \rightarrow Pd(OAc)_2 + H_2O$ (19)

ii. $Pd(Oac)_2 + AcO \rightarrow Pd(OAC)_3$ (20)

iii. $Pd(Oac)_3 + C_2H_4 \rightarrow AcO\text{-}CH{=}CH_2 + AcOH + Pd$ (21)

Almost at the same time, Nakamura and Yasui studied the mechanistic aspects of VA synthesis on Pd-based catalysts [66,81]. They investigated the promotional effect of adding alkali metals, the effect of reaction orders with respect to acetic acid and ethylene. Furthermore, the heterogeneous process of production of VA was identified to be more attractive since there was less corrosion and did not require the presence of chloride. They found evidence to suggest that VA is produced in the gas phase reaction by the coupling between dissociatively adsorbed ethylene and dissociatively adsorbed acetic acid. The mechanism was supposed to proceed as follows: (1) Due to the abstraction of hydrogen by Pd, ethylene is dissociatively adsorbed. (2) Oxygen is dissociatively adsorbed on Pd. (3) Acetic acid (AA) is associatively adsorbed on Pd. (4) Step (2) leads to the abstraction of hydrogen from associatively adsorbed acetic acid. (5) Adosorbed ethylene couples with dissociatively adsorbed acetic acid to form VA.

Schematically the reaction proceeds as follows:

i. $C_2H_4 + 2\ Pd \leftrightarrow CH_2\text{-}CH\text{-}Pd + PdH$ (22)
ii. $O_2 + 2Pd \leftrightarrow 2Pd\text{-}O$ (23)
iii. $CH_3COOH + Pd \leftrightarrow Pd\text{-}CH_3COOH_{ad}$ (24)
iv. $Pd\text{-}CH_3COOH_{ad} + PdO \leftrightarrow Pd\text{-}OCOCH_3 + Pd\text{-}OH$ (25)
v. $Pd\text{-}OCOCH_3 + CH_2CH\text{-}Pd \leftrightarrow Pd\text{-}CH_2CHOCOCH_3\ ad + Pd$ (26)
vi. $Pd\text{-}CH_2CHOCOCH_{3\ ad} \leftrightarrow Pd + VA$ (27)
vii. $Pd\text{-}OH + PdH \leftrightarrow Pd\text{-}H_2O_{ad} + Pd$ (28)
viii. $Pd\text{-}H_2O_{ad} \leftrightarrow Pd + H_2O$ (29)

The rate determining step has been suggested to be the step (v), that is, the combination of dissociatively adsorbed acetic acid with dissociatively adsorbed ethylene. Simultaneously, the side reaction involves the formation of CO_2 from ethylene and acetic acid.

TEM and XRD of Fresh Catalysts

The TEM image in Fig. 11 a and b clearly shows the Pd particles to be highly dispersed on the SiO_2 surface [78]. The Pd particle sizes are distributed over the range of 1.5 – 8.5 and 1.5 – 4.5 nm for the reduced Pd(5 wt%)/SiO_2 and Pd(1 wt%)/SiO_2 catalysts (see Fig. 11 c and d), respectively. The average particle size was estimated to be 4.2 ± 0.2 and 2.5 ± 0.1 nm, respectively.

The X-ray powder diffraction data were collected with a Bruker D8 diffractometer using CuKα radiation [77,78]. The samples were scanned over the 2θ range from 36 to 52^o using 0.2^o per step for the Pd (5.0 wt%)/SiO_2 and 0.04^o steps for the Pd (1.0 wt%)/SiO_2. Fig. 12 shows the XRD scans of the reduced catalysts for Pd (5 wt%)/SiO_2 (Fig. 12 a) and Pd (1 wt%)/SiO_2 (Fig. 12 c) [77,78]. For the reduced Pd (5 wt%)/SiO_2 catalyst diffraction features were observed at Bragg angles of 40.2^o and 46.9^o which correspond to the Pd <111> and <200> planes, respectively. The Pd particle size was estimated using the Scherrer formula [82] where the particle diameter (D) in the direction perpendicular to the diffracting plane (111), $2\theta = 40.2^o$, was obtained from the width of the diffraction profile. The Pd particle sizes before reaction for each catalyst studied are shown in Table 1. For the reduced Pd(1 wt%)/SiO_2 catalyst (as shown in Fig. 12 c) the features at $2\theta = 40.1^o$ and 46.8^o were detected corresponding to the Pd<111> and Pd<200> planes, respectively. The average particle size before reaction was estimated to be 3.8 and 2.8 nm, respectively for Pd(5 wt%)/SiO_2 and Pd(1 wt%)/SiO_2 catalysts.

VA Reaction Rate Measurements

Using Pd/SiO_2 catalyst about 80-90% selectivity has been reported [63]. In our group we have used Pd(5.0 wt%) and Pd(1.0 wt%)/SiO_2 catalysts prepared by wet impregnation method

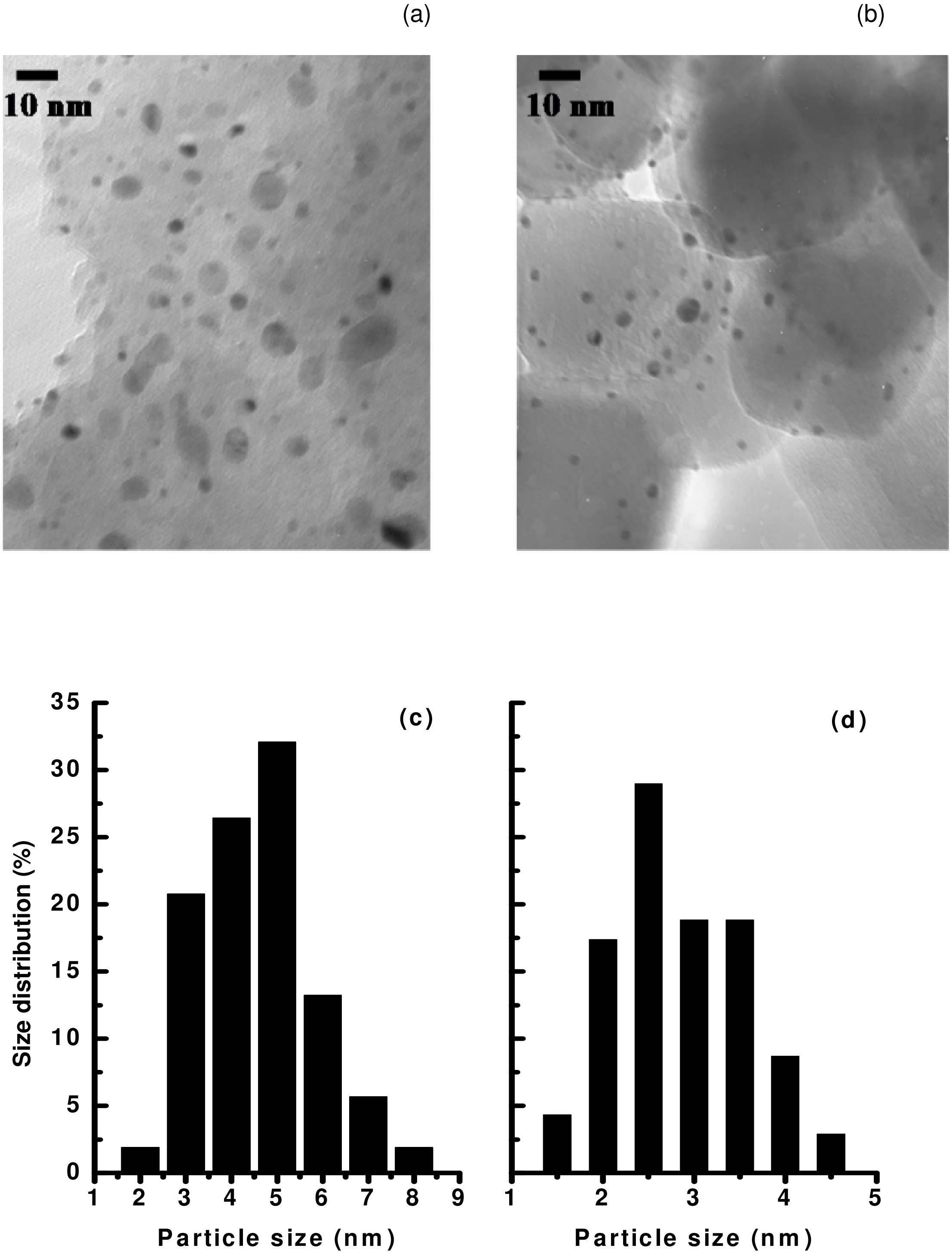

Fig. 11. TEM micrographs of the reduced (a) Pd(5 wt%)/SiO$_2$ and (b) Pd(1 wt%)/SiO$_2$ catalysts and the corresponding particle size distributions (c) and (d).

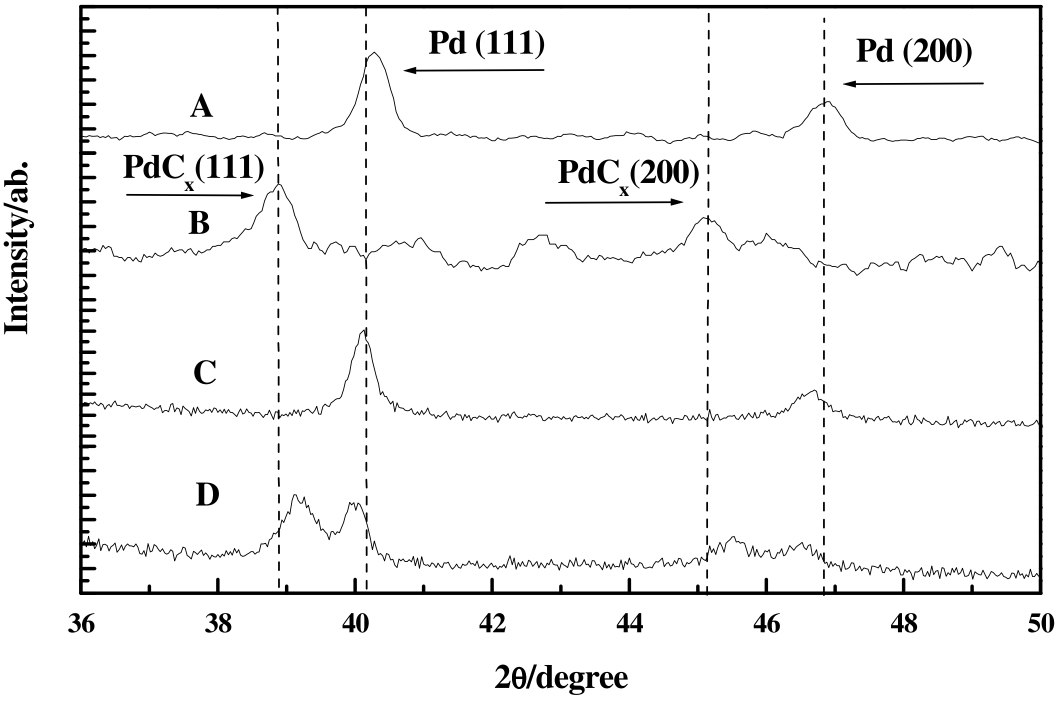

Fig. 12. (A) XRD of the Pd(5.0 wt%)/SiO_2 catalyst after reduction at 673 K in 20 ml/min O_2 (10%) / N_2, 30 min, then 573 K in 20 ml/min H_2 for 30 min; (B) after reaction for 10 hours, at $p_{C_2H_4}$ = 7.5 kPa, p_{O_2} = 1.0 kPa, p_{AcOH} = 2.0 kPa, with remainder N_2; flow rate: 60 ml/min, at 413 K; (C) XRD of the Pd(1.0 wt%)/SiO_2 catalyst after reduction; and (D) after reaction as mentioned above for 16.7 hours.

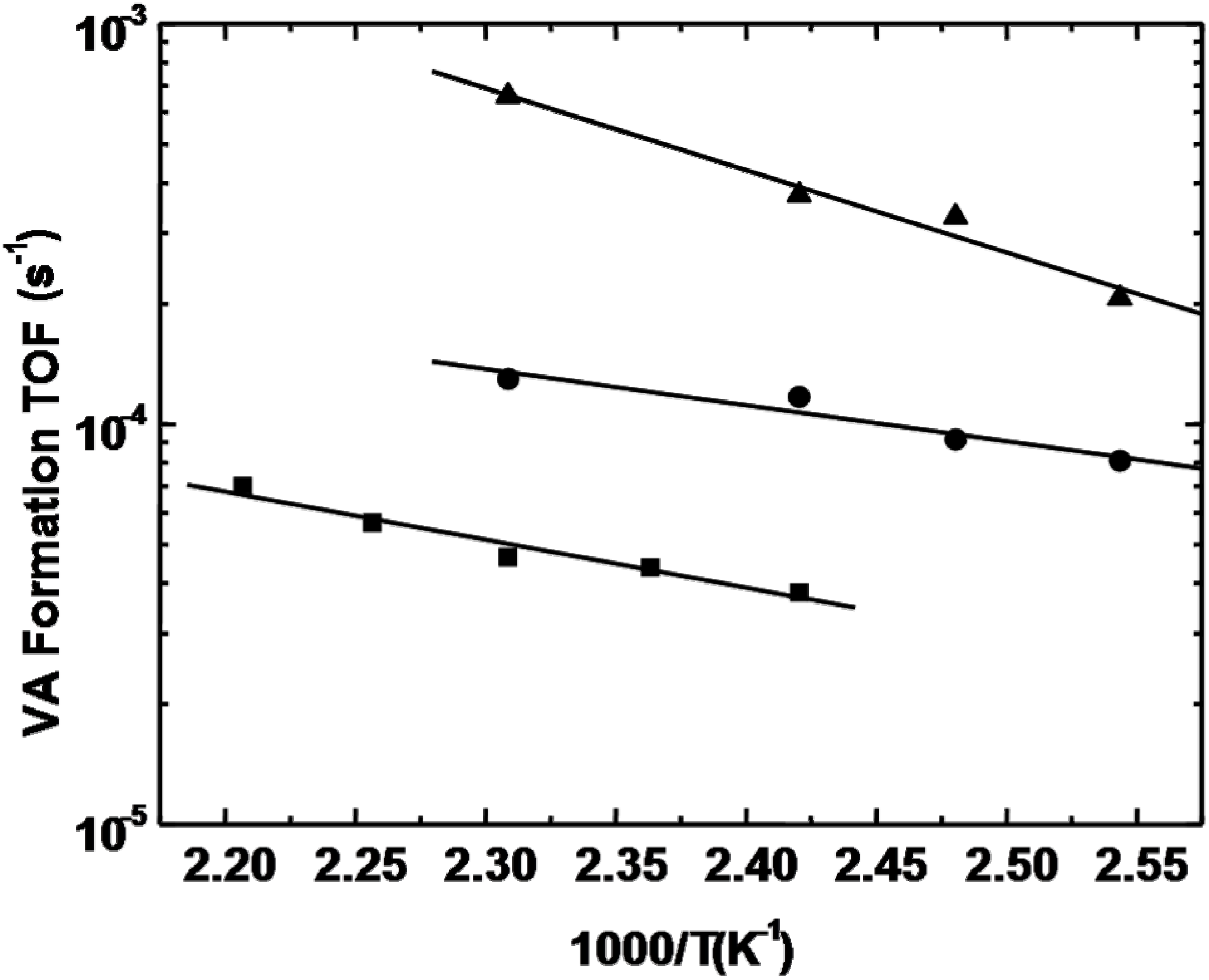

Fig. 13. Arrhenius plot of VA formation rate on Pd(100) (■), Pd(5 wt%)/SiO$_2$ (●) and Pd(1 wt%)/SiO$_2$ (▲) at various temperatures. For Pd(100), p_{O_2} = 2.0 Torr, $p_{C_2H_4}$ = 9.0 Torr, p_{AcOH} = 4.0 Torr; for Pd(5 wt%)/SiO$_2$ and Pd(1 wt%)/SiO$_2$ catalysts p_{O_2} = 7.6 Torr, $p_{C_2H_4}$ = 57.0 Torr, p_{AcOH} = 12.0 Torr, the remainder N$_2$; flow rate: 30 – 60 ml/min, catalyst weight: 0.1 – 1.6 g.

Table 1. Pd particle sizes measured by TEM before* and after VA synthesis reaction**

Sample	**XRD**		**TEM**	
	Diameter/nm	Dispersion/%	Diameter/nm	Dispersion/%
Pd(5 wt%)/SiO_2 reduced	3.8	37.5	4.2	30
Pd(5 wt%)/SiO_2 reacted	4.2	30	5.5	22
Pd(1 wt%)/SiO_2 reduced	2.8	40	2.5	40
Pd(1 wt%)/SiO_2 reacted	3.7	32	3.5	36

* Treated in O_2(10%)/N_2 mixture at 673 K for 30 min, then reduced in H_2 at 573 K for 30 min.

** $p_{C_2H_4}$: 7.5 kPa, p_{O_2} : 1.0 kPa, p_{AcOH} : 2.0 kPa, the remainder N_2, at 413 K; 10 hours for Pd(5 wt%)/SiO_2 and 16.7 hours for Pd(1 wt%)/SiO_2.

Table 2. List of all the catalysts used in the experiments and the corresponding kinetic data obtained for VA synthesis reaction.

Catalysts	Particle size	K 10^{-3} (sec^{-1})	α	β	E_a (kJ/mol)	Selectivity (%)	Loss of initial activity(%)
Pd(100)	~ 1 cm	0.11	-0.40	0.50	23.00	-	~60
Pd(5 wt%)/SiO_2	4.2 nm	0.15	-0.60	0.12	17.3	~85	~50
Pd(1 wt%)/SiO_2	2.5 nm	1.32	-0.34	0.18	39.0	~90	~35
Pd(1 wt%)-Au(0.5 wt%)/ SiO_2	3.2 nm	25.0-50.0	0.38	0.21	15.0-40.0	~96	~25

[78]. Fig. 13 shows the temperature dependent reaction rates for VA synthesis on Pd-only catalysts. The reaction rate over the Pd(1 wt%)/SiO_2 is higher than that for Pd(5 wt%)/SiO_2 [78]. In Fig. 14 the variation of VA selectivity on supported Pd catalysts as a function of temperature is represented. As expected the selectivity decreases due to ethylene oxidation as the reaction temperature increases and the catalyst with smaller Pd particles shows higher selectivity to VA formation. The dependence of reaction rate and selectivity on the particle size suggests a degree of structure sensitivity. The corresponding E_a was determined to be higher for supported catalyst with smaller Pd particles (39.0 kJ/mol) than for the catalyst with larger Pd particles (17.3 kJ/mol). Typically, on promoted 2.0 wt% Pd/SiO_2 and 5.0 wt% Pd/Al_2O_3 catalysts the E_a was reported to be close to 30.0 kJ/mol [63,81].

As shown in Fig. 15, by using Pd(1.0wt%)/SiO_2 catalyst and changing the partial pressure of ethylene ($p_{C_2H_4}$) in the range of 5.0 – 15.0 kPa and by fixing the p_{O_2} at 1.0 kPa and p_{AcoH} at 2.0 kPa, the reaction rate decreased from 0.35×10^{-3} to 0.24×10^{-3} s^{-1}. The selectivity also decreased from 95% to 84%. Similarly using a Pd(5.0wt%)/SiO_2 catalyst lower rates were observed and the change was from 0.14×10^{-3} to 0.08×10^{-3} s^{-1} while the corresponding selectivity also dropped from 94% to 80%. However, as shown in Fig. 16, by fixing $p_{C_2H_4}$ at 7.5 kPa and increasing p_{O_2} from 1.0 to 8.4 kPa, the VA formation rate increased from 0.34×10^{-3} to 0.51×10^{-3} s^{-1} and the selectivity fell from 94% to 86% for Pd(1.0wt%)/SiO_2 catalyst. Using Pd(5.0wt%)/SiO_2 catalysts under similar conditions the reaction rate increased from 0.11×10^{-3} to 0.14×10^{-3} s^{-1} while the selectivity decreased from 92% to 76%.

The reaction orders with respect to C_2H_4 and O_2 were calculated by fitting to a power rate law as follows:

$$r_{VA} = k \cdot p_{C_2H_4}^{a} \cdot p_{O_2}^{\beta} \tag{30}$$

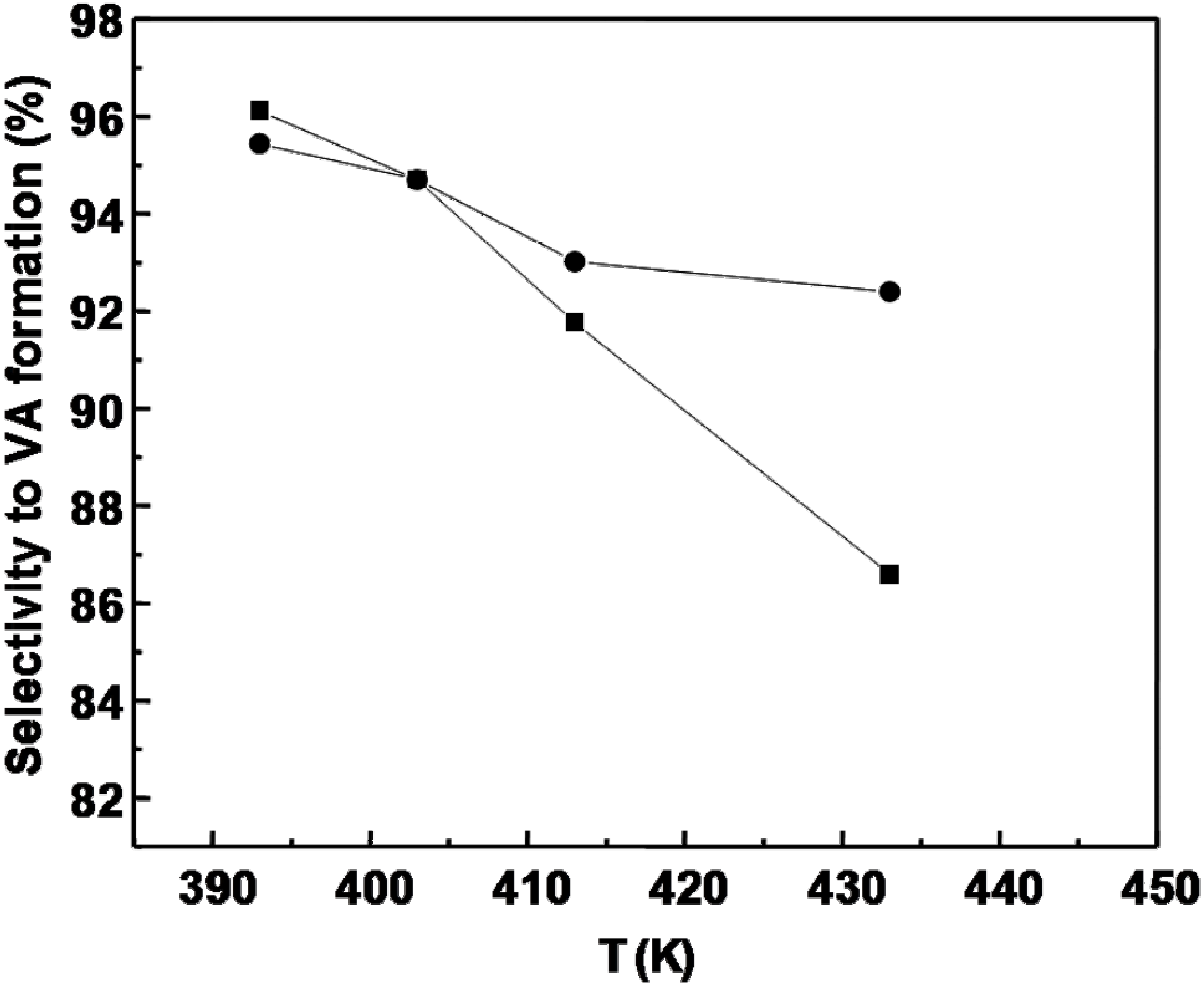

Fig. 14. VA synthesis versus temperature over (●) Pd(1 wt%)/SiO$_2$ and (■) Pd(5 wt%)/SiO$_2$ catalysts. $p_{C_2H_4}$ = 7.5 kPa, p_{O_2} = 1.0 kPa, p_{AcOH} = 2.0 kPa, the remainder N$_2$; flow rate: 60 ml/min, catalyst weight = 1.2 g.

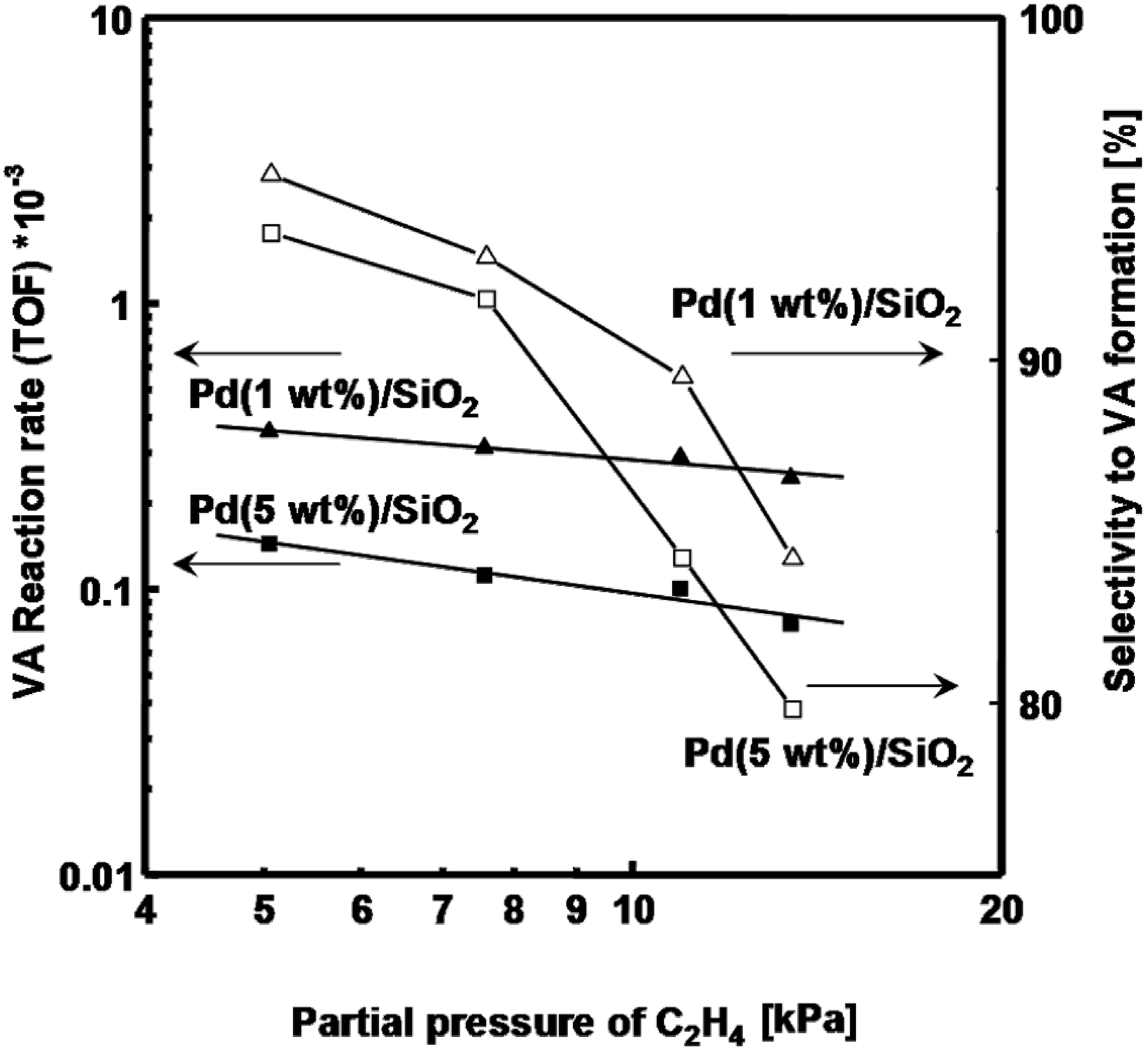

Fig. 15. VA reaction rates (▲: Pd(1 wt%)/SiO_2 , ■: Pd(5 wt%)/SiO_2) and selectivities (△:Pd(1 wt%)/SiO_2, □: Pd(5 wt%)/SiO_2) as a function of the C_2H_4 partial pressure at 413 K. $p_{C_2H_4}$ = 5.0-15.0 kPa, p_{O_2} = 1.0 kPa, p_{AcOH} = 2.0 kPa, the remainder N_2; flow rate = 30-60 ml/min, catalyst: 1.2 – 2.0 g.

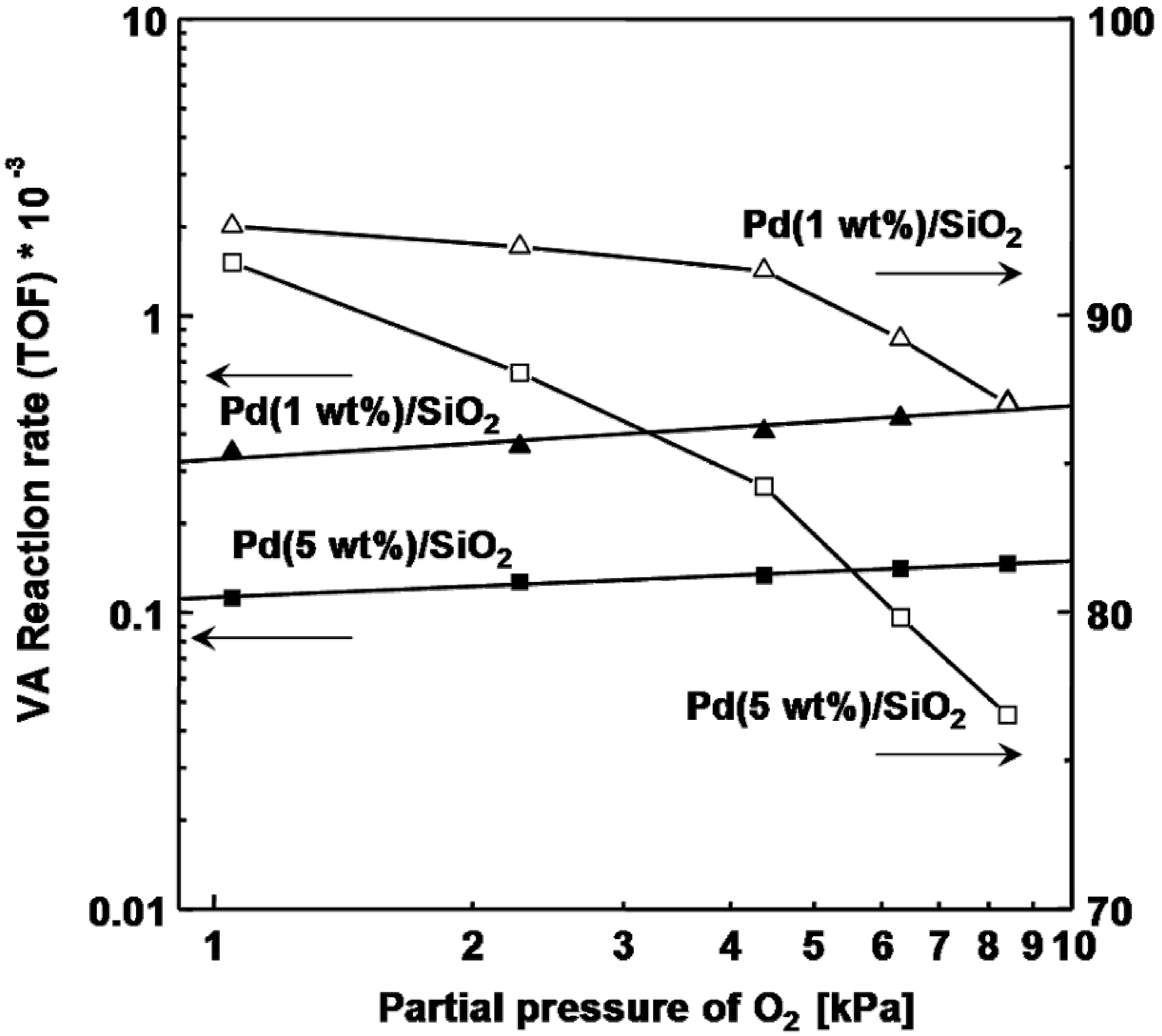

Fig. 16. VA reaction rates (▲: Pd(1 wt%)/SiO$_2$, ■: Pd(5 wt%)/SiO$_2$) and selectivities (△:Pd(1 wt%)/SiO$_2$, □: Pd(5 wt%)/SiO$_2$) as a function of the O$_2$ partial pressure at 413 K. $p_{C_2H_4}$ = 7.5 kPa, p_{O_2} = 1.0 – 10.0 kPa, p_{AcOH} = 2.0 kPa, the remainder N$_2$; flow rate = 30 – 60 ml/min, catalyst: 1.2 – 2.0 g.

As listed in Table 2, similar negative orders with respect to C_2H_4 and positive order with respect to O_2 have been obtained for all the catalysts studied. These results are in agreement with the results reported for a Pd(2.0 wt%)/SiO_2 catalyst [63]. However, at approximately 500 kPa over a Pd(5.0wt%)/Al_2O_3 catalyst Nakamura, et al., reported [81] that the reactivity was enhanced with an increase in $p_{C_2H_4}$ from 50 to 200 kPa but decreased slightly with a further increase in $p_{C_2H_4}$. The reaction order with respect to acetic acid has been a point of contention with reported values ranging from 0 to 0.5 to 1.0 [63,78,83]. On Pd(5.0 wt%)/SiO_2 and Pd(1.0 wt%)/SiO_2 catalysts we observed the reaction order with respect to acetic acid to be zero [78].

The negative order for C_2H_4 may be due to the stronger adsorption of ethylene and its derivate surface species, like ethylidene and ethylidyne. With the increase in the operating pressure the coverages of these ethylene species increase. Due to competitive adsorption with other species cause a decrease in the coverages of species like acetate and oxygen required for VA synthesis. The increase of O_2 pressure, on the other hand, improves the coverage of active surface oxygen species and leads to an increase in the VA formation rate.

Catalyst Deactivation

The catalysts were observed to maintain a steady activity after initial induction period within the first 100 mins. The catalytic stability was observed to be strongly dependent on the particle size. Pd(1.0 wt%)/SiO_2 exhibited less deactivation compared to other Pd-only catalysts after the initial induction period [84]. For Pd/SiO_2 catalysts (as illustrated in Fig. 17), the onset of reactivity for VA formation was observed from ca. 20 min time-on-stream. After 1000 min of reaction time the reactivity of ca. 33% for Pd(1.0 wt%)/SiO_2 and 50% for Pd(5.0 wt%)/SiO_2 was lost in comparison to their maximum rates (see Table 2). Deactivation was observed to be very slow and was mainly attributed to sintering and formation of carbon on the surface [77,78].

Sintering

After reaction, sintering was observed and using TEM the average particle size increased to 5.5 and 3.5 nm for Pd(5.0 wt%) and Pd(1.0 wt%), respectively (see Fig. 18). For Pd (5 wt%)/SiO_2 (Fig. 12 b) and Pd (1 wt%)/SiO_2 (Fig. 12 d), after VA synthesis reaction the peak intensities reduced significantly and the features corresponding to the <111> and <200> planes shifted downward to 38.9^o and 45.0^o, respectively. Using XRD the average particle size was estimated to be 4.2 ± 0.2 and 3.7 ± 0.1 nm, respectively. Thus, the average Pd particle sizes obtained by TEM were close to the sizes estimated by XRD and the trend exhibited by the catalysts before and after the reaction was identical as indicated in Table 1.

For the reacted Pd(1 wt%)/SiO_2 catalyst (as shown in Fig. 12 d) the features at $2\theta = 40.1^o$ and 46.8^o were detected corresponding to the Pd<111> and Pd<200> planes, respectively, which were observed to be split. Hence, two distinct peaks at 40.0^o, and 39.1^o were observed for the Pd <111> plane. As shown in Figs. 12 b and d, the downward shift of all reflections for the reacted catalysts indicate the formation of Pd carbides (PdC_x ($x \approx 0.13$)) [81,85-88]. Kaszkur [89,90] observed a downshift caused by the decrease in the Pd particles size from 3.5 to 1.5 nm with a simultaneous reduction in the peak intensity. The reduction in the particle size from Pd(5 wt%)/SiO_2 to Pd(1 wt%)/SiO_2 catalysts hence causes the relative downshift of the XRD reflections in our case. The peaks at 34.0^o and 42.5^o, assigned to the <101> and <110> planes of PdO, are not evident for either catalyst.

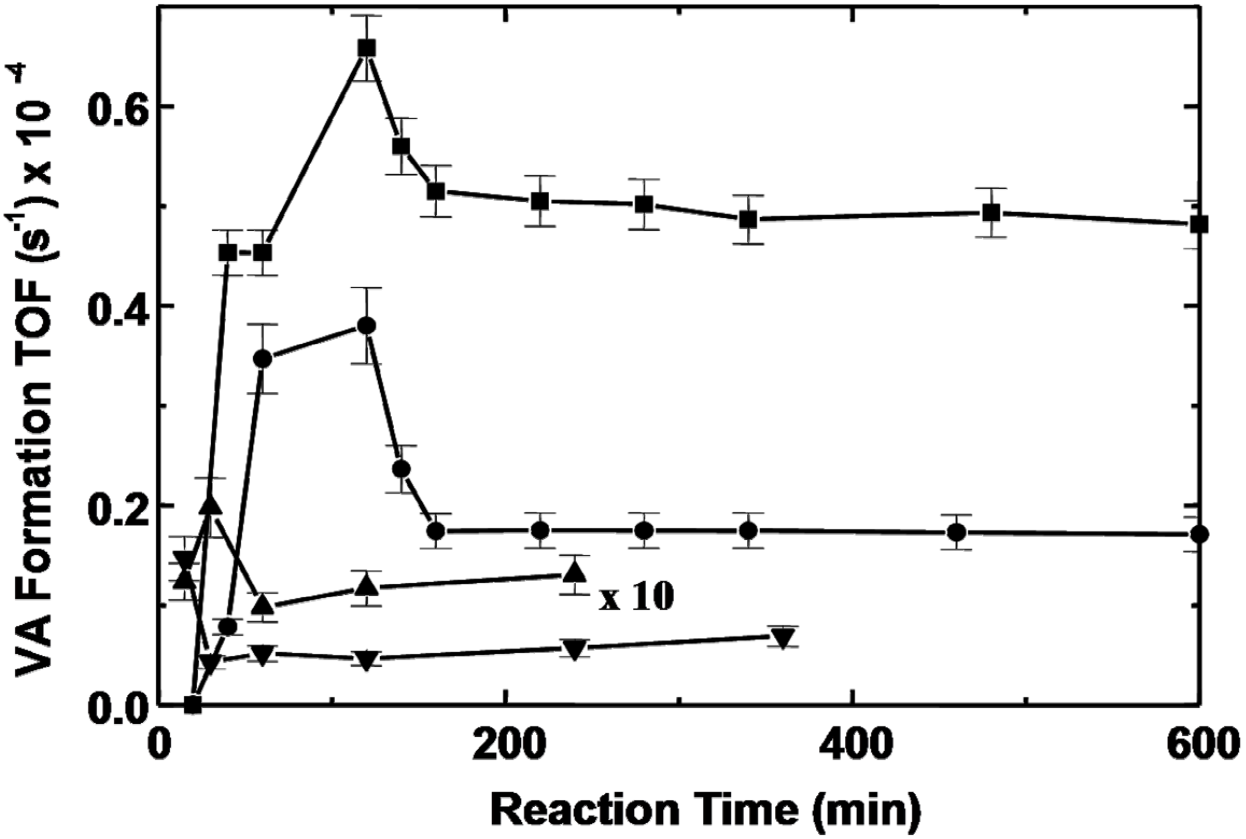

Fig. 17. VA reaction rate as a function of time on Pd(100) catalyst at 413 (▲) and 433 K (▼); p_{O_2} = 5.2 Torr, $p_{C_2H_4}$ = 21.0 Torr, p_{AcOH} = 8.0 Torr; on Pd (1 wt%)/SiO$_2$ (■) and Pd(5 wt%)/SiO$_2$ (●) catalysts at 443 K; p_{O_2} = 7.6 Torr, $p_{C_2H_4}$ = 57.0 Torr, p_{AcOH} = 12.0 Torr, the remainder is N$_2$; flow rate: 30 – 60 ml/min; catalyst weight: 0.1 – 1.6 g.

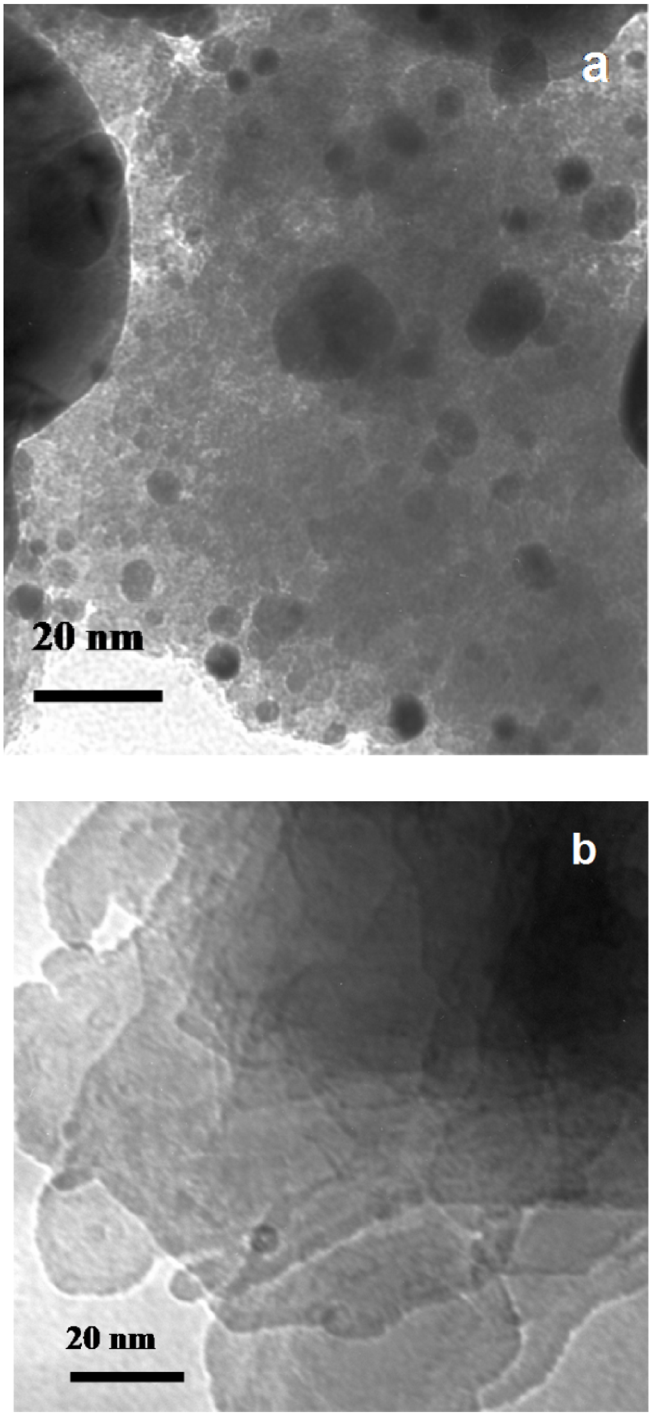

Fig. 18. TEM images of (a) Pd(5 wt%)/SiO_2 and (b) Pd(1 wt%)/SiO_2 catalysts after VA synthesis reaction for 10 and 16.7 hours, respectively at $p_{C_2H_4}$ = 7.5 kPa, p_{O_2} =1.0 kPa, p_{AcOH} =2.0 kPa, with remainder N_2; flow rate: 60 ml/min, at 413 K.

Formation of Pd Carbide

The formation of carbides over supported Pd catalysts in the gas phase acetoxylation was first reported in 1970 [81]. However, this species was fully defined as Pd carbide (PdC_x) a decade later [91]. In the reactions involving hydrocarbons interstitial carbon in Pd may alter the bulk and surface structure significantly and eventually lead to catalytic deactivation [85-88,92-98].

The stability of the catalyst for VA synthesis is inherently related to the extent of formation of carbon on the surface, and hence, a measure of the deactivation is a good parameter to judge the extent of formation of Pd carbide. As mentioned earlier, the catalytic stability for Pd-only catalysts was investigated and it was observed that during the course of the VA reaction the loss of maximum reactivity of the catalysts was related to the particle size. For example, using Pd(1.0 wt%)/SiO_2 catalyst about 33 % activity was lost where as using Pd(5.0 wt%)/SiO_2 about 50 % activity was lost (see Fig. 17).

For Pd(5 wt%)/SiO_2 catalyst, as depicted in Fig. 19 A, the reflections of Pd phase for the reduced catalyst, indexed as <111> and <200> at a Bragg angle of 40.2° and 46.9°, respectively, correspond to a lattice constant of $a_0 = 0.389$ nm. These features shift to 38.8° and 45.2° for the reacted catalyst (see Fig. 19 B) yielding a lattice constant of approximately $a_0 = 0.399$ nm. The apparent increase in the lattice constant indicates the formation of interstitial carbon. Carbon diffuses into bulk of Pd to form PdC_x. The subscript, x, in PdC_x was determined to be 0.13 – 0.15 [86,94,87], according to the 2θ of Pd <111> at 38.8°. After treating the reacted catalyst in H_2 at 623 K for 4 hours, a split in all the peaks was observed as shown in Fig. 19 C. A doublet peaks located at 39.3° and 40.0° indicate that at least two Pd <111> phases co-existed on SiO_2 surface, corresponding to carbide-containing and carbide-free phase.

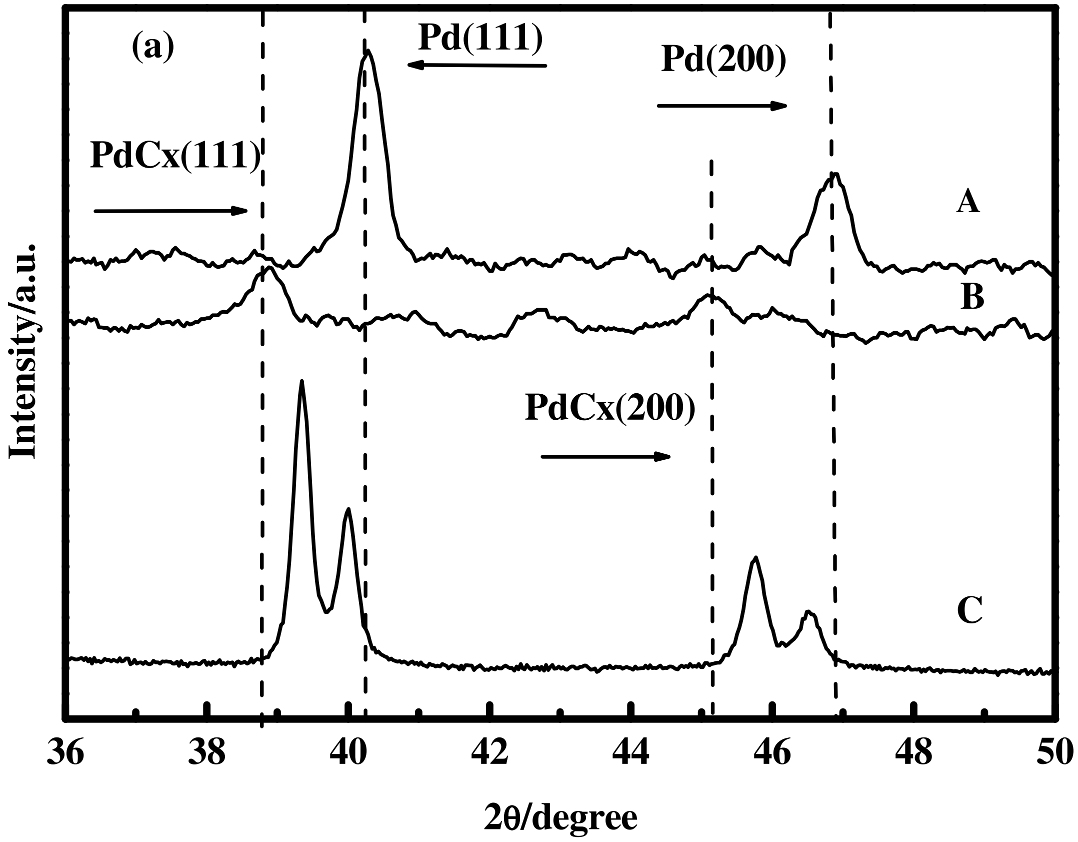

Fig. 19. XRD pattern of Pd(5 wt%)/SiO_2 catalysts. A: reduced; B: reacted; C: reacted with H_2 treatment at 623 K for 4 hours.

As shown in Fig. 20 A, the XRD pattern of the reduced Pd(1 wt%)/SiO_2 catalyst is similar to that of the Pd(5 wt%)/SiO_2 catalyst except for the peaks at Pd <111> and <200>. These peaks are lower than the latter by 0.1° which might be due to the reduction of Pd particle size [90]. Also, for Pd(1.0 wt%)/SiO_2 catalyst (see Fig. 20 B), splitting of the peaks can be observed. The peak at 40.0° is indicative of the presence of some pure Pd particles due to very little interaction with deposited carbon. The other peak at 39.2°, higher than the peak at 38.8° observed for the Pd(5.0 wt%)/SiO_2 catalyst, suggests the formation of intermediate PdC_x phases. The Pd phase was fully restored back to a clean Pd phase after H_2 treatment for Pd(1.0 wt%)/SiO_2 catalyst as shown in Fig. 20 C. Hence, H_2 treatment seems to be an effective way to remove the carbon from the bulk of Pd, which is consistent with the previous studies [87].

Ziemecki et al [87] reported that the Pd-C phase could be formed when Pd metal was heated in a carbon-containing gas, such as ethylene, carbon monoxide and acetylene. In this process, a carbonaceous overlayer was supposed to be formed on Pd surface initially, followed by the diffusion of the activated carbon atoms into the bulk of Pd. Studies using neutron diffraction [87,91] and XRD [86,94,98] have demonstrated that the carbon atoms occupy octahedral voids in the bulk of PdC_x, and that leads to Pd lattice expansion. As a result, the downshift of the Bragg diffraction angle for the Pd crystallite is decided by the carbon level in the PdC_x phase. The process of carbide formation [86-88,94] is usually thought to be a diffusion-limited and comes to an end in a few minutes above 373 K in hydrocarbon. The reacted catalyst can be decarbonized by heating in H_2 at 570 K for 2 hours [98] or in air at 473 K for 20 min [91]. In this study, the XRD results have demonstrated the formation of Pd carbides in VA synthesis over the two supported mono-Pd catalysts. After reaction, the significant downshift of the main XRD reflections of Pd <111> and <200> for the Pd(5 wt%)/ SiO_2 (3.8 nm of Pd

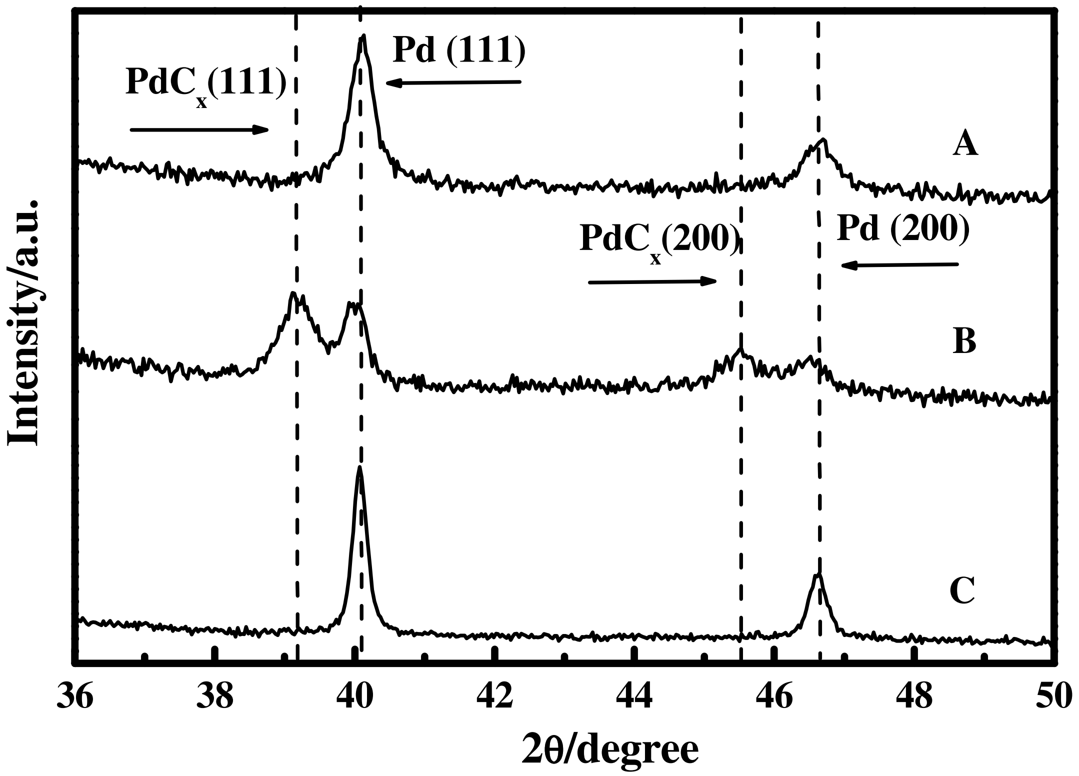

Fig. 20. XRD pattern of Pd(1 wt%)/SiO$_2$ catalysts. A: reduced; B: reacted; C: reacted with H$_2$ treatment at 623 K for 4 hours.

particles), see Fig. 19, indicates the formation of PdC_x with 0.13-0.15 of x; while the split peaks at <111> and <200> for the Pd(1 wt%)/SiO_2 (2.6 nm of Pd particles), see Fig. 20, are an indicative of the coexistence of PdC_x ($x<0.13$) and pure Pd phases.

It seems that the small Pd particles exhibit relatively high resistance to PdC_x formation. Two plausible reasons are assumed to be responsible for the less amount of PdC_x in the Pd(1 wt%)/SiO_2 catalyst: i) an excess of oxygen may be adsorbed on the small Pd cluster surface in comparison with the large Pd particle, thereby enhancing the combustion of carbon species and reducing the interaction between carbon and Pd. Previous studies [99,100] have shown that Pd particles undergo a metal to nonmetal transition at approximately 2.5 nm which could lead significantly altered chemical properties. That, in turn, could influence the rate of dissociative adsorption of oxygen; and/or ii) the rates of decomposition of hydrocarbon and diffusion of deposit carbon into the small Pd clusters may be lower than that for the large Pd particles reducing the formation of carbides. In a model catalytic system and XPS analysis the amount of carbon-containing species formed by ethylene adsorption on Pd/Al_2O_3/NiAl (110) was investigated by Frank et al. [101,102]. It was observed that approximately 30% of the initial carbon species still stayed on a 4 nm Pd particles while ca. 10% existed on a 0.8 nm Pd clusters on heating from 90 to 300 K. It has been revealed that the ability of donating electrons into the π^*-orbital of ethylene increases with increasing the Pd particles [15], thus, enhancing the binding energy of ethylene on the larger Pd particles and also leading to the decomposition of adsorbed ethylene. On the other hand, the carbon from the decomposition of adsorbed acetic acid cannot be ruled out.

Origin of CO_2 By-product

Ethylene combustion (eq. 30) has received considerable attention because the reaction occurs at low temperatures [103-108].

$$C_2H_4 + 3O_2 \rightarrow 2CO_2 + 2H_2O \tag{30}$$

Previous studies have confirmed that ethylene combustion is the primary side reaction in the synthesis of VA on Pd-based catalysts [55,60,63,78,79,81]. It has been proposed that alkene combustion on single crystal Pd(100) can proceed via two routes [109]: (i) indirect combustion, where CO_2 is produced by the reaction of adsorbed carbon and oxygen; and (ii) oxygen-activated combustion or a direct mechanism, where oxygen reacts with hydrogen and carbon from the alkene by breaking a C-H bond to form CO_2 and H_2O. In particular, the latter mechanism was suggested to be responsible for ethylene combustion at or below 400 K.

Reducing ethylene combustion during VA synthesis is crucial for optimizing the efficiency of this important industrial reaction. Although the kinetics of VA synthesis has been addressed [106-107], the relative contributions to the CO_2 product by ethylene and acetic acid remain in dispute. Some three decades ago, Samanos, *et al.* [63], reported no differences in the apparent activation energies measured for ethylene combustion in the presence and absence of AcOH over unpromoted Pd/SiO_2 and Pd/Al_2O_3 catalysts and concluded that CO_2 was formed primarily from ethylene. For unsupported Pd, Pd/Al_2O_3, and alkali-promoted Pd/Al_2O_3 catalysts, Nakamura and Yasui [81] also concluded that CO_2 is produced mainly via oxidation of C_2H_4. More recently in the most comprehensive study of VA synthesis to date, Crathorne, et al. [55], using isotopic transient kinetics and $Pd/Cd/SiO_2/K^+$ and $Pd/Au/SiO_2/K^+$ catalysts, concluded that CO_2 was derived equally from ethylene and acetic acid. In order to gain more insight into this important side reaction in VA synthesis, a kinetic study of ethylene combustion was carried out on Pd particles of varying size supported on high-surface-area SiO_2 (600 m^2/g).

The Pd (5 wt%)/SiO_2 catalyst was used for VA synthesis and CO_2 formation [79] and as shown in Fig. 21, variation of the reaction rates, r_{VA} and r_{CO_2}, with p_{O_2} was determined at 413 K with $p_{C_2H_4}$ fixed at 7.5 kPa and p_{AcOH} held at 2.0 kPa. By increasing p_{O_2} from 1.0 to 8.4 kPa, r_{CO_2} increased by a factor of 7, from 0.13×10^{-4} to 0.9×10^{-4} s^{-1}. Also simultaneously, a 20% increase of r_{VA} from 1.1×10^{-4} to 1.3×10^{-4} s^{-1} was observed. The corresponding selectivity towards CO_2 increased from < 10 % at $p_{O_2} = 1.0$ kPa to nearly 25 % at $p_{O_2} = 8.4$ kPa. Obviously, ethylene combustion is enhanced more than VA synthesis by an increase in p_{O_2}.

The dependence of CO_2 formation rate (r_{CO_2}) on $p_{C_2H_4}$ was measured between 5.0 – 15.0 kPa and 413 – 453 K in the presence and absence of AcOH, while p_{O_2} was held constant at 6.3 kPa. In the presence of AcOH (p_{AcOH} = 2.0 kPa) (see the dashed-line plots of Fig. 22) a small decrease of r_{CO_2} with an increase in $p_{C_2H_4}$ was observed. Also, r_{CO_2} increases significantly with an increase in temperature. Similar behavior of r_{CO_2} versus $p_{C_2H_4}$ was observed both in the absence of AcOH and in the presence of AcOH (see solid line in Fig. 22). At 413 K r_{CO_2} in the absence of AcOH is significantly higher than in the presence of AcOH.

Similarly, in the presence and absence of AcOH the change in r_{CO_2} with p_{O_2} was investigated with the $p_{C_2H_4}$ fixed at 7.5 kPa. In the presence of AA (see the dashed lines in Fig. 23) r_{CO_2} increases steadily with an increase in p_{O_2}. In the absence of AcOH a similar behavior

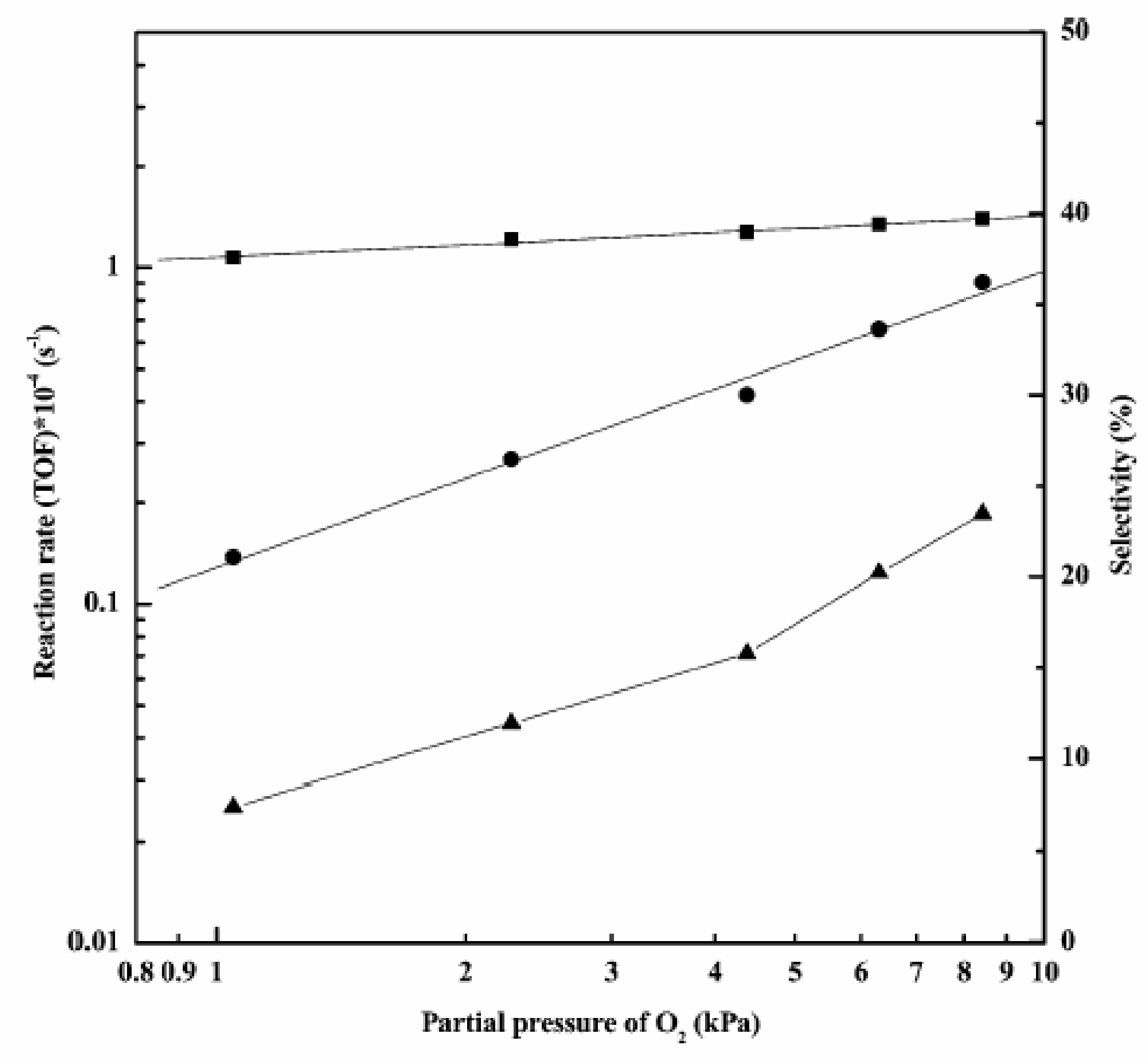

Fig. 21. Variation of reaction rates (VA (■) and CO_2 formation (●)) and selectivity of CO_2 (▲) with the partial pressure of O_2 at 413 K over Pd(5wt%)/SiO_2 catalyst, feed gas: $p_{C_2H_4}$ = 7.5 kPa, p_{O_2} = 1.0-10 kPa, p_{AcOH} = 2.0 kPa, rest N_2; flow rate: 60 ml/min; catalyst weight: 1.6 g.

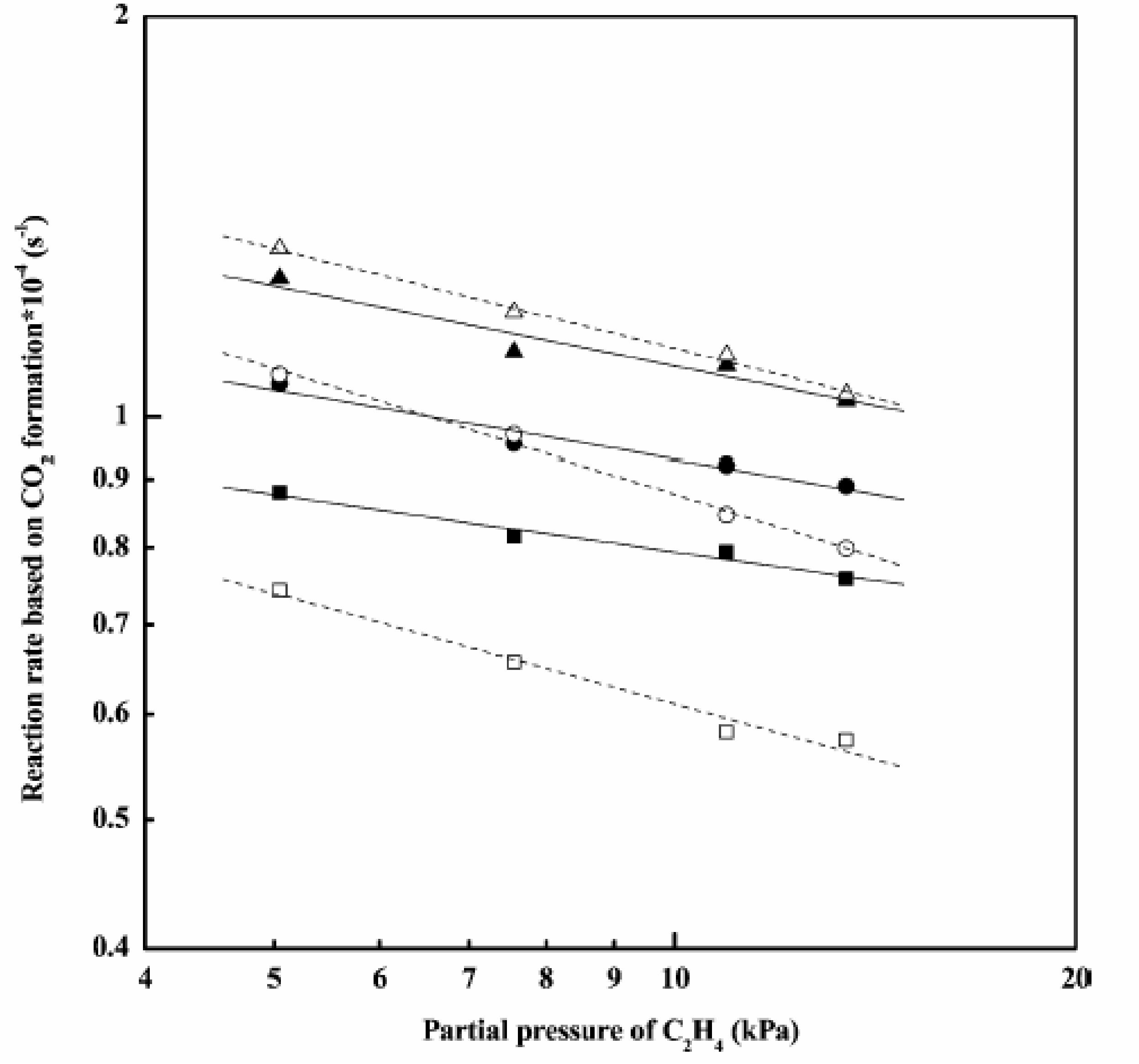

Fig. 22. Dependence of CO_2 formation rate on partial pressure of C_2H_4 in the presence of acetic acid: (□) at 413 K, (○) 433 K and (△) 453 K, feed gas: p_{O_2} = 6.3 kPa, $p_{C_2H_4}$ = 5.0-15.0 kPa, p_{AcOH} = 2.0 kPa, rest N_2, flow rate: 60 ml/min, catalyst weight: 1.6 g; in the absence of acetic acid: (■) at 413 K, (●) at 433 K, (▲) at 453 K, feed gas: p_{O_2} = 6.3 kPa, $p_{C_2H_4}$ = 5.0-15.0 kPa, rest N_2, flow rate: 60 ml/min, catalyst weight: 1.2 g.

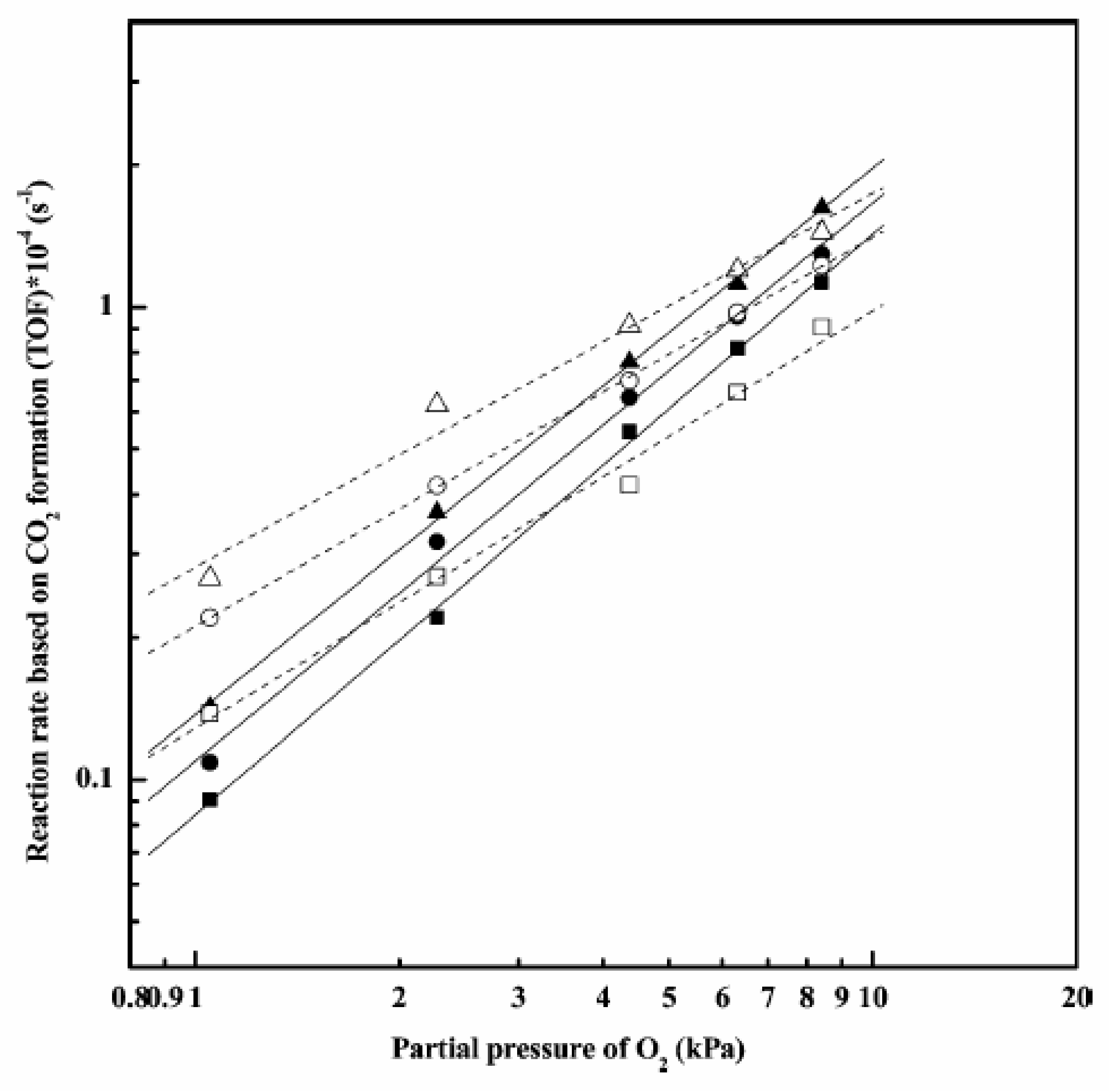

Fig. 23. Dependence of CO_2 formation rate on partial pressure of O_2 in the presence of acetic acid: (□) at 413 K, (○) 433 K and (△) 453 K, feed gas: $p_{C_2H_4} = 7.5$ kPa, $p_{O_2} = 1.0\text{-}10.0$ kPa, $p_{AcOH} = 2.0$ kPa, rest N_2, flow rate: 60 ml/min, catalyst weight: 1.6 g; in the absence of acetic acid: (■) at 413 K, (●) at 433 K, (▲) at 453 K, feed gas: $p_{C_2H_4} = 7.5$ kPa, $p_{O_2} = 1.0\text{-}10.0$ kPa, rest N_2, flow rate: 60 ml/min, catalyst weight: 1.2 g.

of the variation of r_{CO_2} versus p_{O_2} in the absence of AcOH (see the solid line in the Fig. 23) was also observed. It should be observed that r_{CO_2} versus p_{O_2} in the absence of AcOH grows faster than in the presence of AcOH. The reaction orders with respect to ethylene (α) and oxygen (β) were calculated using a power rate law:

$$r_{CO_2} = k \cdot p_{C_2H_4}^{\alpha} \cdot p_{O_2}^{\beta} \tag{31}$$

The results are shown in Table 3. The E_a for ethylene combustion in the absence of AcOH was 17.0 kJ/mol and in the presence of AcOH a value of 21.0 kJ/mol was obtained. Samanos [63] had reported that the presence has significant influence on ethylene combustion during the synthesis of VA. In our studies we did not find any prominent changes in CO_2 formation rate in the presence and absence of AcOH. As shown in Table 3, a negative reaction order with respect to C_2H_4 and a positive order with respect to O_2 indicate that the reaction can be fitted by a Langmuir-Hinshelwood mechanism where the dissociation. The negative order with respect to ethylene and the positive order with respect to oxygen indicate that ethylene or dehydrogenation/decomposition derivatives occupy most of the Pd adsorption sites. Since ethylene adsorption dominates the surface, the dissociative adsorption of oxygen may be suppressed and may become the rate- determining step in ethylene combustion. Ethylene combustion on a supported Pd/SiO_2 catalyst might occur through the mechanism of oxygen-activated combustion proposed by Guo, et al. [109]. In this mechanism an oxygen atom abstracts a hydrogen atom from an ethylene molecule and attacks the C atom of ethylene. Also, the mechanism of indirect combustion, in which the adsorbed oxygen reacts with an adsorbed C and H to form CO_2 and H_2O, cannot be ruled out. However, the contribution of this mechanism is estimated to be only a small fraction of the CO_2 to the overall rate.

Table 3. Kinetic parameters for ethylene combustion in the presence and absence of acetic acid according to the power rate law: $r_{CO_2} = k \cdot p_{C_2H_4}^{a} \cdot p_{O_2}^{\beta}$

Kinetic parameters	Absence of AcOH			Presence of AcOH		
	413 K	433 K	453 K	413 K	433 K	453 K
Rate Constant (k)*10^{-3}/s^{-1}	1. 66	1.66	1.78	0.38	0.42	0.71
α	-0.15 ±0.01	-0.17 ±0.01	-0.19 ±0.02	-0.27 ±0.02	-0.31 ±0.01	-0.27 ±0.01
β	1.22 ±0.01	1.18 ±0.02	1.16 ±0.01	0.88 ±0.03	0.82 ±0.01	0.89 ±0.03
Ea/kJ/mol	17.0±4.0			21.0±4.0		

Palladium Single Crystal Catalysts

VA Reaction Rate Measurements

The present study was undertaken to examine in detail the kinetics of VA formation over a Pd(100) single crystal and to compare the results with data from high-surface-area Pd supported on SiO_2. The single crystal Pd(100) catalyst used in this study was a 1.0 cm diameter, 0.1 cm thick disk. The catalyst was cleaned in UHV using Ar ion sputtering and annealing to 1000 K. A typical reaction time was 2 hours at a total pressure of ~15 Torr. After reaction, the products were condensed in a sample loop and introduced into the GC for analysis. The reactor was then evacuated and the catalyst transferred into the surface analysis section for XPS analysis. The turnover frequencies (TOF's) (molecules of VA produced per surface Pd site per second) were calculated from the number of VA molecules produced during the reaction (total conversion <0.5 %) using a Pd(100) atom density of 1.7×10^{15} atoms/cm^2.

Fig. 13 shows the temperature dependent reaction rates for VA synthesis on Pd-only catalysts. The reaction rate over the Pd(1 wt%)/SiO_2 is higher than that for Pd(5 wt%)/SiO_2 [78]. On Pd(100) VA formation rate was observed to be even lower confirming the fact that larger particles are relatively less active for VA formation [84]. Using Pd(100), the corresponding E_a was determined to be 23.0 kJ/mol. Reliable selectivity data could not be obtained for Pd(100) catalyst since the amount of CO_2 produced is very small compared to that of the background. Using a Pd(100) catalyst, the reaction rates as a function of oxygen and ethylene partial pressure at 433 K are displayed in Figs. 24 and 25, respectively. As evident in Fig. 24, changing p_{O_2} from 2.0 to 6.0 Torr while maintaining $p_{C_2H_4}$ and p_{AcOH} constant at 9.0 and 4.0 Torr, respectively, the

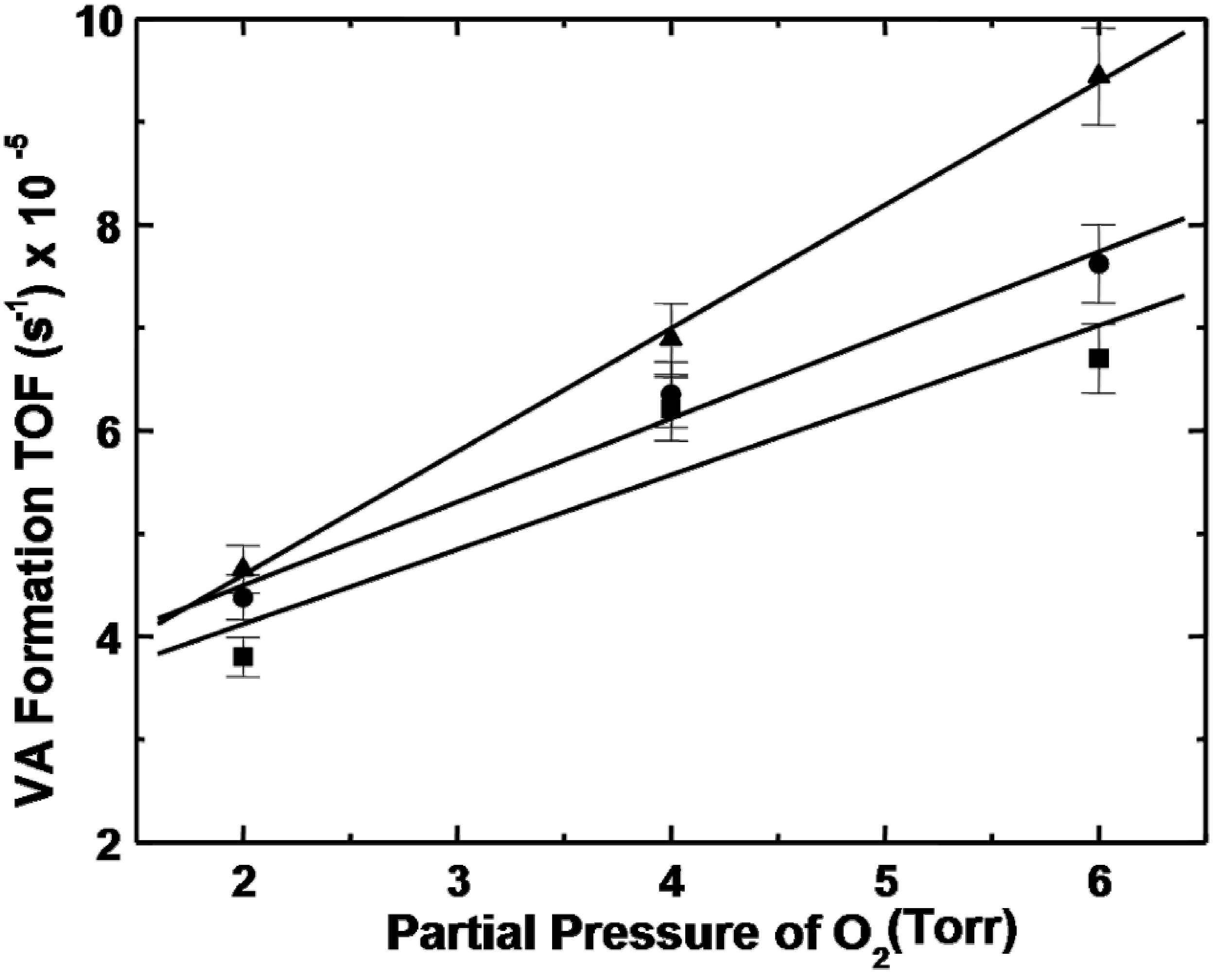

Fig. 24. Dependence of VA formation TOF on partial pressure of O_2 at 413 K (■), 423 K(●), 433 K (▲) on Pd(100); $p_{C_2H_4} = 9.0$ Torr, $p_{AcOH} = 4.0$ Torr.

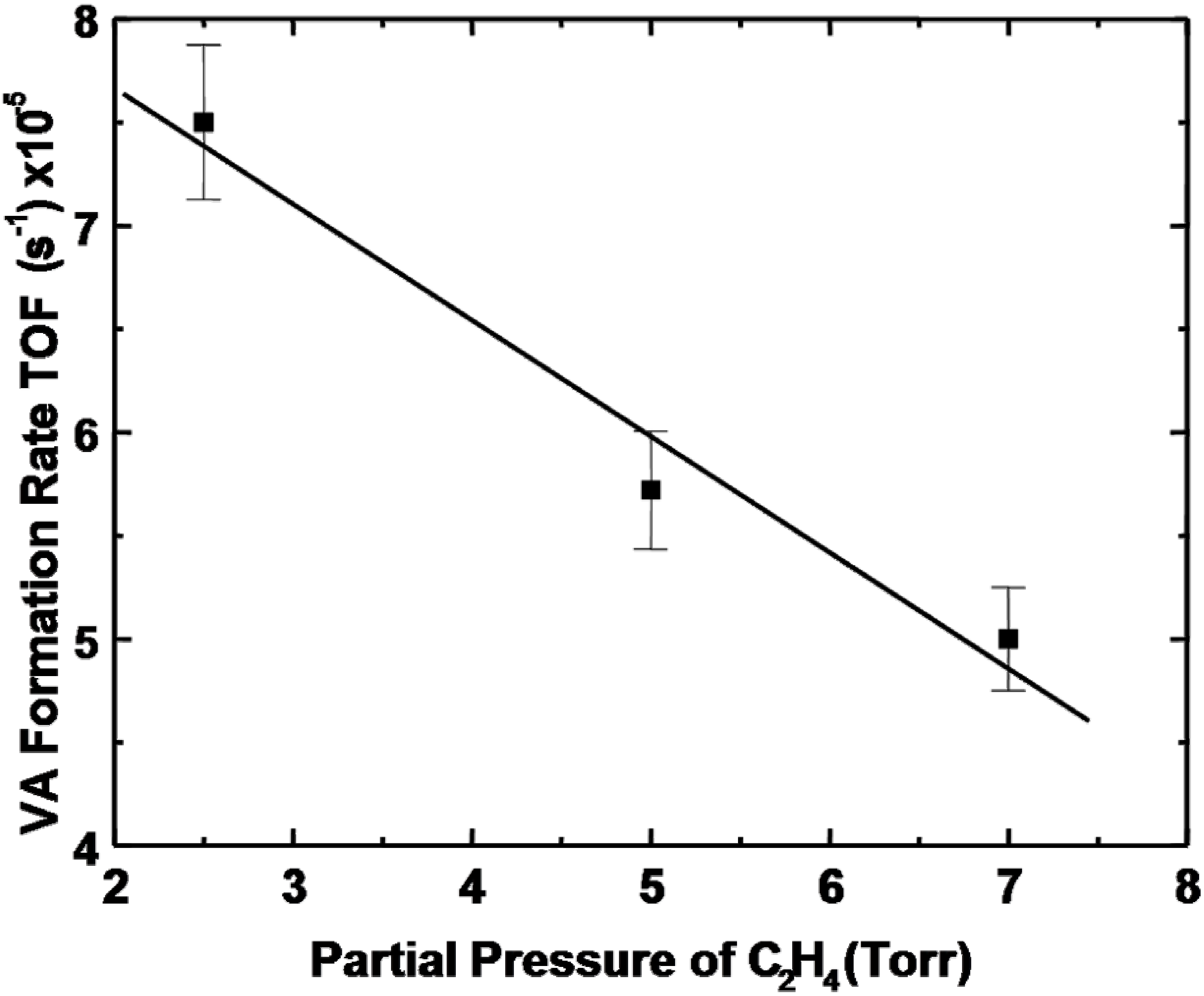

Fig. 25. Dependence of VA formation rate on partial pressure of C_2H_4 at 433 K (■) on Pd(100); $p_{O_2} = 2.0$ Torr, $p_{AcOH} = 4.0$ Torr.

reaction rate increased from 4.5×10^{-5} to 7.5×10^{-5} s^{-1} at 423 K. Similarly, by changing $p_{C_2H_4}$ from 2.0 to 7.0 Torr (see Fig. 25) and maintaining p_{O_2} and p_{AcOH} constant at 8.5 Torr and 3.2 Torr, respectively, the reaction rate decreased from 7.5×10^{-5} to 5.0×10^{-5} s^{-1} at 433 K. The reaction orders with respect to C_2H_4 and O_2 were calculated by fitting to a power rate law as follows:

$$r_{VA} = k \cdot p_{C_2H_4}^{a} \cdot p_{O_2}^{\beta} \tag{30}$$

As listed in Table 2, similar negative orders with respect to C_2H_4 and positive order with respect to O_2 have been obtained for all the catalysts studied. These results are in agreement with the results reported for a Pd(2.0 wt%)/SiO_2 catalyst [63]. In summary, the kinetic parameters for VA synthesis over Pd(100) are similar to those observed for supported Pd/SiO_2.

Catalyst Deactivation

The Pd(100) catalyst was observed to maintain a steady activity after initial induction period within the first 20 mins (see Fig. 17). Deactivation was observed to be very slow and was mainly attributed to the formation of carbon on the surface. While, the reactivity of ca. 33% for Pd(1.0 wt%)/SiO_2 and 50% for Pd(5.0 wt%)/SiO_2 was lost in comparison to their maximum rates, using Pd(100) 60% loss in the activity was recorded (see Table 2).

Formation of Pd Carbide and Surface Carbon

Under reaction conditions, acetic acid and water are the primary surface species during VA synthesis as determined by isotopic transient methods [55]. C 1s XPS of the Pd(100) catalyst subsequent to VA reaction (Fig. 13) can be resolved into three distinct peaks with binding energies (BE) centered at 284.2, 285.5 and 288.0 eV [84]. The more intense peak at

284.2 eV is assigned to a surface CH_x (x = 0-3) species formed from the dissociation of an ethylene and/or acetate species. The features at 285.5 and 288.0 eV are assigned to CO and an acetate species, respectively [110-113].

Adsorption of CO at saturated coverage was used to calibrate the amount of surface carbon on Pd(100) after reaction. The C_{1s} XP spectra show a primary feature centered at 285.5 eV for various coverages of CO (as shown in the lower panel of Fig. 26), which is in excellent agreement with the observations by Jones et al. [114,115]. Madix, et al. [116], have reported that the saturation coverage for CO on Pd(100) at room temperature is 0.53 ML. By comparing the peak area of the C_{1s} region after VA reaction (Fig. 26 upper panel) to that for saturated CO shown in Fig. 26 lower panel, the amount of C on Pd(100) after reaction is estimated to be approximately 1.5 ML. This carbon coverage is in agreement with the results of Bowker, et al., who have estimated the carbon coverage on Pd(110) following exposure to ethylene [110] and acetic acid [117] to be approximately 1.5 ML. These authors report that of this 1.5 ML, 0.5 ML is on the topmost surface while the remainder is interdiffused into the top several layers of the catalyst.

Fig. 27 A shows C_{1s} XPS spectra acquired at room temperature after reaction and after flashing the Pd(100) catalyst to various temperatures. Each of these spectra can be deconvoluted into three surface species, CH_x, CO and acetate, as shown in Fig. 26. The intensities for each component as a function of annealing temperature were plotted in Fig. 27 B. After a flash to 380 K the intensities of the carbon features at 284.3 and 288.5 eV decrease rapidly. This reduction in intensity is likely due to desorption of ethylene and acetate species, in agreement with previous studies [117,118], showing desorption of acetate species at approximately 350 K. Flashing to much higher temperatures, i.e. >500 K, removes adsorbed CO (at 285.5 eV), and at still higher

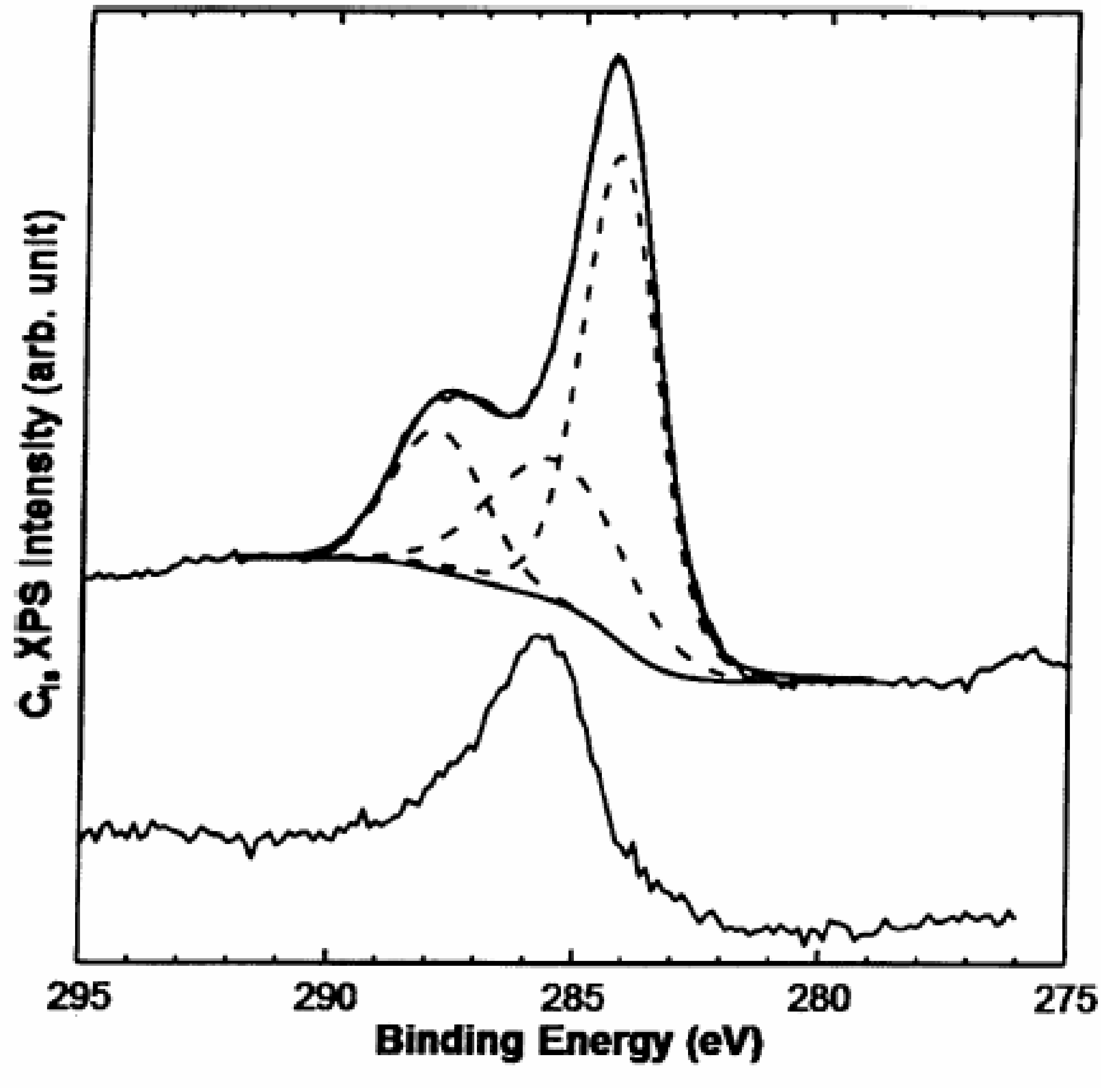

Fig. 26. Upper panel is the C_{1s} XPS spectrum after VA reaction on Pd(100) at 433 K; p_{O_2} = 2.0 Torr, $p_{C_2H_4}$ = 9.0 Torr, p_{AcOH} = 4.0 Torr; Lower panel is the C_{1s} XPS spectrum of saturated coverage of CO on Pd(100) at 300 K.

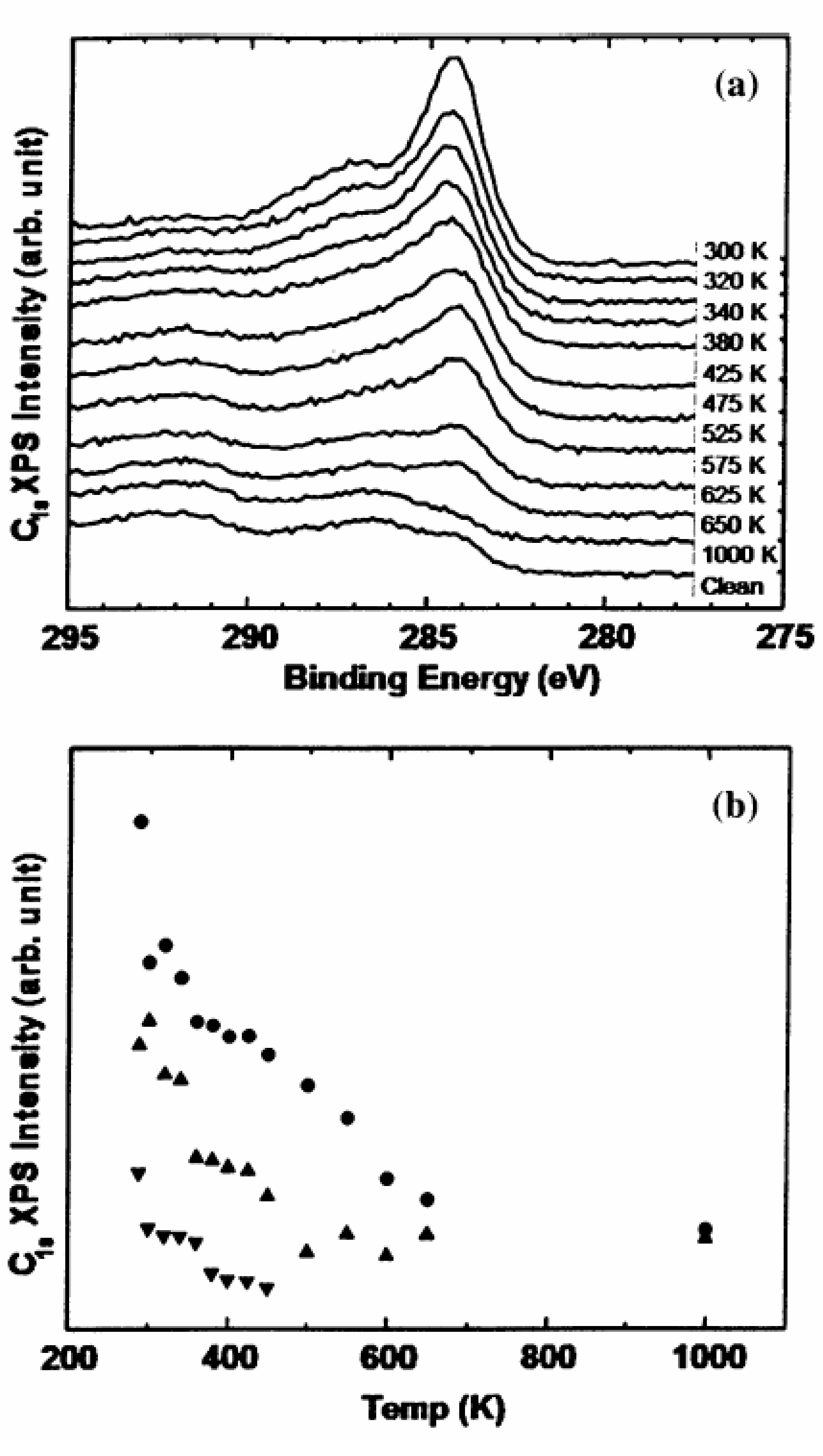

Fig. 27. (A) C_{1s} XPS spectra on Pd(100) after reaction at 433 K and after annealing to temperatures as indicated; $p_{O_2} = 2.0$ Torr, $p_{C_2H_4} = 9.0$ Torr, $p_{AcOH} = 4.0$ Torr; (B) C_{1s} XPS peak intensity for CH_x (●), CO (▲) and acetate (▼) species plotted against the annealing temperature.

temperatures, the feature at 284.2 eV, assigned to amorphous carbon and CH_x species, disappears. Note that during this transformation no apparent change was observed in the binding energy of the Pd 3d feature. These XPS results show that carbon-containing species formed during VA synthesis reaction are stable on Pd(100) to 350 – 500 K.

Ethylene Combustion Kinetics

Previous studies have confirmed that ethylene combustion is the primary side reaction in the synthesis of VA on Pd-based catalysts [55,60,63,78,79,81]. Reducing ethylene combustion during VA synthesis is crucial for optimizing the efficiency of this important industrial reaction. In order to gain more insight into this important side reaction in VA synthesis, a kinetic study of ethylene combustion was carried out on a Pd(100) single crystal. For comparative purposes, parallel studies were carried out on Pd particles of varying size supported on high-surface-area SiO_2 (600 m^2/g).

Fig. 28 shows the relationship of the CO_2 formation rate on Pd(100) versus the partial pressure of O_2 (p_{O_2}) at various temperatures [119]. The TOF's increase with an increase in p_{O_2} up to ~ 7 Torr, then decrease at every temperature. It is noteworthy that all experiments were carried out with the same total pressure (15 Torr) changing only the O_2/C_2H_4 ratio. At fixed p_{O_2} (7 Torr) only minor effects were detected when varying $p_{C_2H_4}$ within a relatively small range (4 – 13 Torr), consistent with a saturation coverage of C_2H_4 on the Pd(100) surface during reaction. The corresponding p_{O_2} for the maximum TOF's shifts gradually to a high value of $p_{O_2} / p_{C_2H_4}$ as the temperature increases, suggesting an oxygen-limited reaction. Interestingly, increasing $p_{O_2} / p_{C_2H_4}$ after reaching the maximum leads to a flat, constant reaction rate at 428,

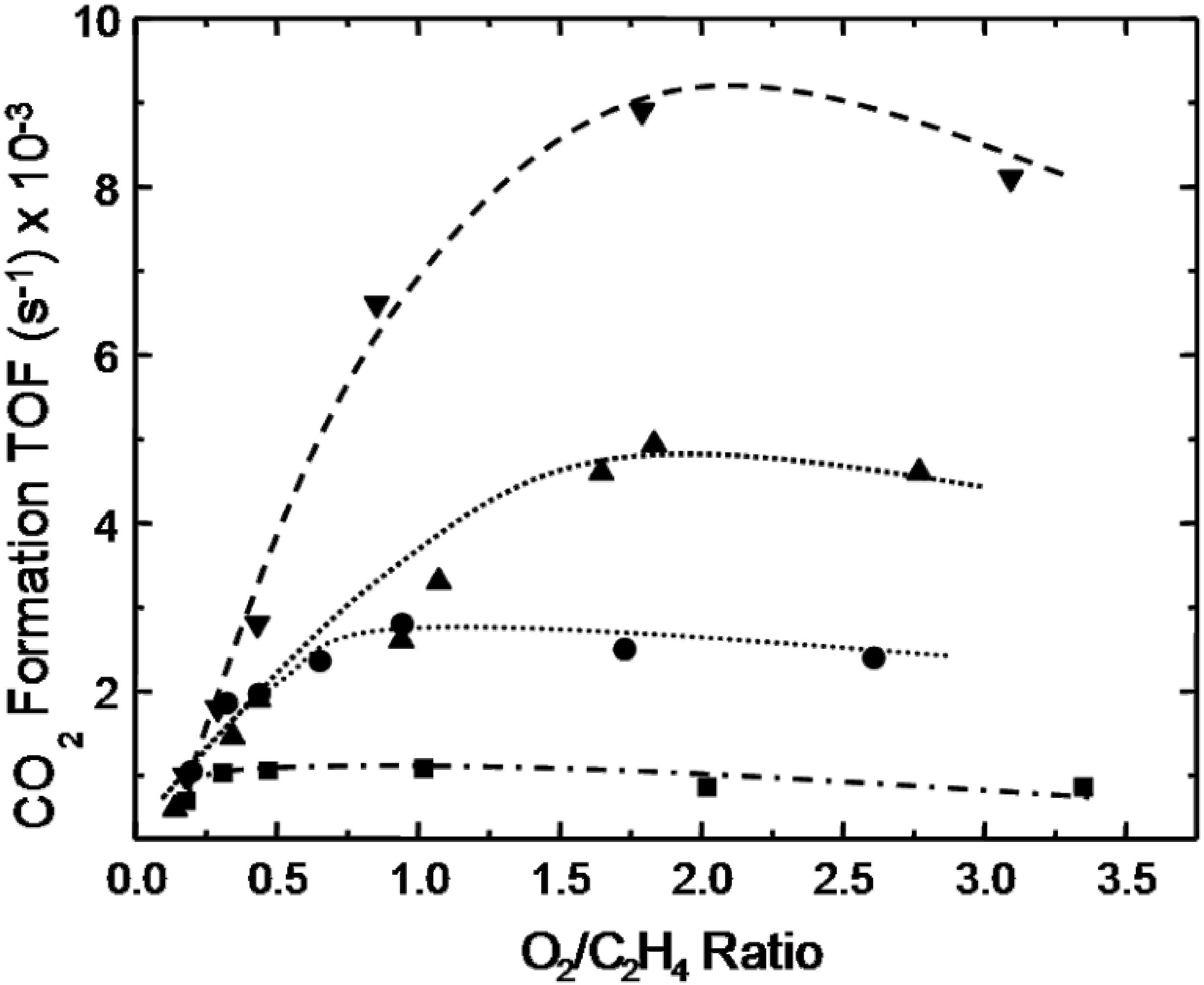

Fig. 28. Reaction rate as a function of O_2:C_2H_4 ratio at various temperatures on Pd(100); total pressure = 15.0 Torr; 428 K (■), 443 K (●), 458 K (▲), 473 (▼).

443 and 458K. A rollover, however, is observed at 473 K indicating the presence of two kinetic regimes: one corresponding to low $p_{O_2} / p_{C_2H_4}$ values and another corresponding to high $p_{O_2} / p_{C_2H_4}$. These kinetic data of Fig. 28 are consistent with a Langmuir-Hinshelwood mechanism for ethylene combustion on Pd(100).

As shown in Figs. 29 and 30 on Pd(5 wt%)/SiO_2 and Pd(1 wt%)/SiO_2 the specific TOF's were measured, respectively, after ~ 2.5 hrs of reaction time at various temperatures and reactant gas ratios. Analogous behavior is seen for supported Pd and the Pd(100) catalysts. As discussed above, competitive adsorption of oxygen and ethylene is observed for supported Pd catalysts, therefore, it is inferred that a similar reaction mechanism can be invoked for Pd(100) and supported Pd catalysts.

For comparison, Fig. 31 shows the $p_{O_2} / p_{C_2H_4}$-dependent reaction rates for all catalysts at 453 K. The rates for different catalysts are in the order of Pd(1 wt%)/SiO_2 > Pd(5 wt%)/SiO_2 ≈ Pd(100). It should be recollected that, by TEM the Pd particle size was estimated to be 2.5 nm for Pd(1 wt%)/SiO_2 catalyst and 4.2 nm for Pd(5 wt%)/SiO_2 catalyst. The activity of CO_2 formation on Pd(100), therefore follows more closely that of the larger particle Pd(5 wt%)/SiO_2 catalyst.

On Pd single crystals and clusters, it has been shown that ethylene adsorbs in two possible configurations: (a) π-bonded due to atop adsorption and (b) di σ-bonded due to bridge adsorption [120-122]. Freund and coworkers demonstrated that di σ-bonded ethylene molecules preferentially adsorb on larger particles on Pd/Al_2O_3/NiAl (110) catalysts [123]. It has been shown that with increasing particle size the ability of donation of electrons into π*-orbital of ethylene increases. This implies that the hybridization changes from sp^2 to sp^3, that is, from a π- to a di σ-bonded state. Thus, the adsorption of ethylene is dependent on the particle size due to the change in electronic structure and morphology. The superiority of Pd(1 wt%)/SiO_2 catalyst is due to the morphology and electronic structure of metal particles with a size less than 3 nm.

Fig. 32 shows that the apparent activation energies (E_a) for ethylene combustion are dependent on the ratio of $p_{O_2} / p_{C_2H_4}$ [119]. In oxygen-poor conditions ($p_{O_2} / p_{C_2H_4} < 1.00$) the activation energy is about 35 to 40 kJ/mole for Pd (100); however, the value increases with an increase of p_{O_2}, with an E_a of 65 – 70 kJ/mole observed in oxygen-rich conditions ($p_{O_2} / p_{C_2H_4} > 1.00$). Similar behavior has been observed for Pd(1 wt%)/SiO_2 and Pd(5 wt%)/SiO_2 catalysts as presented in Fig. 32. An E_a increase of Δ17 kJ/mole and Δ47 kJ/mole was observed for Pd(1 wt%)/SiO_2 and Pd(5 wt%)/SiO_2 catalysts, respectively, as the $p_{O_2} / p_{C_2H_4}$ was changed from 0.5 to 3.5. E_a's are in the order Pd(100) > Pd(5 wt%)/SiO_2 and Pd(1 wt%)/SiO_2 for a given $p_{O_2} / p_{C_2H_4}$.

XPS has been used to investigate carbon deposition on Pd(100) surface before and after the reaction. The ratio of C 1s / Pd $3d_{3/2}$ XPS intensity was used as an indication of carbon accumulation on Pd(100). As anticipated, more carbon is observed on the surface in oxygen poor conditions (see Figs. 33 A and B). A transition zone where carbon is deposited on the surface is observed for a $p_{O_2} / p_{C_2H_4}$ range between 1.00 and 1.50, and then decreases with further increase in $p_{O_2} / p_{C_2H_4}$. This observation seems consistent with the fact that carbon can be removed by excess oxygen on the surface.

Fig. 34 is a comparison between C 1s XPS intensity on Pd(100) after reaction versus the saturated amount of CO dosed onto Pd(100) surface at room temperature. Since saturation carbon coverage is 0.53 ML, the amount of carbon on Pd(100) after reaction in low O_2 to C_2H_4 ratios is about 1.7 ML. This value decreases to less than 1.0 ML at higher reactant ratios. From

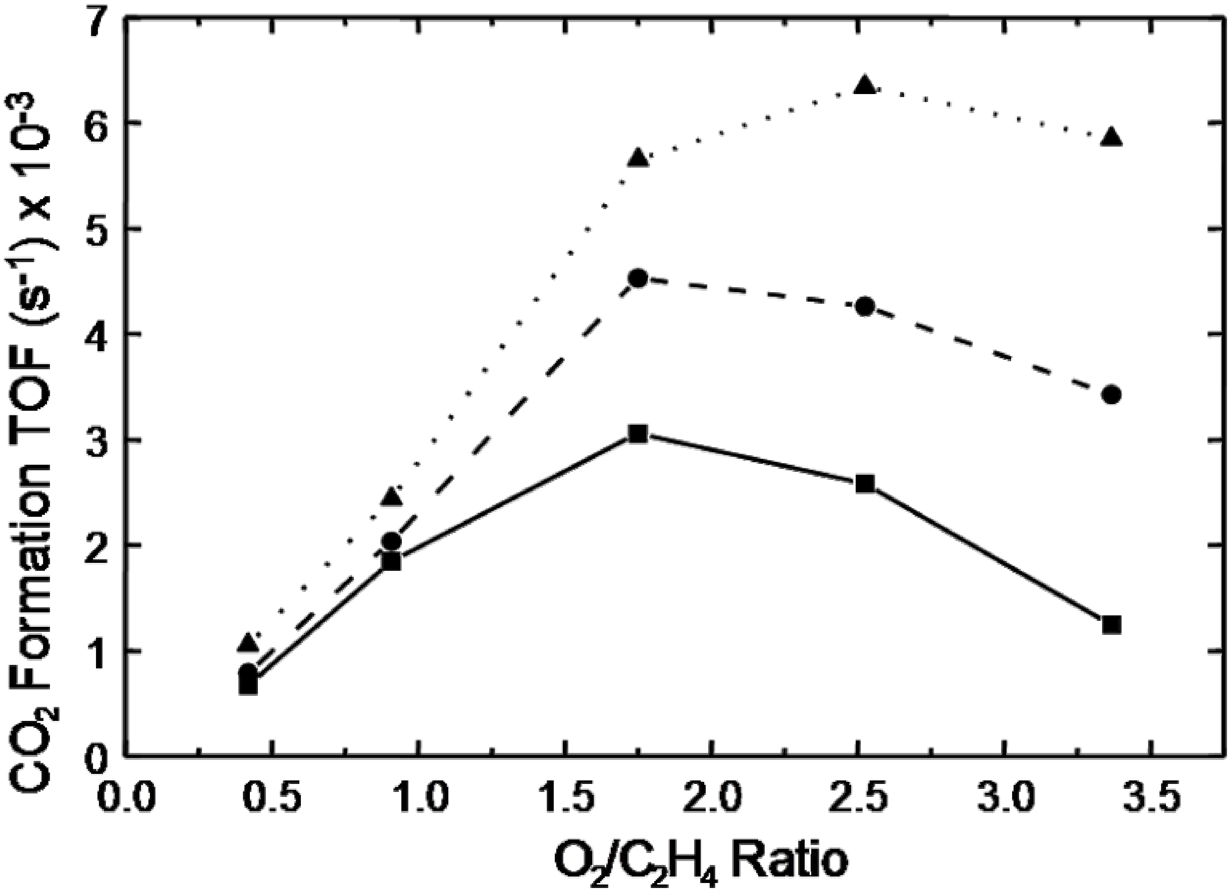

Fig. 29. Reaction rate as a function of O_2:C_2H_4 ratio at various temperatures on Pd(5 wt%)/SiO_2. Total pressure of C_2H_4 and O_2 = 131 Torr; remainder N_2. Flow rate: 60 ml/min, catalyst weight: 1.2 g; 433 K (■), 453 K (●), 473 K (▲).

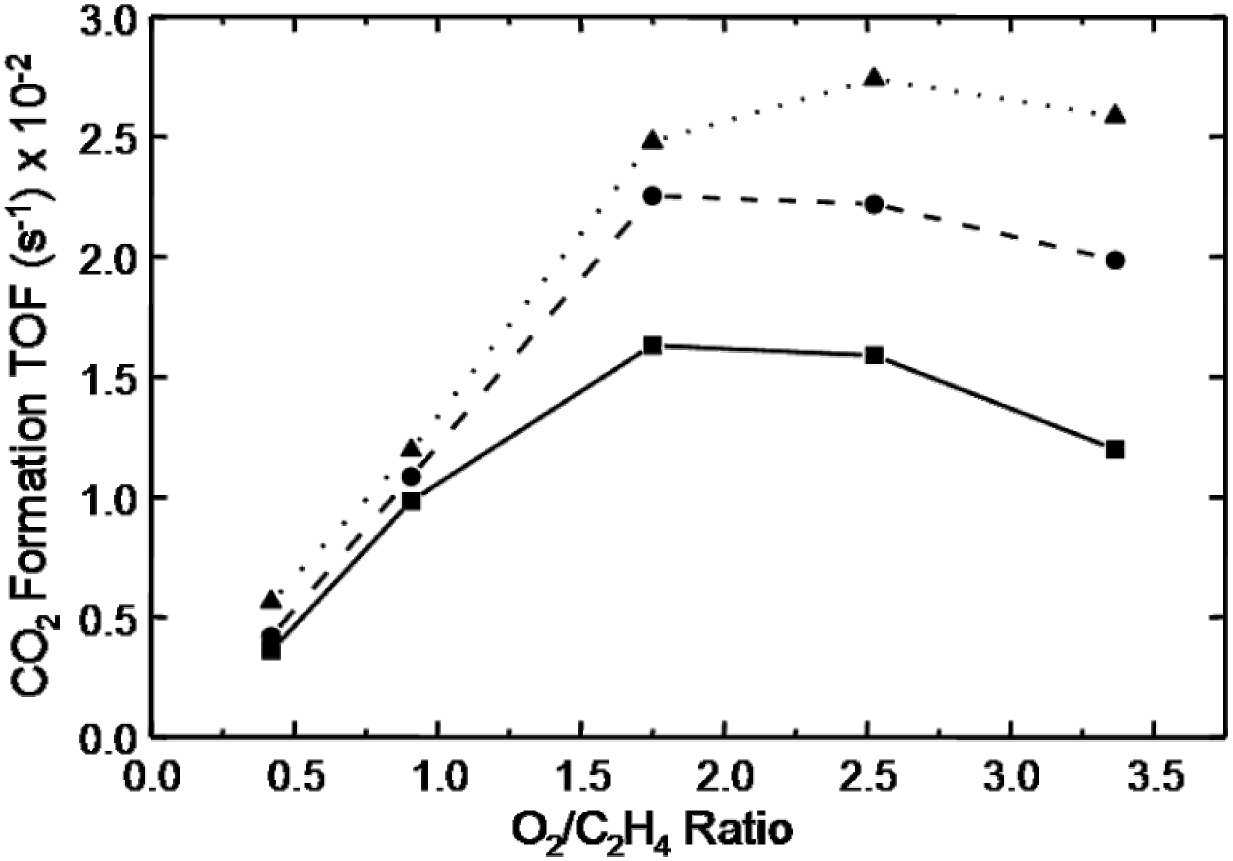

Fig. 30. Reaction rate as a function of O_2:C_2H_4 ratio at various temperatures on Pd(1 wt%)/SiO_2. Total pressure of C_2H_4 and O_2 = 131 Torr; remainder N_2; flow rate: 60 ml/min, catalyst weight: 2.0 g. 433 K (■), 453 K (●), 473 K (▲).

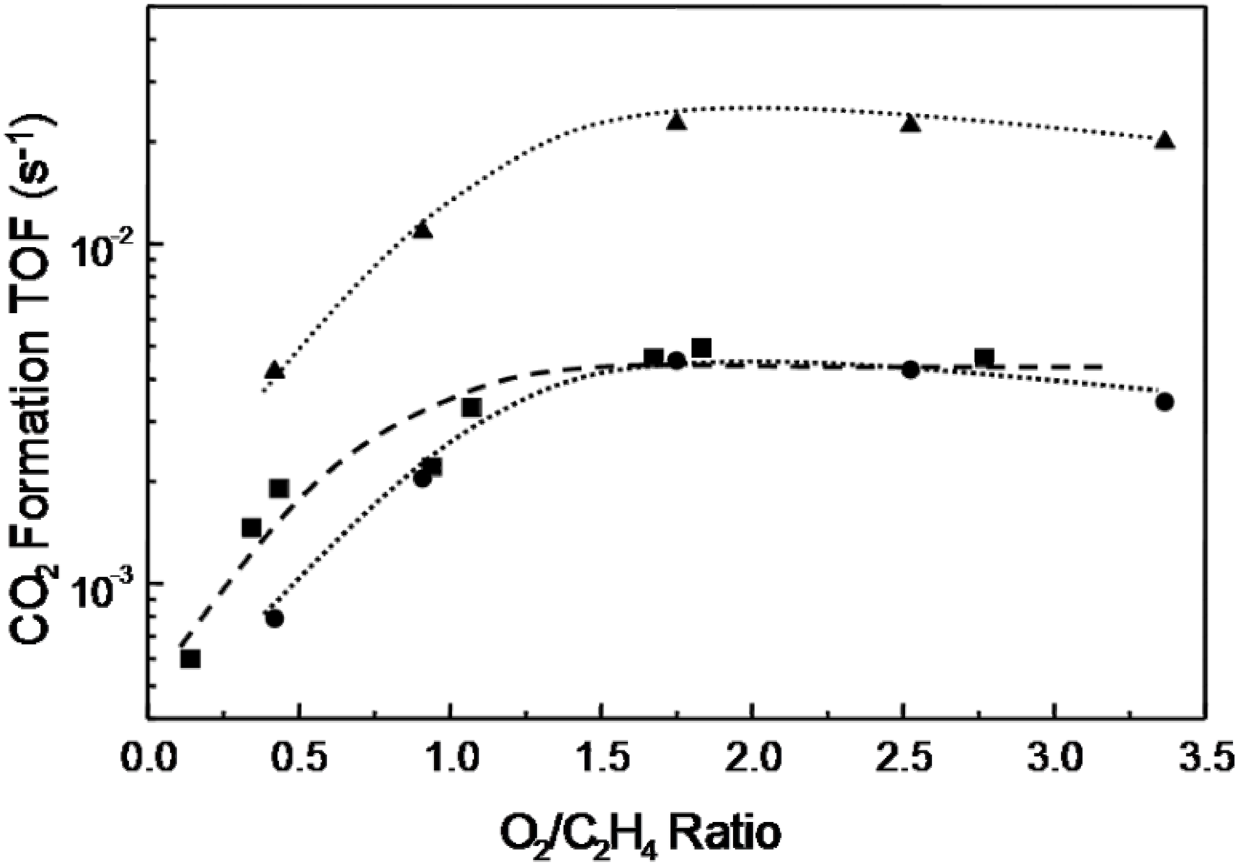

Fig. 31. Comparison of the reaction rates for Pd(100), Pd(1 wt%)/SiO_2, and Pd(5 wt%)/SiO_2 catalysts. Pd(1 wt%)/SiO_2 (▲) and Pd(5 wt%)/SiO_2 (●) at 453 K and Pd(100) (■) at 458 K.

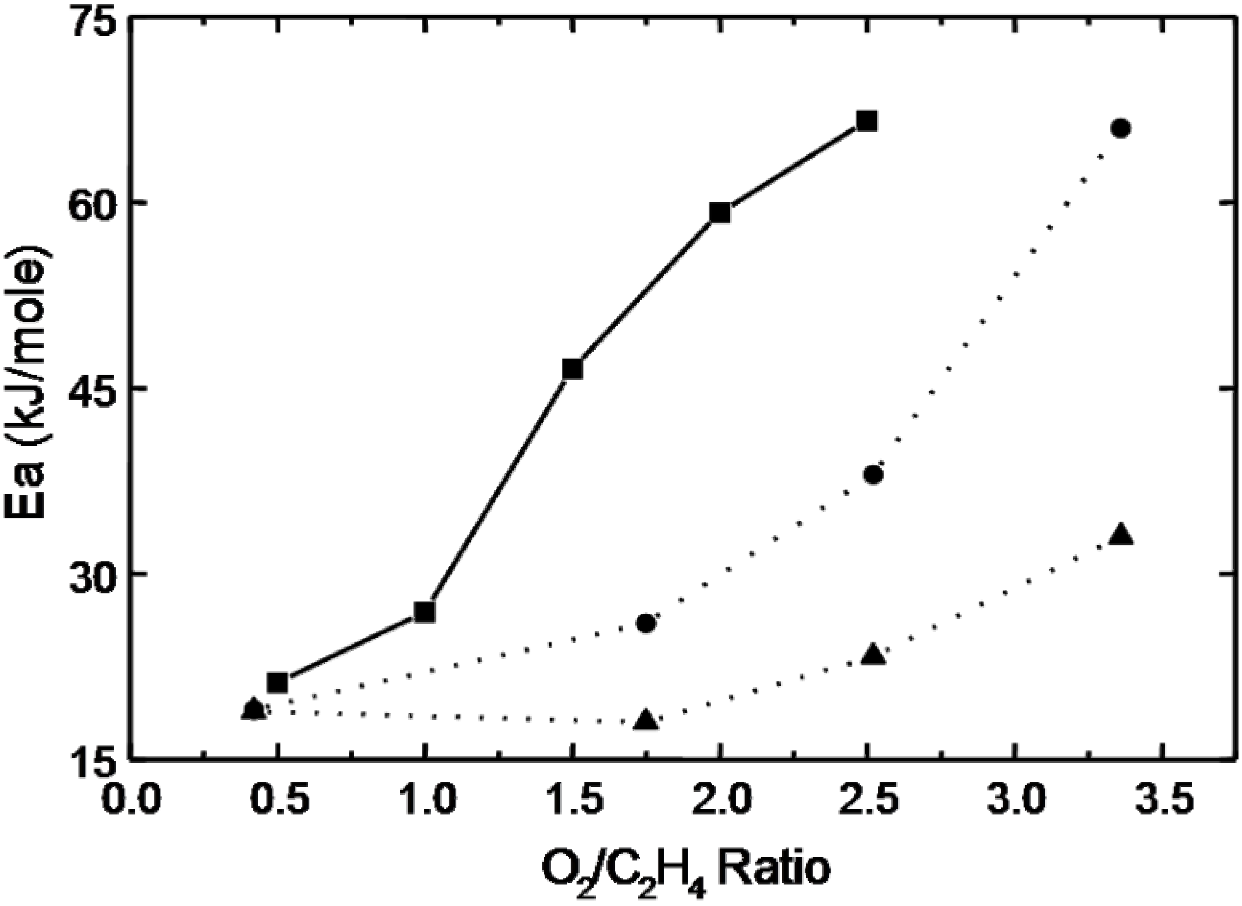

Fig. 32. Apparent activation energies as a function of the O_2:C_2H_4 ratio. Pd(1 wt%)/SiO_2 (▲), Pd(5 wt%)/SiO_2 (●) and Pd(100) (■).

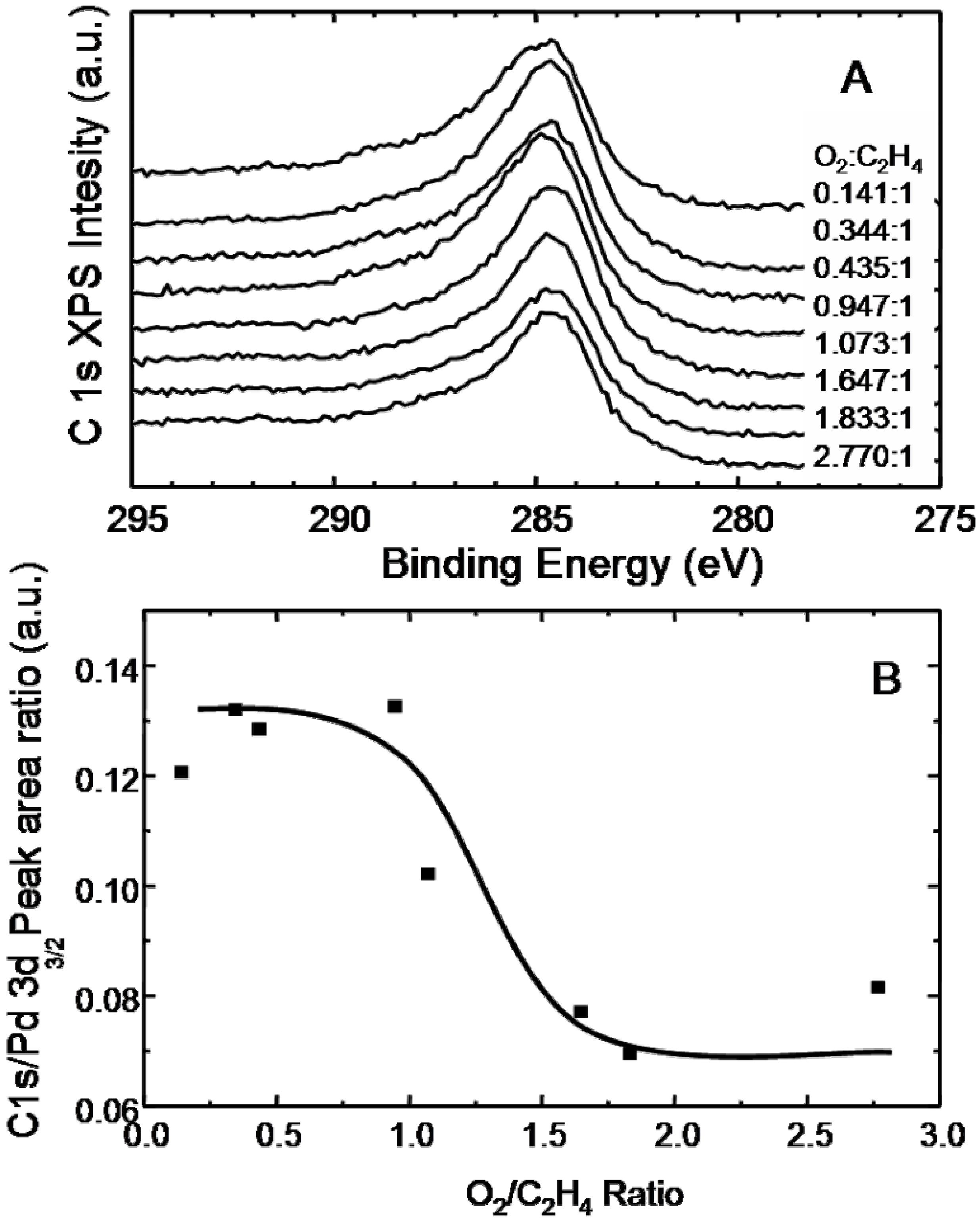

Fig. 33. (A) C 1s XPS spectra at various O_2/C_2H_4 ratios on Pd(100) at 458 K. (B) C 1s/Pd 3d5/2 peak intensity as a function of the O_2:C_2H_4 ratio at 458 K on Pd(100) catalyst.

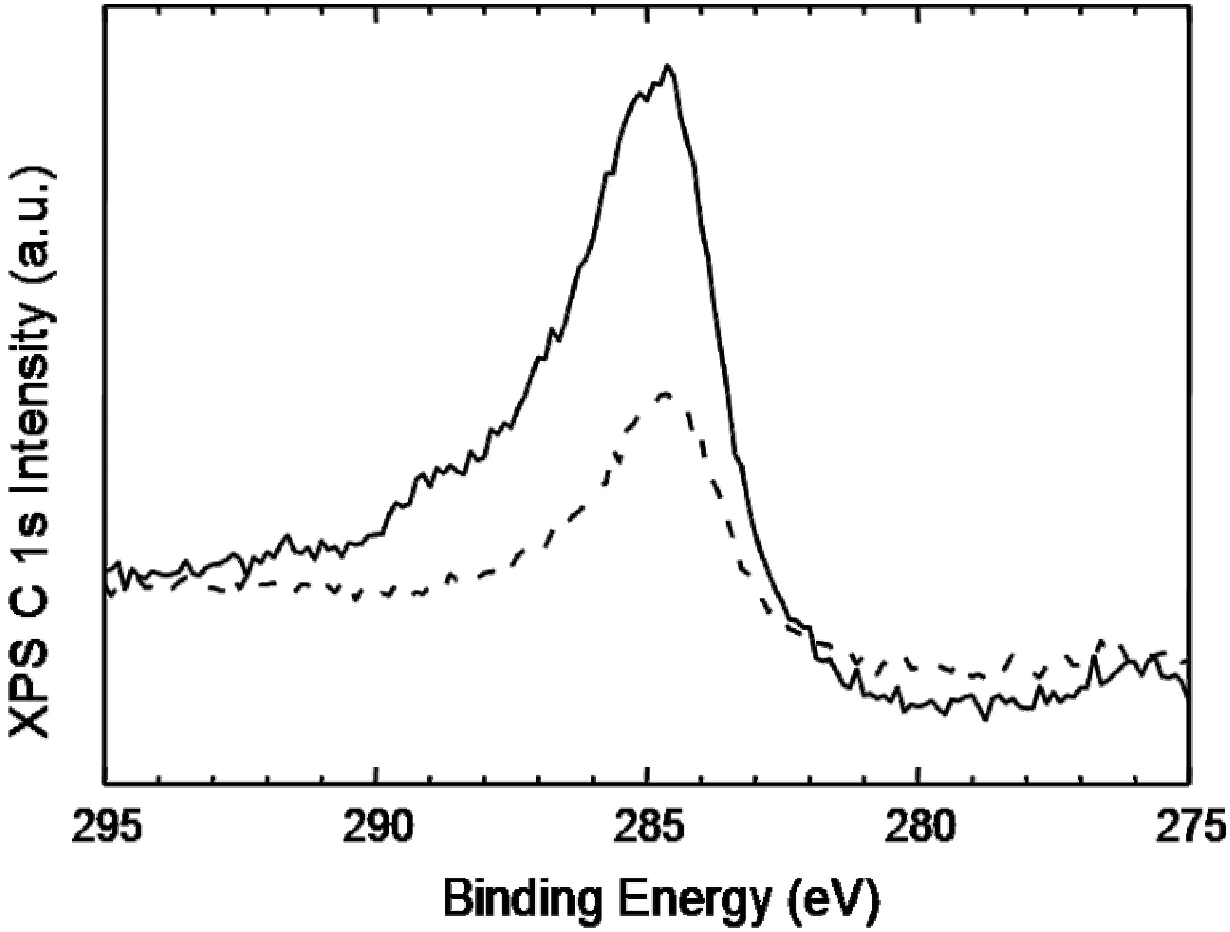

Fig. 34. Comparison of C 1s XPS signal on Pd(100) after reaction at 458 K, O_2:C_2H_4 = 0.94:1.0; total pressure = 15.0 Torr and C 1s XPS signal on Pd(100) after CO saturation at room temperature. Saturation coverage of CO (solid line), carbon region after reaction (dashed line).

Fig. 28 it is evident that the maximum formation rate is achieved at reactant ratios (O_2/C_2H_4) higher than 2.0 and at 1.0 ML of carbon.

Palladium Alloy Catalysts

Supported Pd-Au Catalysts

One of the initial studies aimed at understanding the role of Au in enhancing the VA reaction rate has been reported by Provine *et. al.* [69]. While noting that there is indeed an increase in the production rate of VA due to alloying, it was observed that the adsorption strength of some surface species also changed. Among other observations it was noted that Au suppressed the formation of CO from the combustion of acetic acid. It is worth mentioning that the production rate of VA was enhanced due to the change in the desorption rate of the product which was a little faster under the influence of Au. While corroborating the same, Lambert et al. further proposed that under the influence of Au the decomposition of VA is suppressed [68]. Addition of Au was also supposed to enhance the formation of adsorbed monodentate acetate species at 1735 cm^{-1}. This species was proposed to be the key reaction intermediate and the presence of this species under reaction conditions on working Pd catalyst was confirmed by Augustine and Blitz [83].

The commercial VA synthesis catalyst, Pd-Au-K/SiO_2, contains approximately 1 wt% Au and Pd with a 4:1 Pd:Au atomic ratio, and 2.5 wt % of potassium acetate [68,80]. During the lifetime of a commercial Pd-Au-K/SiO_2 catalyst, progressive loss of activity occurs, restricting the useful lifetime. Detail XRD and HREM/EDX investigations [68] show that fresh catalysts contain Pd in two forms: Pd-Au alloy particles 4 - 5 nm in diameter with a Pd:Au ratio of 2:3 and a very highly dispersed Pd metal component corresponding to ~ 85% of the total Pd loading. As a consequence, the alloy particles are far more Au rich (60 atomic % Au) than expected from the metal loadings (~ 20% Au). After aging (deactivation), pronounced sintering of the Pd-Au alloy particles and the appearance of Pd acetate were observed, but without significant change in composition of the alloy particles. It was found that high reaction temperatures as well as high oxygen partial pressures favor deactivation while both the ethylene concentration and initial GHSV influenced very little the deactivation rate [124].

TEM and XRD of Fresh Catalysts

Similar to the preparation of Pd(1 wt%)/SiO_2 and Pd(5 wt%)/SiO_2 catalysts, the Pd(1.0wt%)-Au(0.5wt%)-K+(2.5wt%)/SiO_2 catalyst was prepared by incipient wet-impregnation method. The TEM results of Fig. 35 show that the sizes of the Pd-Au particles are distributed broadly over the range 1.0 – 13.0 nm while most of the particles lie between 2.0 and 5.0 nm. The corresponding average diameter is 3.2 nm for the Pd-Au before reaction. Surface composition determined by EDS indicates that the average Pd/Au atom ratio in region A in Fig. 35 (top) is 2.0, lower than the initially deposited ratio of 4.0; a ratio of 2.2 and 1.9 was observed for particle B and C, respectively. For supported Pd-Au catalysts using XRD after reduction (see Fig. 36 A) a reflection feature is apparent at 39.8°, which is lower than that for the Pd <111> phase by 0.4°. Another peak was observed at 38.6° which corresponds to a Au-rich phase.

VA Reaction Rate Measurements

Fig. 37 shows the formation of VA as a function of partial pressure of oxygen (p_{O_2}) and ethylene ($p_{C_2H_4}$) in the temperature range 393 - 433 K. As illustrated in Fig. 37 A, an increase in

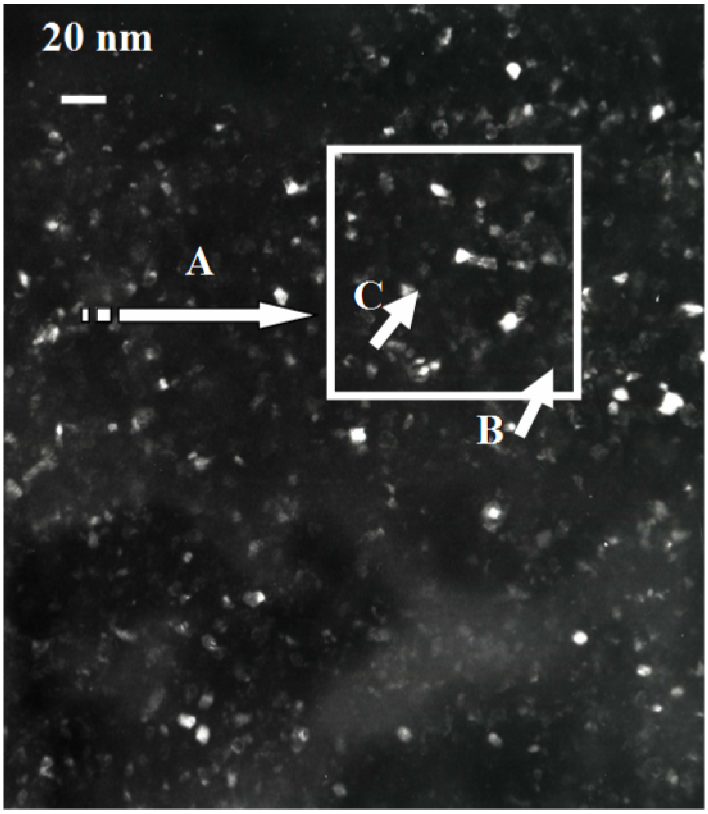

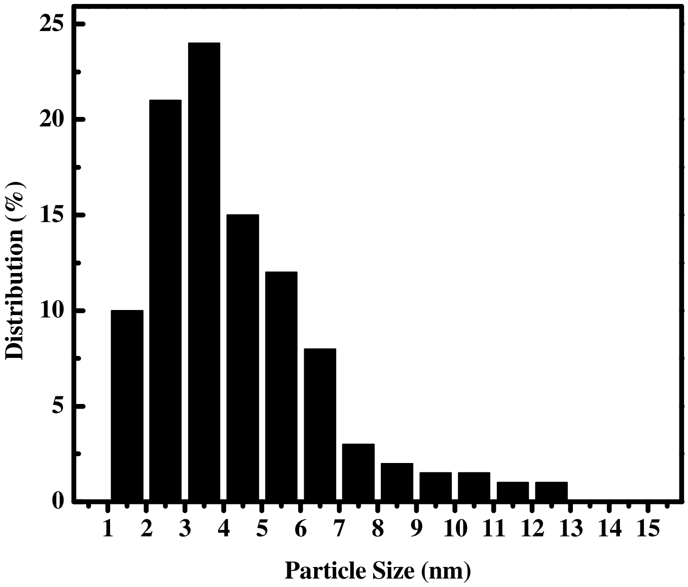

Fig. 35. TEM image of Pd-Au clusters for the reduced Pd-Au catalyst, atomic ratio of Pd/Au in region A = 2/1, at particle B = 2.2/1 and C = 1.9/1. The Pd-Au cluster size distribution is shown in the bottom panel.

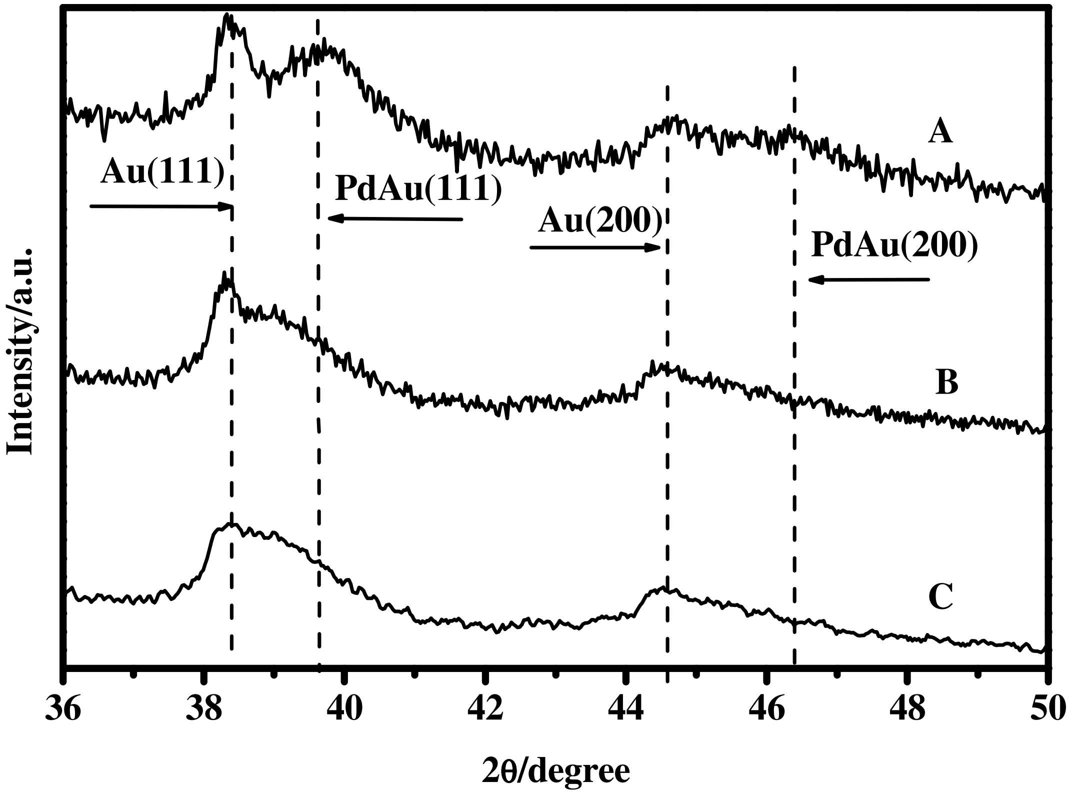

Fig. 36. XRD pattern of Pd-Au/SiO_2 catalysts. A: reduced; B: reacted; C: reacted with H_2 treatment at 623 K for 4 hours.

$p_{C_2H_4}$ maintaining p_{O_2} constant at 1.0 kPa causes the reaction rate to increase. The VA formation rate increased by a factor of two with an increase in the temperature from 393 to 413 K, whereas, only a 25% increase was noted with an increase from 413 to 433 K. The selectivity also varies with temperature and shows the same trend with varying $p_{C_2H_4}$, as shown in Fig. 37B. At 393 K, the selectivity increases from 93.0 to 96.0% by increasing $p_{C_2H_4}$ from 5.0 to 14.0 kPa. In the mean time, as expected the selectivity was decreased with an increase in the temperature. For example, at $p_{C_2H_4}$ = 5.0 kPa, the selectivity fell from 93.0 to 88.0% by changing the temperature from 393 to 433 K. It is proposed that, ethylene combustion increases with an increase in the temperature and leads to the loss of selectivity.

Similarly, the VA formation rate as function of p_{O_2} was measured by maintaining $p_{C_2H_4}$ at 7.5 kPa (see Fig. 37 C) and p_{AcOH} at 2.0 kPa and varying p_{O_2} from 1.0 to 8.4 kPa. However, a steep decrease in selectivity was observed with an increase in p_{O_2} (see Fig. 37 D). For example, at 393 K, the selectivity decreased from 94.0 to 89.0% by increasing p_{O_2} from 1.0 to 8.4 kPa. The evaluation of kinetic parameters (see Table 4) for VA synthesis over supported Pd-Au catalysts indicate that the reaction proceeds via a Langmuir-Hinshelwood mechanism. For VA synthesis over the Pd-Au catalyst, as illustrated in Fig. 37 A and 36 B, a $p_{C_2H_4}$-dependent rate-increase was observed, which implies that the coverage of C_2H_4 - derived species is less than saturation on the Pd-Au surface. On the other hand, for the Pd-only catalyst the coverage of C_2H_4 was estimated to be at saturation based on the negative order of the rate with respect to $p_{C_2H_4}$. A positive reaction order with respect to p_{O_2} for both catalysts suggests that O_2 adsorption is blocked by adsorbed C_2H_4 and acetate species.

Table 4. Kinetic Parameters for the Synthesis of VA over Pd-Au/SiO$_2$ Catalyst, Power Law Functionality: $r_{VA} = k \cdot p_{C_2H_4}^{a} \cdot p_{O_2}^{\beta}$

T/K	**Constant rate (k)*10^{-2}/s^{-1}**	α	β	γ_{VA}/ 10^{-3}/s^{-1}
393	2.45	0.38±0.04	0.20±0.02	3.48
413	4.03	0.35±0.01	0.20±0.03	6.47
433	4.70	0.35±0.03	0.21±0.03	7.54

Rates obtained with $p_{C_2H_4}$ = 5.0 kPa, p_{O_2} = 1.0 kPa, p_{AcOH} = 2.0 kPa, the remainder N$_2$. Turnover frequency (TOF) was calculated based on: $r_{TOF,VA} = r_{VA} * m_{Pd} / D$, m$_{Pd}$ = Pd atom weight, D = dispersion of Pd. The dispersion of Pd was estimated from the Pd particle size measured by TEM; ca. 40% dispersion of Pd was estimated for the Pd-Au/SiO$_2$ catalyst, corresponding to ca. 3.2 nm Pd-Au particles.

As illustrated in Fig. 37 C and 37 D, the selectivity for VA formation increases with an increase in $p_{C_2H_4}$, and decreases with an increase in p_{O_2}. The rise in selectivity with an increase in $p_{C_2H_4}$ may be due to an increase in the C_2H_4 coverage, which favors VA synthesis more so than ethylene combustion. Since the coverage of C_2H_4 on the Pd-Au catalyst is less than saturation. The decrease of selectivity by increasing p_{O_2} implies that high coverage of adsorbed oxygen (O_{ad}) decreases VA formation and increases ethylene combustion. Therefore, a high selectivity towards VA formation is ensured by using a high ratio of $p_{C_2H_4} / p_{O_2}$.

Reaction rates as a function of temperature are shown in Fig. 38. By fixing $p_{C_2H_4}$ at 7.5 kPa and varying p_{O_2} from 1.0 to 8.4 kPa, the VA rates varied significantly with temperature. There are two regions where an apparent difference in the temperature effects can be seen: Region I (393 - 413 K) and Region II (413 - 433 K). The rates in Region I increase faster with temperature compared to the corresponding rates in Region II, which implies that ethylene combustion is favored at temperatures > 413 K. Apparent activation energies (E_a) of 40.0 ± 4.0 kJ/mol for Region I (very close to the E_a`s of 39.0 kJ/mol measured for Pd-only catalysts) and 15.0 ± 4.0 kJ/mol for Region II were calculated from the above data.

As mentioned earlier the kinetics of VA synthesis for the Pd-only catalyst has also been measured under identical conditions (refer to Table 2). Other than the fact the rate improves significantly by alloying of Pd with Au, the main difference between the two catalysts is in terms of the reaction order with respect to C_2H_4, i.e., negative for the Pd-only catalyst and positive for the Pd-Au catalyst (see Table 4). It should be noted that the reaction order with respect to acetic acid was observed to be approximately zero.

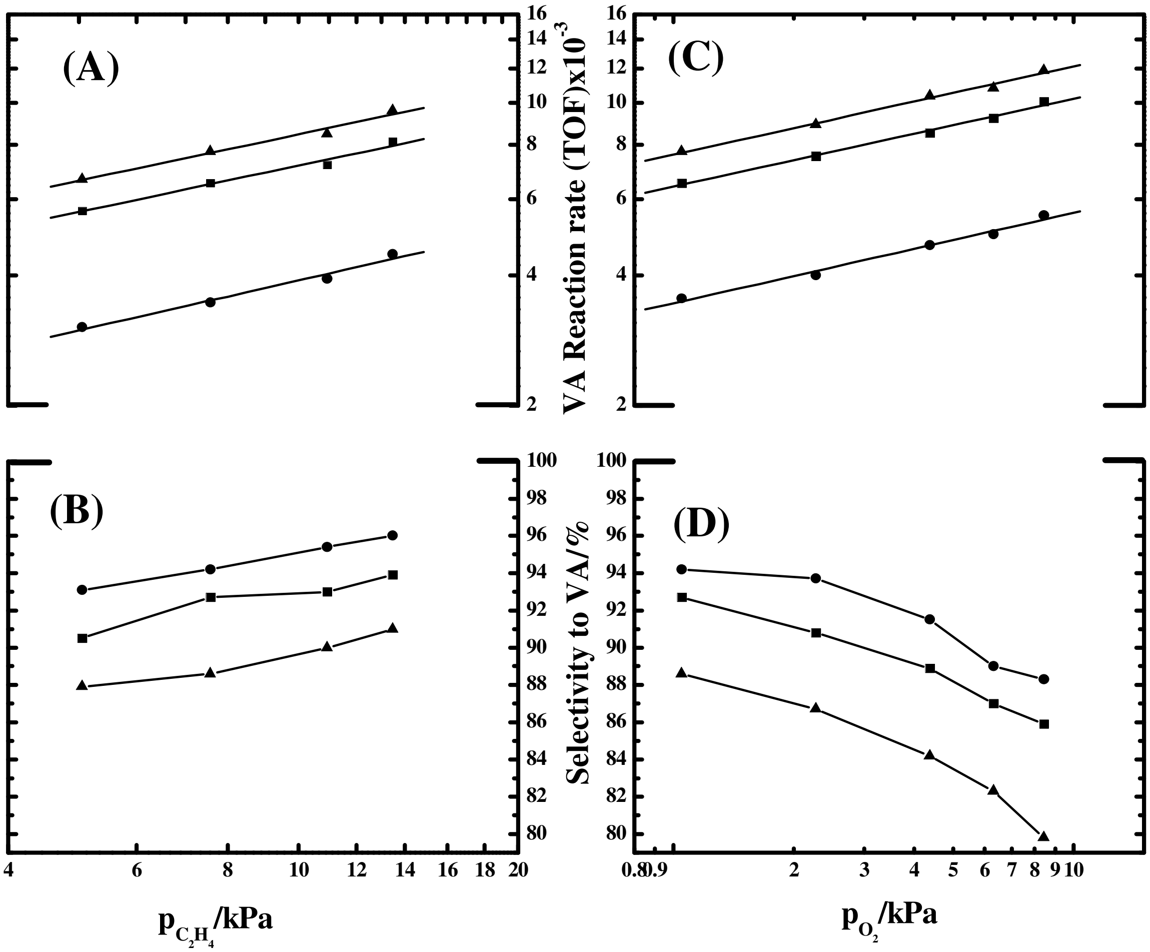

Fig. 37. $p_{C_2H_4}$-dependent reaction rate for VA synthesis (A) and selectivity (C) at feed gas of $p_{C_2H_4}$ = 5.0-14.0 kPa, p_{O_2} = 1.0 kPa, p_{AcOH} = 2.0 kPa, the remainder N_2; p_{O_2}-dependent reaction rate for VA synthesis (B) and selectivity (D) at feed gas of $p_{C_2H_4}$ = 7.5 kPa, p_{O_2} = 1.0-8.4 kPa, p_{AcOH} = 2.0 kPa, remainder N_2. Reaction conditions: 0.1-1.0 g of the Pd-Au catalyst, 30 - 60 ml/min of flow rate, temperatures of 433 K (▲), 413 K (■) and 393 K (●).

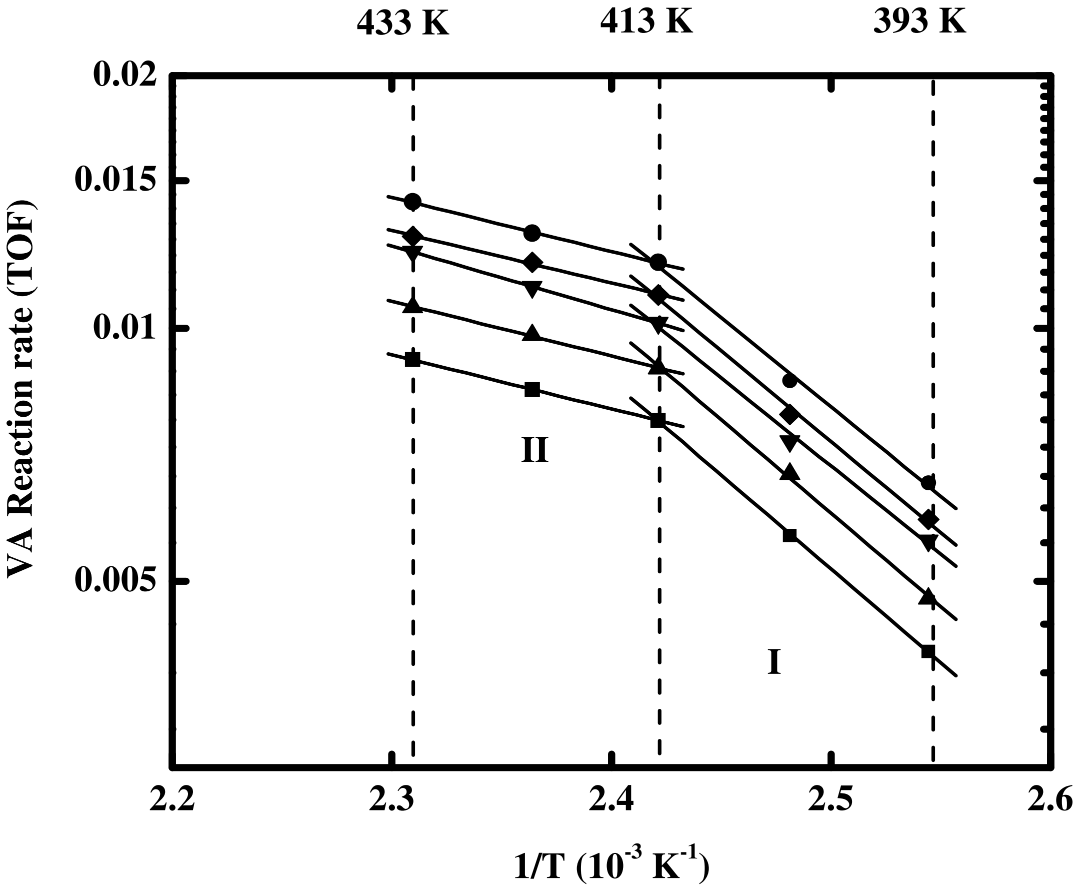

Fig. 38. Arrhenius plots for VA synthesis on the Pd-Au catalysts. Region I: 393 - 413 K, II: 413 - 433 K. Varying p_{O_2} at 1.0 kPa (■), 2.2 kPa (▲), 4.2 kPa (▼), 6.3 kPa (♦) and 8.4 kPa (●) while keeping $p_{C_2H_4}$ = 7.5 kPa, p_{AcOH} = 2.0 kPa, remainder N_2.

The kinetic data for VA synthesis over Pd-based catalysts are consistent with the reaction proceeding via a Langmuir-Hinshelwood mechanism. For VA synthesis over the Pd-Au catalyst, as depicted in Fig. 37A and B, a $p_{C_2H_4}$ - dependent rate-increase was observed at temperatures of 393 K, 413 K and 433 K, respectively, consistent with the coverage of C_2H_4 - derived species being less than saturation on the Pd-Au surface. This contrasts with the behavior observed for the Pd-only catalyst where the coverage of C_2H_4 was estimated to be at saturation based on the negative order of the rate with respect to $p_{C_2H_4}$ at similar reaction conditions [78,80]. On the other hand, a positive reaction order with respect to p_{O_2} for both catalysts suggests that O_2 adsorption is blocked by adsorbed C_2H_4, consistent with O_2 being the rate limiting reagent on the Pd-only catalyst; this point has been discussed in detail previously [78]. Moreover, the reaction orders at all three temperatures approximate those for the Pd-Au catalyst, consistent with a single reaction mechanism being operative in VA synthesis, independent of the reaction conditions.

As illustrated in Fig. 37 C and D, the selectivity for VA formation increases with an increase in $p_{C_2H_4}$, and decreases with an increase in p_{O_2}. Two competitive reactions are operative for VA synthesis over supported Pd-only catalysts [79,81,63]: ethylene combustion and VA synthesis. For a 5wt% Pd/SiO_2 catalyst, a mechanistic study of ethylene combustion in either a VA reactant mixture or an acetic acid-free gas mixture shows limited dissociative adsorption of oxygen, deduced from the negative order of the reaction with respect to $p_{C_2H_4}$. For a Pd-Au catalyst, the rise in selectivity with an increase in $p_{C_2H_4}$ may be due to an increase in the C_2H_4 coverage, which favors VA synthesis more so than ethylene combustion. That is, the coverage of C_2H_4 on the Pd-Au catalyst is far from saturation. The decrease of selectivity by raising the p_{O_2} illustrates that an excess of adsorbed oxygen (O_{ad}) accelerates ethylene combustion more so than VA formation. Therefore, to achieve a high selectivity toward VA formation, a high ratio of $p_{C_2H_4} / p_{O_2}$, is essential.

VA formation and combustion are greatly influenced by the reaction temperature. As shown in Fig. 38, two Arrhenius regions are apparent within the temperature range 393 to 433 K. Over a wide range of p_{O_2} with a fixed $p_{C_2H_4}$, the temperature - dependent rate increases more significantly between 393 and 413 K (Region I) than between 413 and 433 K(Region II), indicating that ethylene combustion was significantly enhanced at elevated temperatures, depletes O_{ad}, and suppresses the formation of VA. A possible consequence may be the reduction of the C_2H_4 coverage as the temperature is increased. On the other hand, a larger fraction of C_2H_4 is likely dissociated to a hydrocarbonaceous residue with an increase in the temperature; this species, in turn, is more easily converted by oxygen to CO_2. Consequently, the selectivity is dramatically reduced with an increase in temperature, as shown in Fig. 37 B and D. Interestingly, the similarity of the E_a values for both catalysts (region I for Pd-Au) suggests that VA synthesis mainly occurs at Pd sites.

Catalyst Deactivation

As mentioned earlier, the catalytic stability for Pd-only catalysts was investigated and it was observed that during the course of the VA reaction the loss of maximum reactivity of the catalysts was related to the particle size. For example, using Pd(1.0 wt%)/SiO_2 catalyst about 33 % activity was lost where as using Pd(5.0 wt%)/SiO_2 about 50 % activity was lost. For Pd(100) catalyst a loss of about 60 % was recorded. However, as illustrated in Fig. 39, under the same reaction conditions for Pd-Au catalyst the maximum rate, TOF of 11.0×10^{-3} s^{-1} was observed after 60 min of reaction time and a loss of about 25% of reactivity was monitored after 1000 min

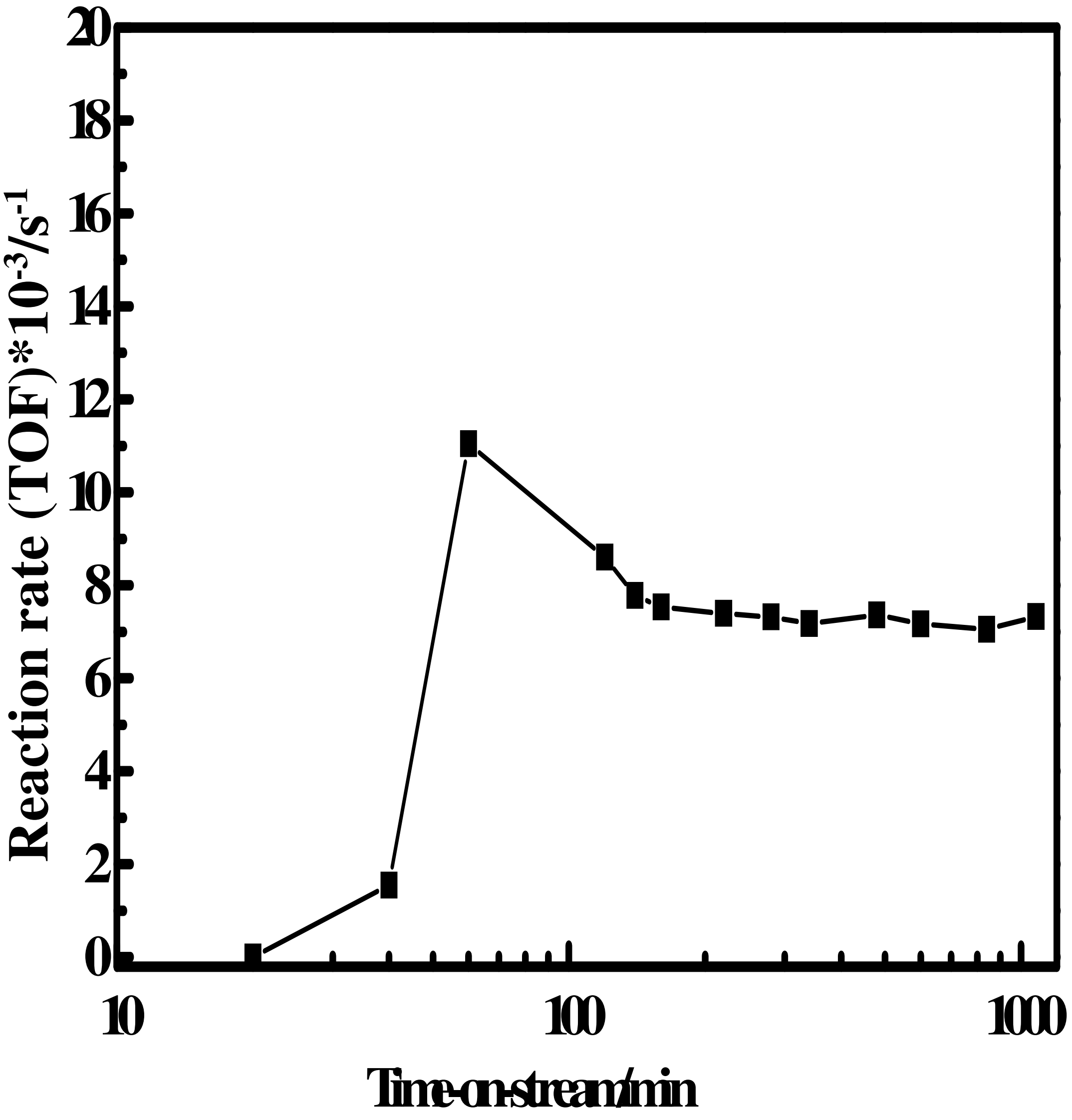

Fig. 39. Catalytic stability of Pd(1 wt%)-Au(0.4 wt%)/SiO_2 catalyst in the absence of VA, feed gas: $p_{C_2H_4}$ = 7.5 kPa, p_{O_2} = 6.3 kPa, rest N_2; flow rate: 60 ml/min, at 413 K.

(see Table 2). In comparison, the decay of reactivity over Pd-Au is much milder than over mono-Pd catalysts and is primarily attributed to sintering.

Sintering

The TEM results of Fig. 40 show that the sizes of the Pd-Au particles are distributed broadly over the range 1.0 – 13.0 nm while most of the particles lie between 2.0 and 7.0 nm. The corresponding average diameter is 4.2 nm after VA reaction. However, before reaction the average particle size was estimated to be about 3.2 nm. Surface composition determined by EDS indicates that the average Pd/Au atom ratio in region A in Fig. 35 (top) is 2.0, lower than the initially deposited ratio of 4.0; a ratio of 2.2 and 1.9 was observed for particle B and C, respectively. However, the ratio of Pd/Au decreased to 1.5 after reaction, as shown in region A of Fig. 40 (top), while the ratio for particle B and C in region A is 1.1 and 1.3, respectively.

Formation of Palladium Carbide and Surface Carbon

One of the important issues in using Pd-Au alloy catalysts is whether PdC_x is formed. Other questions about the formation of PdC_x are in terms of the extent of the deactivation of the catalysts due to the presence of PdC_x. Can PdC_x be removed completely through the reduction in H_2 atmosphere? What is the difference between the carbon species bonding to the surface of Pd-Au alloy and mono-Pd catalysts?

For supported Pd-Au catalysts, after reduction (see Fig. 36 A) a reflection feature is apparent at 39.8°, which is lower than that for the Pd <111> phase by 0.4°. Another peak was observed at 38.6° which corresponds to a Au-rich phase. As illustrated in Fig. 36 B, for the reacted catalyst, the peak for Pd-rich phase shifts to 39.0° while the one for Au-rich phase remains at 38.6°. After treating the reacted Pd-Au alloy catalyst at 623 K with H_2 gas for 4 h, the peak of the PdAu <111> phase in the Pd-rich alloy shifted down to 38.7° and merged with the peak of PdAu <111> phase in the Au-rich alloy as shown in Fig. 36 C. A similar downshift of PdAu reflections in the reaction has also been reported previously over a K^+ doped Pd-Au/SiO_2 catalyst and was attributed to the further alloying of Pd and Au rather than the penetration of carbon into the Pd bulk.

In the present study, XPS C1s spectroscopy was performed over the supported catalysts to gain more information about the carbon species on the Pd surfaces. XPS was measured over the reduced, after VA reaction and H_2-treated reacted catalysts. A straight line in C1s region was observed on a clean Pd (100) surface, where as, two peaks at binding energy(BE) of 285.3 and 290.0 eV were detected for the reacted catalyst, roughly assigned to the adsorbed hydrocarbon (C_xH_y) and carbonate/carboxyl (CO_3^{2-} / CO_3H^-), respectively. Two small peaks at 284.0 and 287.0 eV, assigned to graphite carbon I and adsorbed CO were also observed in the deconvolution.

Fig. 41 A and B show that graphite carbon dominates on both reduced Pd/SiO_2 catalysts. Meanwhile a small amount of hydrocarbon was also noticeable, but the carbonate/carboxyl was only found on the Pd(5 wt%)/SiO_2 catalyst (see Fig. 41 B). All carbon species were supposed to come from the preparation process and could not be removed through the pretreatment procedures. Surprisingly, there was only a trace amount of carbon on the reduced Pd-Au catalyst, as shown in Fig. 41 C. As shown in Fig. 42, four kinds of carbon species were detected at 288.1, 285.3, 284.0 and 282.0 eV. In particular, the peak at 282.0 eV was supposed to be due to the PdC_x-like species. Interestingly, after treating the reacted catalyst in H_2 (see Fig. 43) the peak at 282.0 eV disappeared for Pd(1 wt%)/SiO_2 catalyst and the supported Pd-Au catalyst, but was still

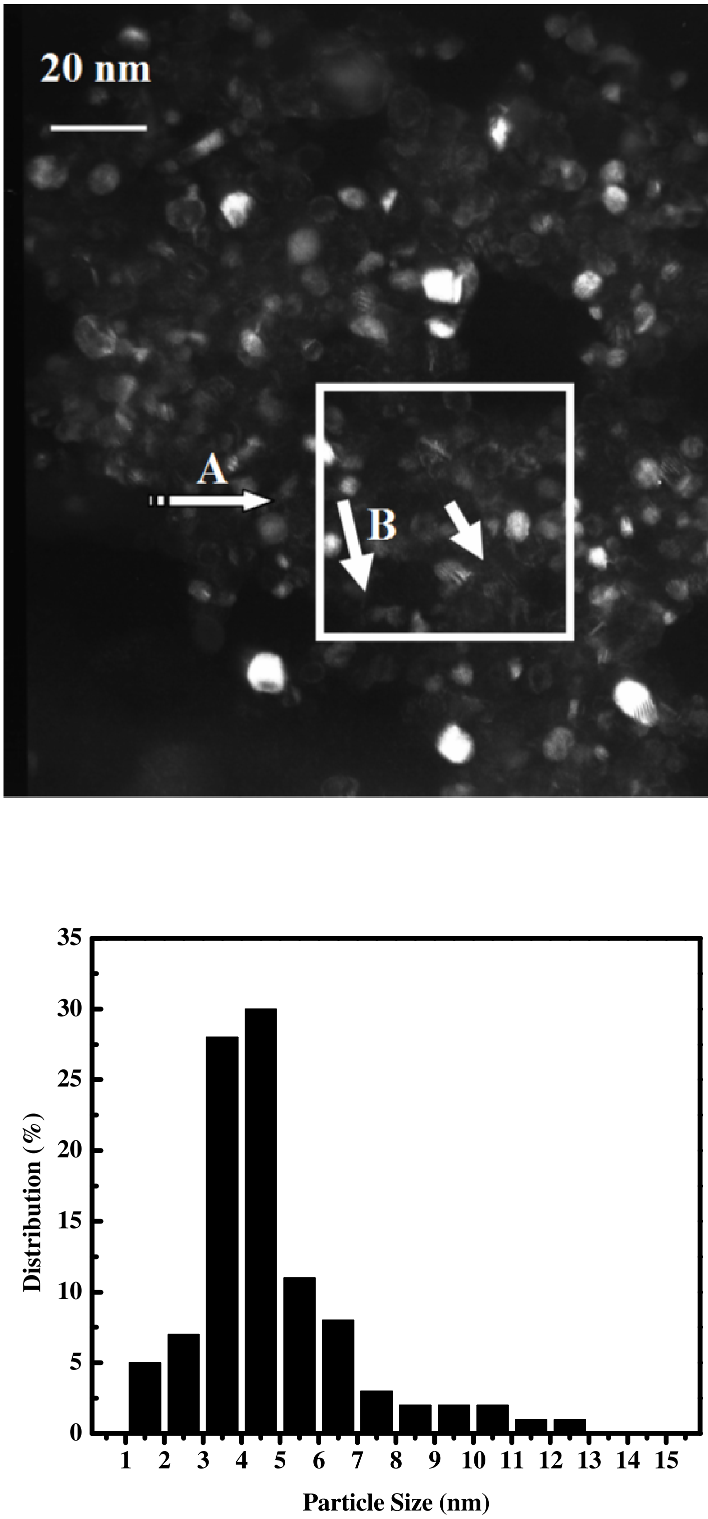

Fig. 40. TEM image of Pd-Au clusters for the reacted Pd-Au catalyst (top, for VA synthesis in a mixture of C_2H_4 = 7.5 kPa, O_2 = 1.0 kPa, AcOH = 2.0 kPa, remainder N_2, at 413 K for 100 hours), atomic ratio of Pd/Au in region A = 1.5/1, at particle B = 1.1/1 and C = 1.3/1; the Pd-Au cluster distribution is shown at the bottom.

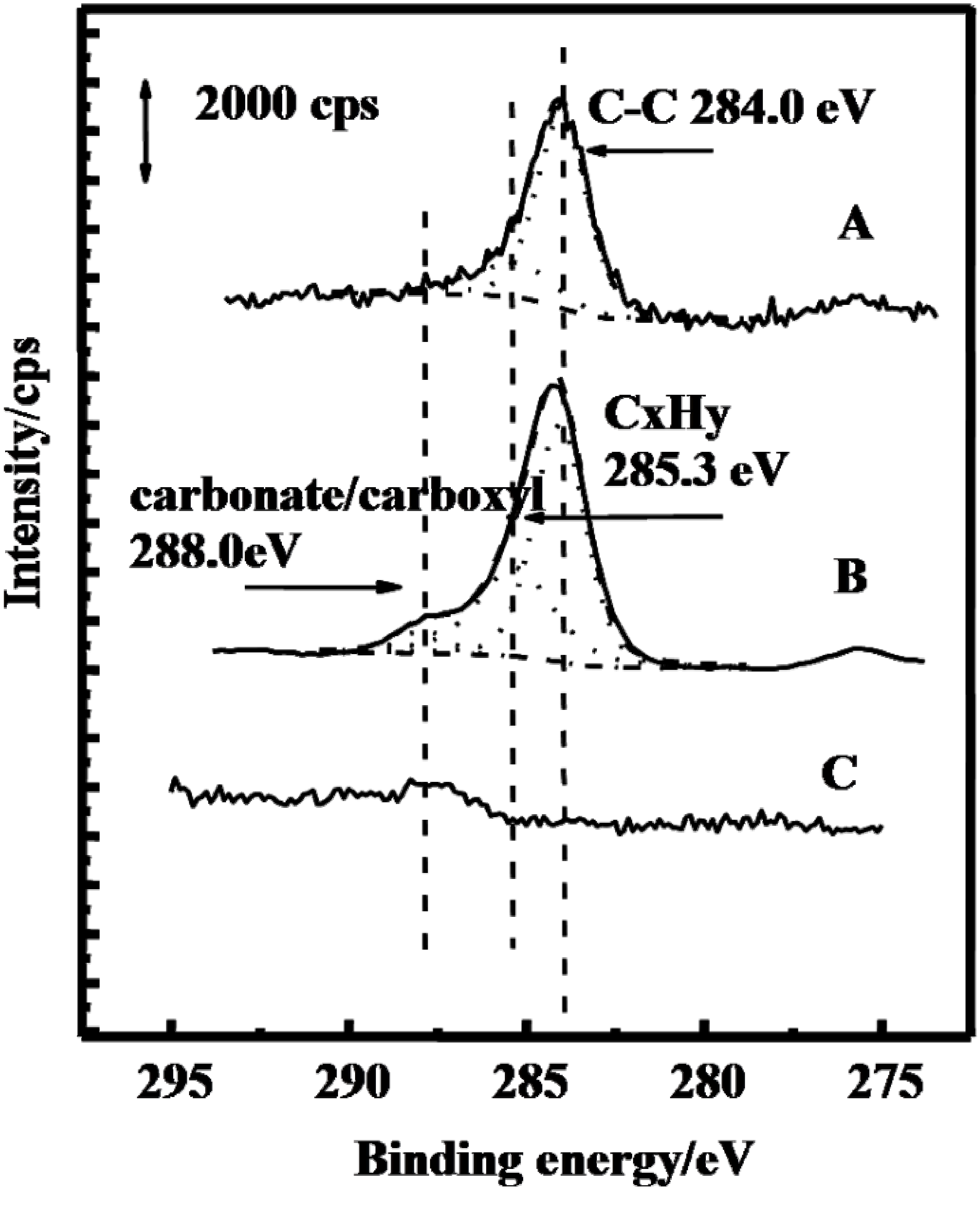

Fig. 41. C1s spectroscopy of reduced Pd-based catalysts. A: Pd(1 wt%)/SiO_2; B: Pd(5 wt%)/SiO_2; C: Pd-Au/SiO_2.

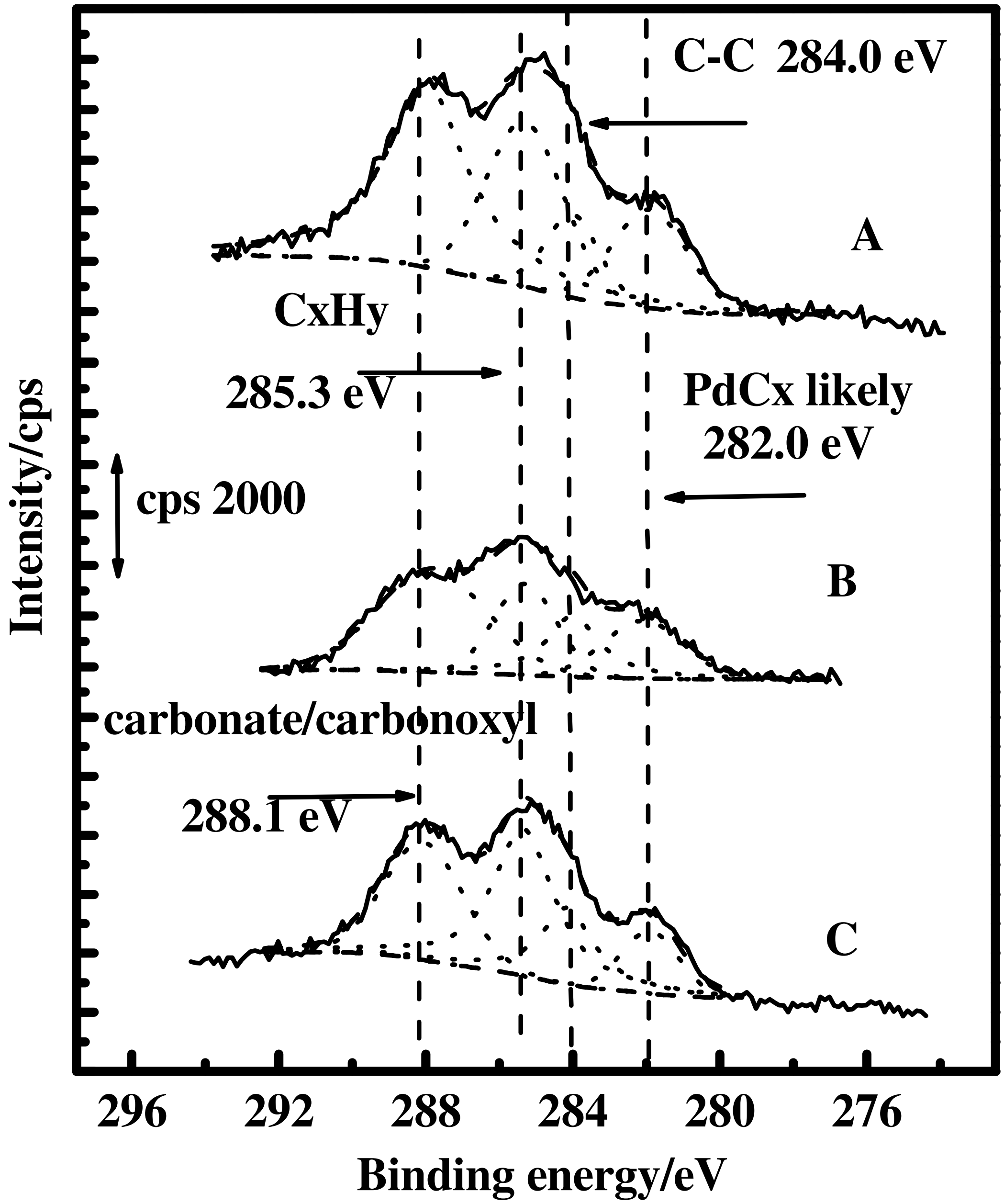

Fig. 42. XPS C1s spectroscopy of reacted Pd-based catalysts. A: Pd(1 wt%)/SiO_2; B: Pd(5 wt%)/SiO_2; C: Pd-Au/SiO_2.

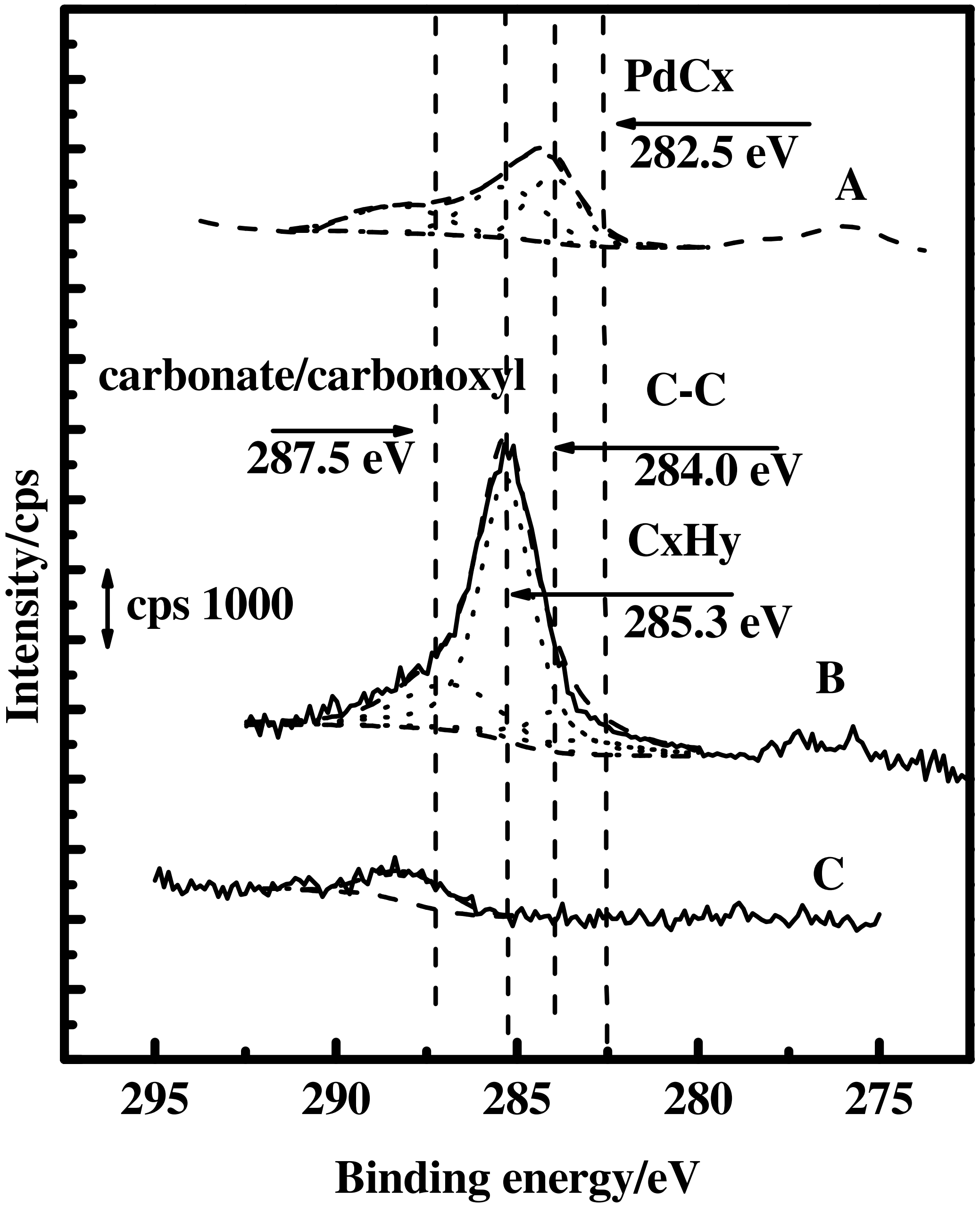

Fig. 43. XPS C1s spectroscopy of reacted Pd-based catalysts with H_2 treatment at 623 K for 4 hours. A: Pd(1 wt%)/SiO_2; B: Pd(5 wt%)/SiO_2; C: Pd-Au/SiO_2.

visible for the Pd(5 wt%)/SiO_2 catalyst. The feature in the C1s region over Pd-Au/SiO_2 catalyst indicated that deposited-carbon has been totally eliminated, see Fig. 43 C. A small peak at ca. 288.0 eV was ascribed to the mixture of Pd feature and contaminated carbon from the instrument.

The XPS spectroscopy for all reacted catalysts, see Fig. 42, suggested that Pd surface was covered with overlayer of deposited carbon which consisted of several carbon species, including the Pd carbide. Illustrating carbide formation in Pd-Au/SiO_2 catalyst becomes more complex considering the possible alloying between Pd and Au in the reaction, which also leads to the downshift of Pd reflections in XRD. For the same catalyst doped with potassium, composition of Au-rich phase is quite stable under all conditions; however, the variation of the Pd-rich phase was observed after heating in different gas [77]. For instance, the time-dependent downshift of Pd-Au <111> was detected within 100 hours as heated in H_2 at 413 K (reaction temperature). In contrast, there was almost no change under the same process in N_2. Therefore, we argue that the carbide in the Pd-Au alloy is quite different with that in mono-Pd catalyst, it is only superficial species and weakly bonded to Pd-Au. Instead, the reactant-induced structure change should be primarily responsible for the downshift of Pd-Au <111> in the reaction. Similarly, in the present study by referring to the diffraction feature of the reduced catalyst, see Fig. 36 A, the downshift of Pd-Au <111> phase, Fig. 36 B, was determined after reaction as well as in Fig. 19 and 20 for Pd <111> in Pd/SiO_2 catalysts. It was found that the reflection of Pd-rich phase moved down further; see Fig. 36 C, with treating the reacted Pd-Au alloy in H_2 at 623 K. The downshift of the Pd-Au <111> during the reaction and H_2 treatment may be caused by the reactants-induced phase transition. Else, the restoration of Pd XRD reflections should be observed after H_2 treating the reacted catalyst as was monitored for the mono-Pd catalysts. On the other hand, the XPS results indicated that the contaminating-carbon was more easily to be removed from Pd-Au alloy than that of mono-Pd by either oxidizing/reducing precursor (Fig. 41) or H_2-treating reacted catalyst (Fig. 43).

In summary, PdC_x is formed in a Pd-only catalyst during the synthesis of VA. Reducing the Pd particle size can enhance the resistance of Pd for carbide formation, this resistance likely being the reason for the improvement in stability seen for highly dispersed Pd for VA synthesis. On the other hand, there is no evidence for PdC_x in a Pd-Au alloy catalyst following VA synthesis. Alloying Au with Pd apparently inhibits the reaction between Pd and interstitial carbon and appears to be an effective way to prevent PdC_x formation in Pd-based catalysts. The reason why Pd-Au alloy shows strong resistance to carbide formation is apparent from our studies of VA synthesis using model catalysts and will be addressed in the later sections. Hence, reducing the size of Pd particle and alloying Pd with Au are suggested to be effective way to prevent the carbide formation.

Poisoning by Carbon Monoxide

VA synthesis was investigated in the presence of CO (0-1.0 kPa) using a mixture of C_2H_4 (7.5 kPa), O_2 (1.0 kPa) and AcOH (2.0 kPa) at 413 K over the supported Pd-Au catalyst. Fig. 44 shows that the addition of CO strongly poisons the active sites and suppresses VA production. The reaction time required for complete reduction of VA activity due to the presence of CO in the reactant gas stream was observed to be about 60 min. Almost same amount of time was required to completely restore the activity following the removal of CO from the reactant stream. Furthermore, it was observed that the amount of CO_2 formed also decreased simultaneously with the decline in the rate of VA formation. Also the onset of CO oxidation over the same catalyst

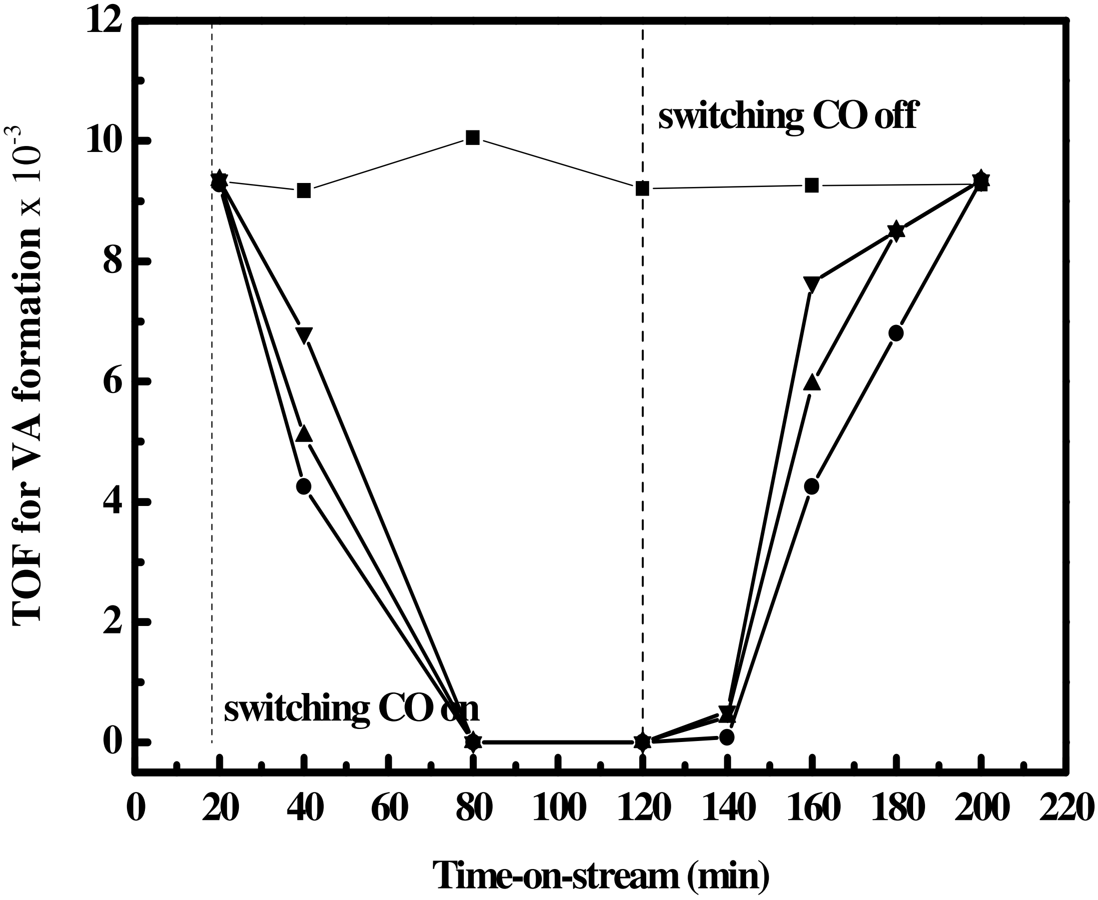

Fig. 44. VA synthesis in the presence of CO at 413 K in the feed gas of $p_{C_2H_4}$ = 7.5 kPa, p_{O_2} =1.0 kPa, p_{AcOH} = 2.0 kPa, remainder N_2, p_{CO} : 0 (■), 0.1 kPa (▼), 0.5 kPa (▲), 1.0 kPa (●).

was detected at 483 K (using a feed gas of 3.0 % CO and 3.0 % O_2). Hence, the O_{ads} needed for VA synthesis, is not consumed by the CO oxidation reaction.

Thermal Deactivation

The enhancement in the catalytic properties of Pd upon alloying with Au has led to many investigations to understand the changes happening in the surface structure of the alloy catalysts. It was observed that Au preferentially segregates to the surface in Pd-Au alloys [125-127]. On the other hand, another study showed that Pd-Au clusters consist of a Au-rich core covered with a monolayer of Pd [128]. Pd-Au/SiO_2 catalyst was prepared by depositing Pd-Au particles onto a high surface area SiO_2 and used for VA synthesis. Attention was given to the impact of reduction temperature on the catalyst structure, especially the ratio of Pd-Au at the catalyst surface. The composition of Pd-Au particle was investigated with high resolution SEM-EDX and XPS.

The reactivity and selectivity for VA formation were measured at 413 K in O_2 (1.0 kPa), AcOH (2.0 kPa) and C_2H_4 (7.5 kPa) with N_2 as the balance. As depicted in Fig. 45, the reaction rate increased from $22\times10^{-6}\ mol\cdot g_{PdAu}^{-1}\cdot s^{-1}$ to $28\times10^{-6}\ mol\cdot g_{PdAu}^{-1}\cdot s^{-1}$ upon raising the reduction temperature from 573 to 723 K; the rate decreased sharply to $13\times10^{-6}\ mol\cdot g_{PdAu}^{-1}\cdot s^{-1}$ with a further increase to 773 K. Meanwhile, the selectivity of VA was stable at ca. 93%, independent of the reduction temperature.

The SEM images in Fig. 46 show that nano-sized particles (white spots) are highly dispersed on SiO_2 surface. The size distribution in the range of 1 - 10 nm for all catalysts are shown in Fig. 46, which reveals that the distribution is not influenced by a change in the

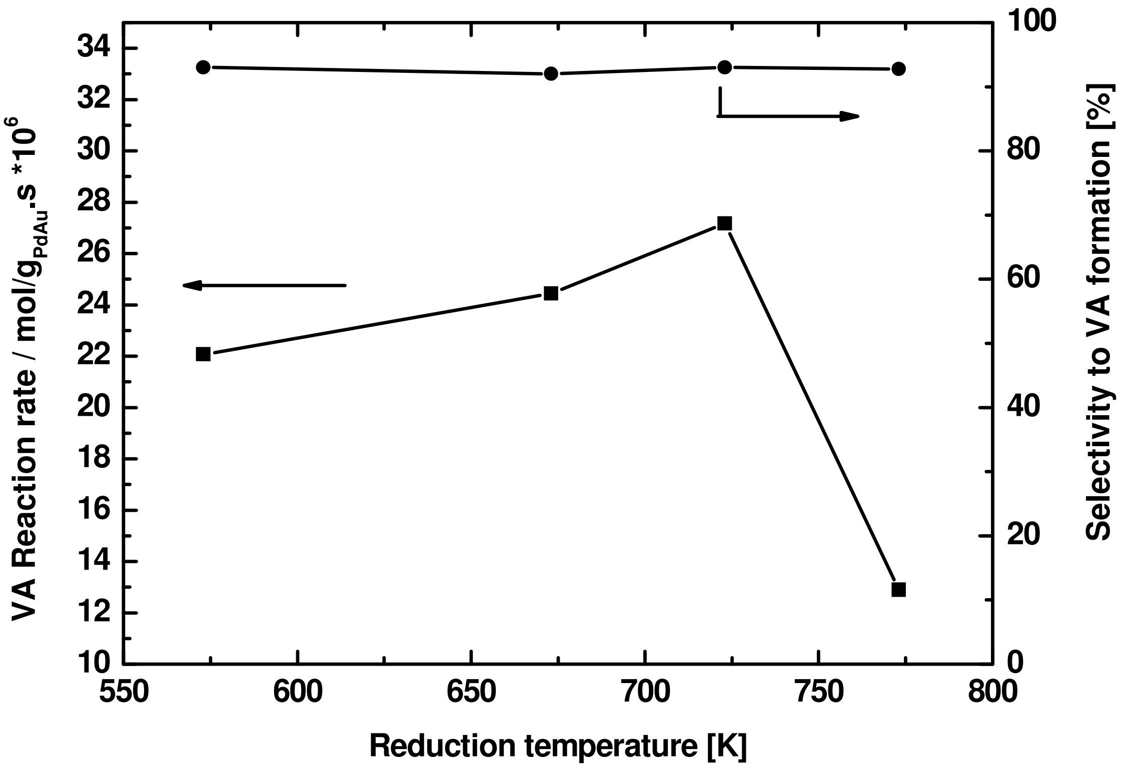

Fig. 45. VA reaction rates as a function of catalyst reduction temperature. (■): reaction rates and (●): selectivity for VA formation. $p_{C_2H_4}$ = 7.5 kPa, p_{O_2} =1.0 kPa, p_{AcOH} =2.0 kPa, remainder N_2; flow rate: 60 ml/min, reaction temperature: 413 K, flow rate: 60 ml/min.

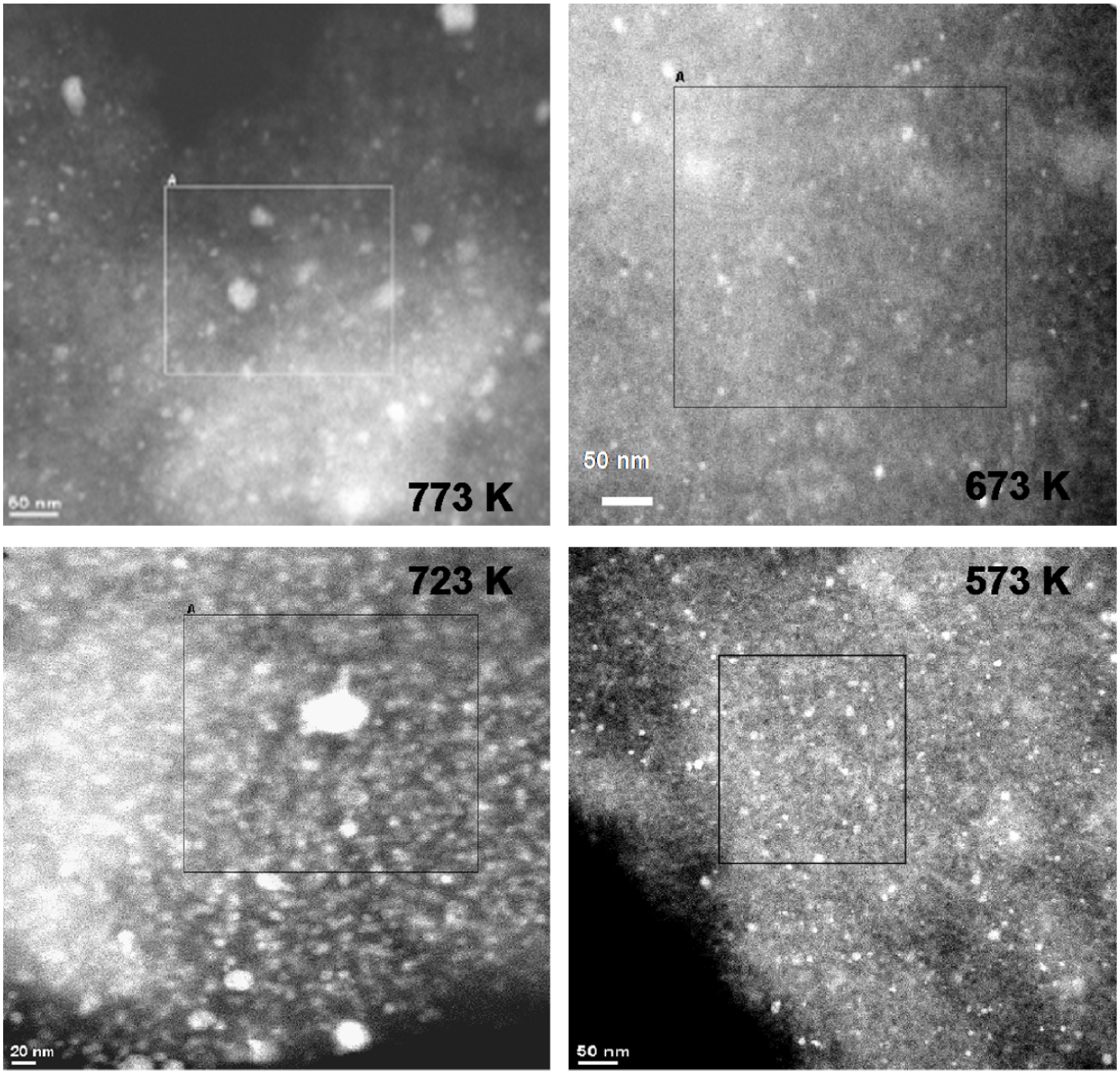

Fig. 46. SEM images of Pd-Au/SiO$_2$ catalysts reduced at various temperatures.

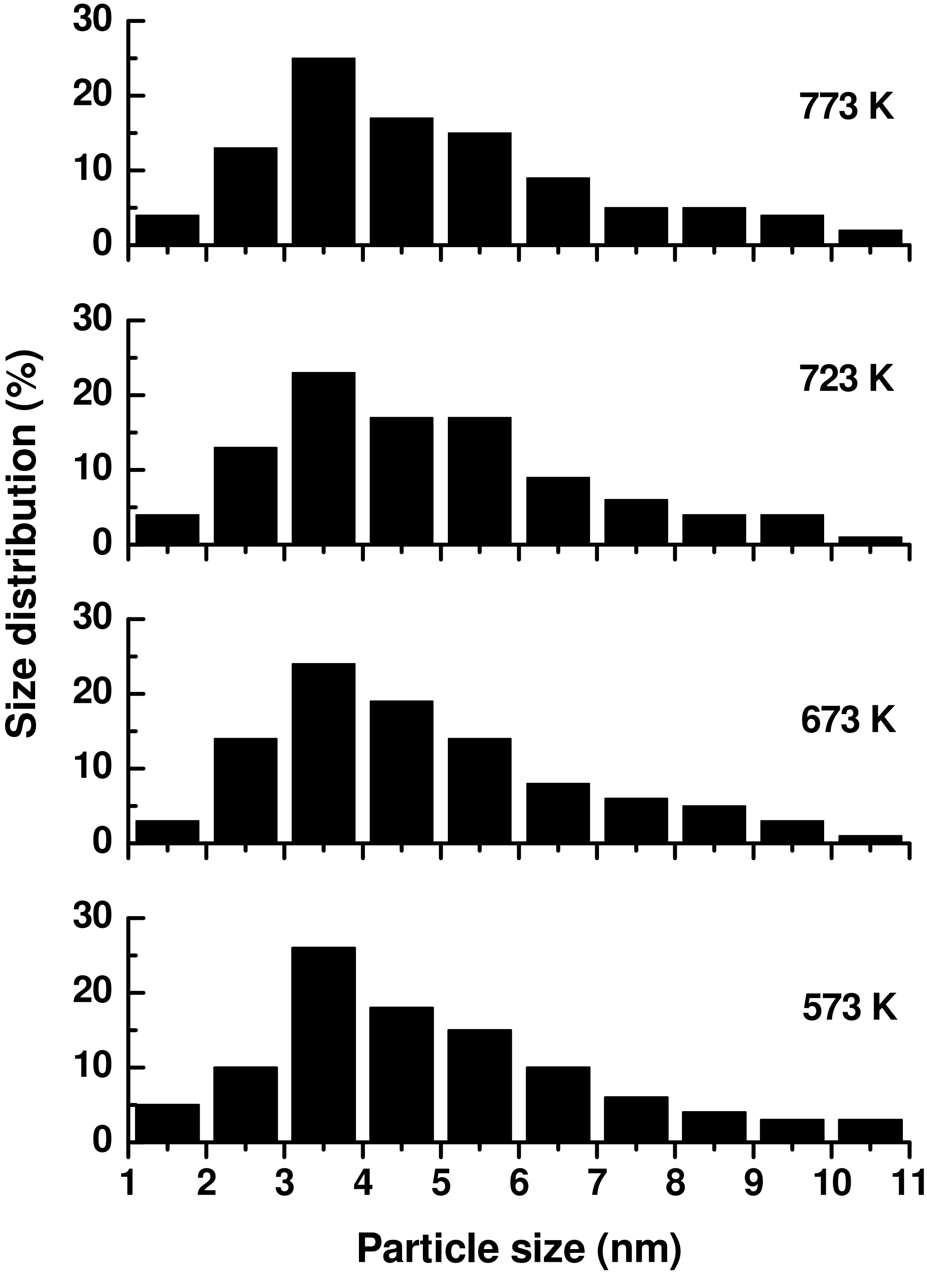

Fig. 47. Size distribution of metal particles on catalysts reduced at various temperatures.

reduction temperature. The average particle size for both catalysts is estimated to be 3.5 ± 0.3 nm (see Fig. 47).

Due to the overlap of the Pd $3d_{5/2}$ and Au $4d_{5/2}$ features, evaluation of the Pd chemical state was based on the Pd $3d_{3/2}$ BE. The XPS data of Fig. 48 shows that the BE of Pd $3d_{3/2}$ is 339.5 eV at 573 K, 339.6 eV at 673 and 723 K, and shifts to 340.2 eV at 773 K, indicating that metallic Pd^0 is predominant on the surface of all the catalysts. Deconvolution of the Pd $3d_{5/2}$ feature indicates that the Au $4d_{5/2}$ feature grows with an increase in the reduction temperature.

As depicted in Fig. 49, EDX shows that the atomic ratio of Pd-Au decreases from 2.0 at 573 K to 1.0 at 773 K, values lower than 4.0 found for the catalyst precursor. It is noteworthy that EDX analysis is centered on the region defined by the square frame in each image of Fig. 47 (A). In principle, EDX utilizes X-rays that are emitted from the sample during bombardment by the electron beam to characterize the elemental composition of the analyzed volume. Features or phases as small as about 1µm can be analyzed. The data from Fig. 47 shows that most of the particles are in the range of 2 - 6 nm. The estimated composition likely represents the average surface composition of the supported nanoparticles; on the other hand, the Pd-Au ratio of the individual particles was also observed to be distributed randomly over a wide range, including Pd-only and Au-only particles. The same trend of the Pd-Au ratio varying with reduction temperature was also detected by XPS. The ratio of the peak area of Pd $3d_{3/2}$ - Au $4d_{5/2}$ and Pd $3d_{3/2}$ - Au $4f_{5/2}$ decreased with increasing reduction temperature. SEM-EDX and XPS implies that an increase in the reduction temperature leads to Au surface enrichment but with little effect on the particle size. Furthermore, the invariance in selectivity throughout the reduction temperature regime is consistent with the reaction occurring on the same type of active

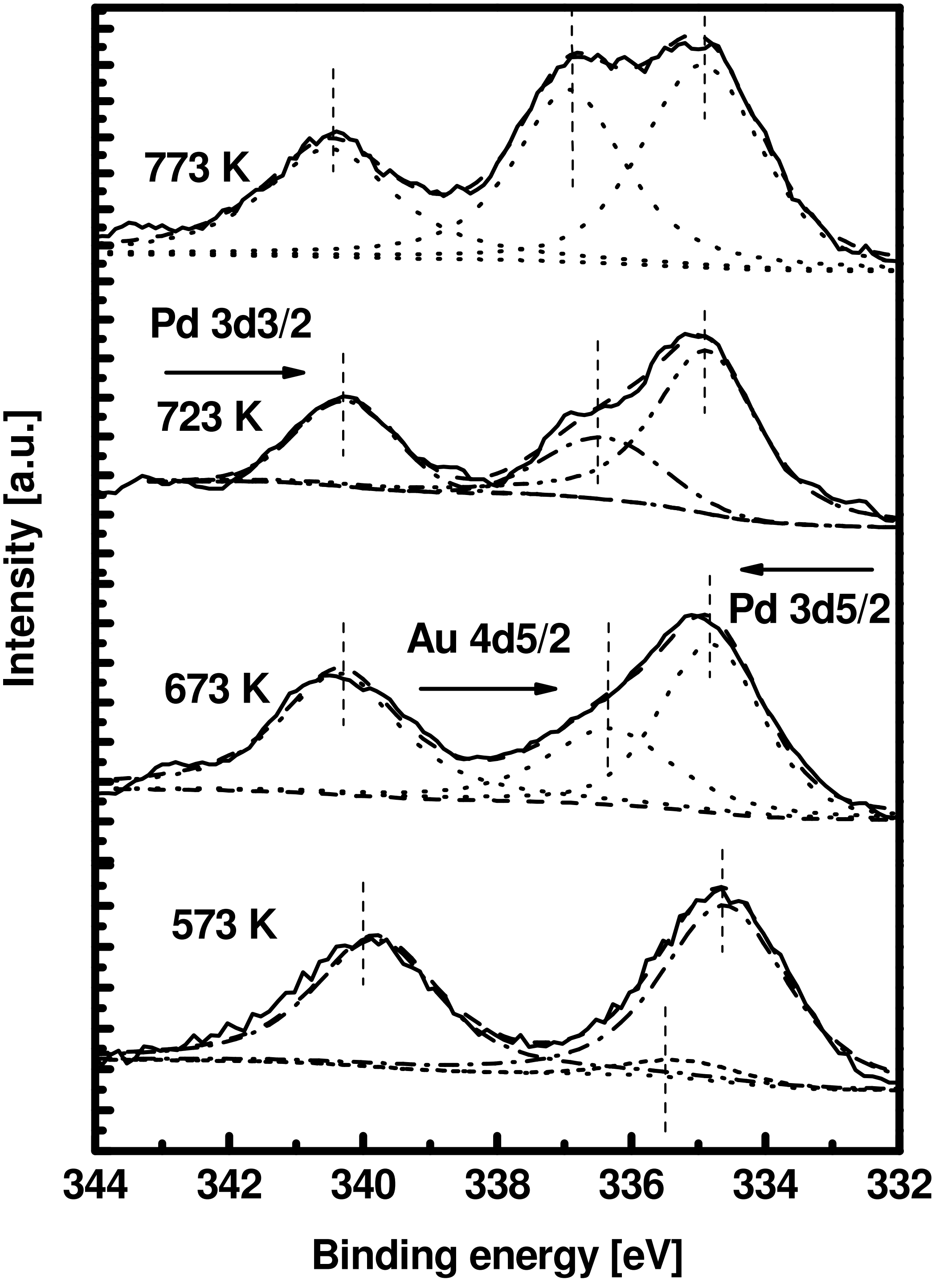

Fig. 48. XPS of Pd 3d region as a function of the reduction temperature of Pd-Au/SiO$_2$.

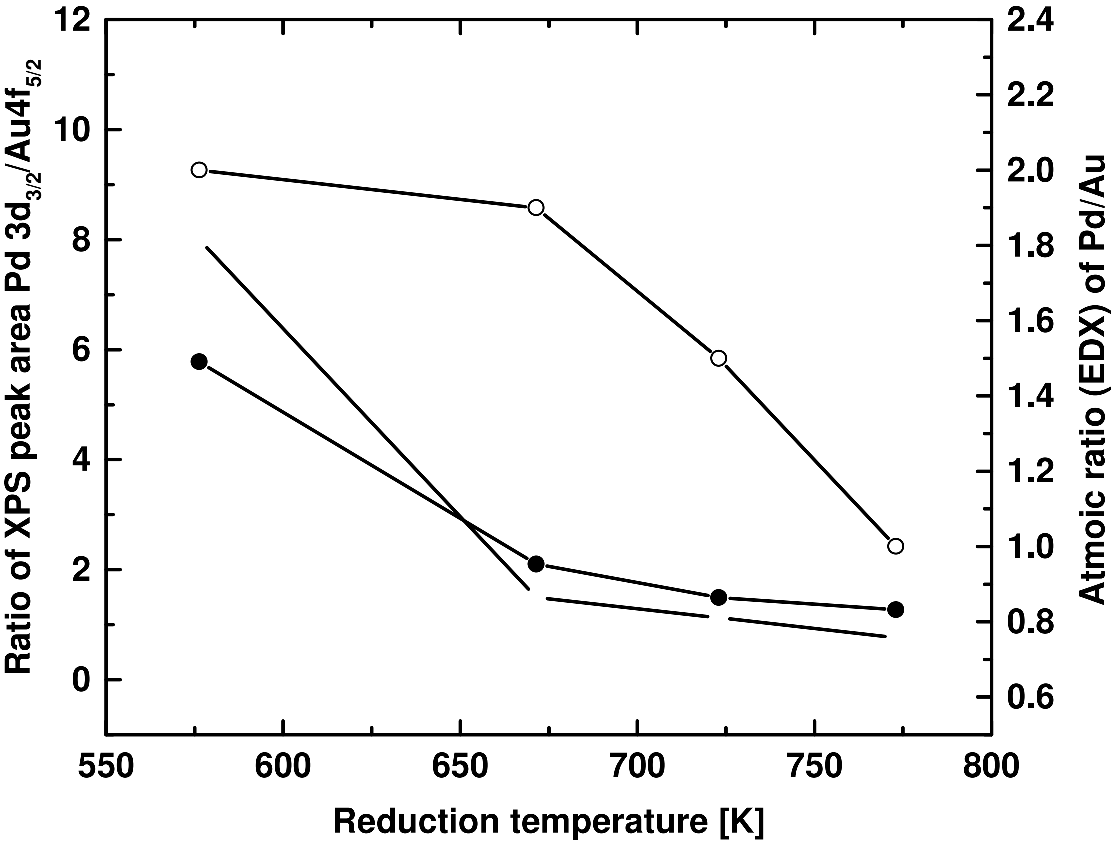

Fig. 49. Pd/Au ratio determined by EDX and XPS as a function of the catalyst reduction temperature.

site. The reactivity increase with increasing reduction temperature from 573 to 723 K is likely related to reconstruction of the particle surface.

Although some understanding regarding the surface composition of the Pd-Au alloy catalysts could be obtained by the use of various characterization techniques on supported catalysts, an in-depth knowledge is hard to achieve. As mentioned earlier, only limited knowledge can be achieved by using heterogeneous catalysts allowing us to relate the parameters such as, the composition, operating temperature, etc., to measurable global characteristics of the catalysts, such as, selectivity, activity, etc. Further understanding of the functioning of these catalysts and the formation and the working of the active sites is possible by using bimetallic model catalysts. In the coming sections this issue will be addressed.

Planar Pd-Au Catalysts

Bimetallic systems find extensive applications in catalysis, semiconductors, electrochemistry, etc. For example, these catalysts were extensively used in hydrocarbon reforming in the 1960’s and 70’s [18]. Due to this many surface science investigations have endeavored to unravel the chemical, electronic and physical properties of these systems [19-25]. The modern surface scientist is confronted with these questions and knowledge of these systems is required to design and understand the complex heterogeneous catalysts. There are two methods of production of the bimetallic surfaces [19]. The first one involves vapor deposition of one metal onto a clean well-defined single crystal surface in UHV. The second method consists of cutting and polishing an alloy single-crystal followed by cleaning in UHV. The former method has been much popular and has produced exciting results. Using these crystalline alloy films one can expect to study structure-function relationships by correlating the atomic structure with the electronic and chemical properties.

Surface Structure and Composition

The reactivity of metal surfaces is a critical function of composition and structure with alloys often showing unique properties compared to the corresponding single component metals [129-131]. For example, mixtures of Pd and Au are used as catalysts for a number of applications [132-135] including hydrogen fuel cells [136] and pollution control [97]. The addition of Au to Pd significantly enhances the catalytic activity, selectivity and stability; however, the details of this promotional effect are not well-understood.

Pd and Au alloys are completely miscible, with the heats of formation of Au-Pd alloys at 300 K being negative over the entire composition range; maximum stability occurs at ~60% Au [133]. Large negative enthalpies were observed which are indicative of an attractive interaction between the alloy constituents and a tendency to order. The lattice parameters of Au-Pd alloys at 300 K vary from 0.389 nm for pure Pd to 0.408 nm for pure Au with a small negative deviation from Vegard's law [137]. Short-range ordering in Au-Pd alloys has been reported and reviewed by Allison, et al [133]. Early work on their properties concluded that the 0.6 d-band vacancies of pure Pd fill at an alloy composition of ~60% Au which stimulated studies of the catalytic properties of Au-Pd mixtures at this critical composition, e.g., ortho, para-hydrogen conversion [138]. However, in surveying a number of reactions, the consensus is that surface composition is more important for adsorption and catalysis than is the bulk electronic structure [133,139-142]. There is still considerable uncertainty in the interpretation of the surface properties, since the surface composition can differ markedly from the bulk, and the surface atoms can be quite mobile under reaction conditions. In any case, theoretical calculations have shown a correlation among surface strain, adsorption energy, and activation barriers for reaction [143].

A number of studies have shown that the surface composition of Au-Pd mixtures differs from the respective bulk composition, with the surface being enriched in Au [125-128]. Surface enrichment in Au is consistent with Au having a much lower surface free energy compared with Pd. AES studies of Au-Pd alloy surfaces containing various bulk compositions show that Au is significantly enriched in an annealed surface [128]. These results have been confirmed using LEISS, a technique particularly sensitive to the top-most surface layer. The effect of annealing temperatures on the surface composition of Pd and Au (5 ML Pd/5 ML Au/Mo(110) and 5 ML Au/5 ML Pd/Mo(110)) was investigated using LEISS [144,145]. After annealing to high temperatures the inter-diffusion of Pd-Au is clearly evident. For example, at 800 K much of the surface is enriched in Au while surface concentration of Pd is less. Hence, between 700 and 1000 K a stable alloy of $Pd_{0.2}Au_{0.8}$ composition could be formed using a 50-50 mixture of Pd and Au. In fact, the sequence of deposition of the thin films of Pd and Au do not matter. The LEISS data were further obtained at different ratios of Pd and Au compositions to recognize the surface concentration phase diagram. As shown in Fig. 50 LEISS results of Au-Pd thin films supported on a refractory single crystal Mo(110) surface are in excellent agreement with those obtained from bulk alloys [127,128,144,145]. The reason for the significant surface enrichment of Au in a Pd-Au alloy is because of the lower surface free energy of Au in comparison to that of Pd. For Pd-Au/SiO_2 model catalysts similar enrichment in the surface concentration of Au is observed for different bulk ratios of Pd and Au. It is evident that the surface segregation of Au is more significant for Pd-Au planar surfaces [144]. Nevertheless, the study clearly demonstrates that the properties related to the surface composition can be well studied by using model catalysts and that the supported catalysts have similar surface composition as compared to model Pd-Au thin film catalysts.

There are only a few studies of Au-Pd alloy single crystal surfaces using surface-layer sensitive techniques [146,147]. LEISS studies of $Au_3Pd(113)$ [147] and $Au_3Pd(100)$ [146] surfaces show these surfaces to consist essentially of a Au layer; Pd is found only within the second atomic layer. Such surface segregation is common in metal alloy surfaces [76,148] with all Au-containing alloys showing preferential surface segregation of Au [149,150].

Based on the surface composition of Au-Pd alloys, epitaxial growth of a Pd monolayer on Au(111) should be thermodynamically unstable even at rather moderate temperatures. Koel and coworkers [151] carried out detailed investigations of Pd overlayers on Au(111) using AES and LEIS. Following the deposition of Pd at 150 and 300 K, results consistent with a van der Merwe, i.e., layer-by-layer growth mode was observed. At 500 K, however, the Pd AES intensity is markedly smaller while the Au AES value is larger than the corresponding values at 150 and 300 K. These observations qualitatively indicate alloying or inter-diffusion of a Pd monolayer at 500 K. Lambert and coworkers [152] have addressed Pd submonolayers on Au(111)-($22 \times \sqrt{3}$) where Pd islands initially nucleate and grow at the elbows near the surface edge dislocations of the Au herringbone reconstruction. A morphological evolution of these islands with increasing Pd coverage was observed and provides an excellent explanation for their catalytic behavior.

Behm et al. [153], using high resolution STM images obtained from Pd-Au alloy surfaces prepared by electrochemically co-deposition of Pd and Au onto Au(111), clearly resolved two types of atoms with different apparent heights and shapes, arranged in a hexagonal lattice with a lattice spacing equal to that of Au(111) (see Fig. 51). These STM images with

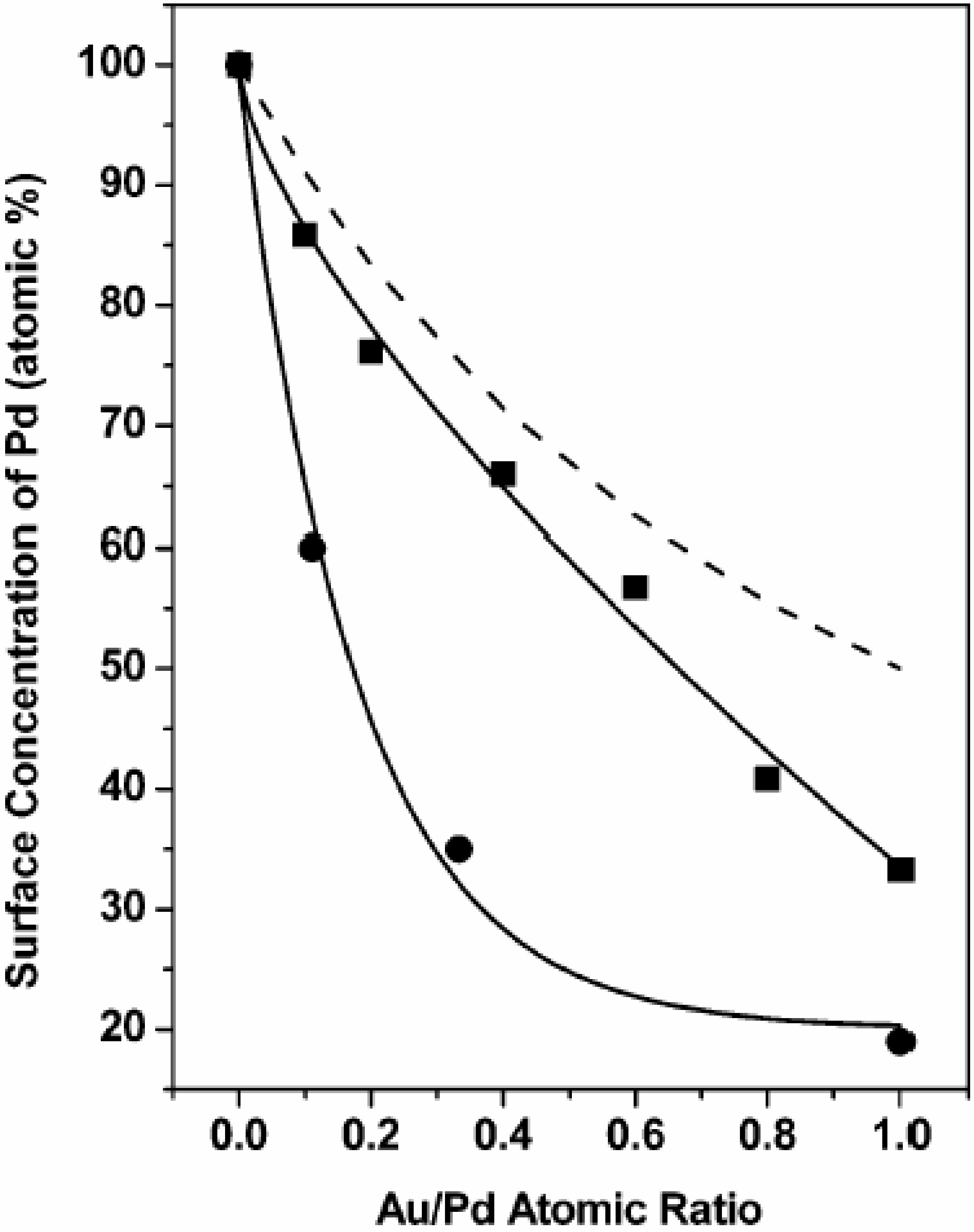

Fig. 50. Surface concentration of Pd (●) for Au-Pd thin films on Mo(110) after annealing to 800 K, (■) after Au (0.1 – 1.0 ML) deposition on 1.0 ML Pd/SiO_2 and annealing to 800 K and the dashed line is calculated Pd concentration [144].

atomic contrast showed that a single, uniform Au-Pd alloy phase with a disordered metal-atom arrangement can be formed without phase separation into Pd and Au domains.

Recent studies in our laboratories using IRAS with CO as a probe molecule clearly demonstrated the formation of isolated Pd surface sites surrounded by Au on Au-Pd thin films supported on a Mo(110) surface [145,154] and for Pd on Au(111) [155]. IRAS spectra is shown in Fig. 52 as a function of the CO exposure at 90 K onto a 5 ML Pd/5 ML Au/Mo(110) surface annealed at 600 K for 20 minutes. After relatively a low exposure of CO (< 0.10 L), two prominent stretching features are visible at 2087 and 1940 cm^{-1}, related to linearly- and bridged-bound CO on metal surfaces, respectively. These assignments are consistent with the CO adsorption features on Pd(111) at 2110~2080 cm^{-1} for linearly bound CO, at 1965~1900 cm^{-1} for 2-fold bridging CO and at 1900~1800 cm^{-1} for 3-fold bound CO species. Also, the features are similar to the assignments of 1910 and 2090 cm^{-1} to bridging and a-top sites bonding, respectively, for Pd/Au(111) by Koel et al. After CO coverage was increased (≥ 0.20 L), a new feature was apparent at 2105 cm^{-1} and saturated after 0.5 L CO dose. Since the vibrational frequency of CO on atop sites of Au fall within the range 2120~2100 cm^{-1} [156] and disappear below 200 K (which is much lower than CO atop adsorption on Pd), this feature at 2105 cm^{-1} is assigned to CO a-top on Au [145]. Fig. 52 shows CO on a 5 ML Pd/5 ML Au/Mo(110) annealed at 800 K for 20 minutes. A distinct feature at 2087 cm^{-1} corresponding to CO atop on Pd appears at CO coverage < 0.10 L is observed and after increasing the CO exposure, a second feature at 2112 cm^{-1} corresponding to CO atop on Au is observed. Multi-fold CO vibrational features were not visible on this surface, indicating that the formation of surface Pd atoms isolated by Au atoms ($PdAu_6$). These results demonstrate that much of the deposited Pd atoms diffuse into the bulk of the catalysts forming an interface of Pd-Au alloy with a small

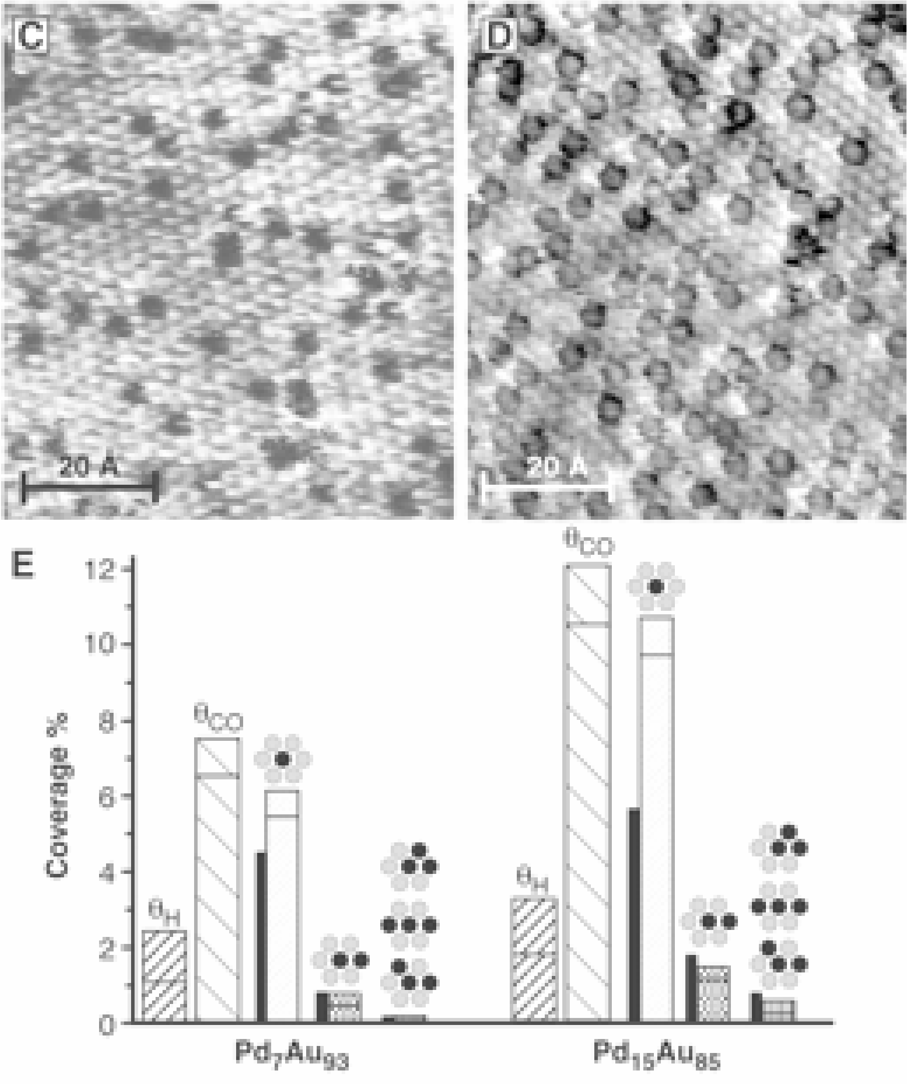

Fig. 51. In situ atomic resolution STM images of PdAu alloys electrodeposited on Au(111) for (A) $Pd_{07}Au_{93}$; and (B) $Pd_{15}Au_{85}$. Pd atoms appear larger and, depending on tunneling conditions, brighter or darker than Au atoms. (C) Surface coverages of Pd monomers, dimers, and trimers, as obtained from atomically resolved STM images [153].

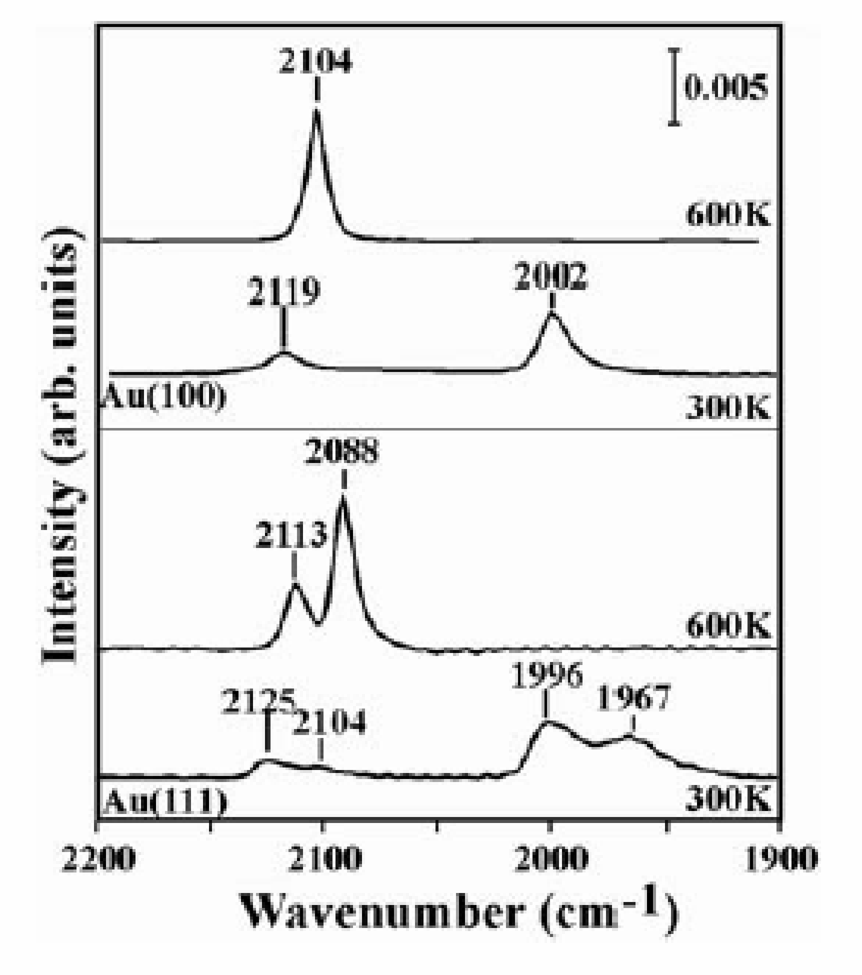

Fig. 52. IRAS spectra after CO adsorption at 90 K on 4 ML Pd/Au(100) and 4 ML Pd/Au(111). Pd was deposited on Au(100) and Au(111) at 90 K and subsequently annealed to 300 and 600 K for 10 minutes each.

amount of Pd atoms forming Pd monomers, Au_4Pd on Au(100) and Au_6Pd on Au(111) after annealing. This assumption is in agreement with LEISS results (Fig. 50) which suggest that the surface concentration of Pd is reduced to ~ 18% upon annealing a 5 ML Pd-5ML Au/Mo(110) surface at 800 K for 20 minutes.

TPD is an excellent surface science tool to characterize the surface adsorption sites and hence, CO TPD was performed on Pd-Au/Mo(110), as well as on Pd/Mo(110) [145,157]. On the 5ML Pd- 5ML Au/(110) alloy surface, two distinct TPD peaks are observed at about 100 and 300 K (see Fig. 53) corresponding to CO atop adsorption on Au and Pd, respectively. On Pd/Mo(110) surface features between 400 and 500 K corresponding to CO adsorbed on the bridge and tri-hollow sites were visible. Since a desorption feature of CO above 350 K on the Pd-Au surface was not observed, there are no multi-fold Pd adsorption sites on the surface. This assumption is consistent with IRAS (Fig. 52) and LEISS (Fig. 50) results which indicate that all surface Pd atoms were isolated by Au atoms forming Pd monomer, $PdAu_6$.

VA Reaction Rate Measurements on Pd/Au(100) and Pd/Au(111)

VA synthesis was performed using Pd/Au(100) and Pd/Au(111) catalysts at 453 K to understand the promotional effect of Au. The catalysts were prepared by physical vapor deposition of Pd on clean single crystals followed by annealing to 550 K. As mentioned earlier, the formation of isolated Pd monomers for Pd/Au(100) and Pd/Au(111) were confirmed by IRAS and CO probe molecule. STM results have also confirmed the formation of surface Pd monomers on Au(111) [153]. After annealing to 500 K a considerable decrease in the surface Pd coverage on Au(111) was observed using LEISS [151]. Ideally, the availability of the isolated Pd monomers should occur at 1/2 ML Pd on Au(100) and at 1/3 ML Pd on Au(111),

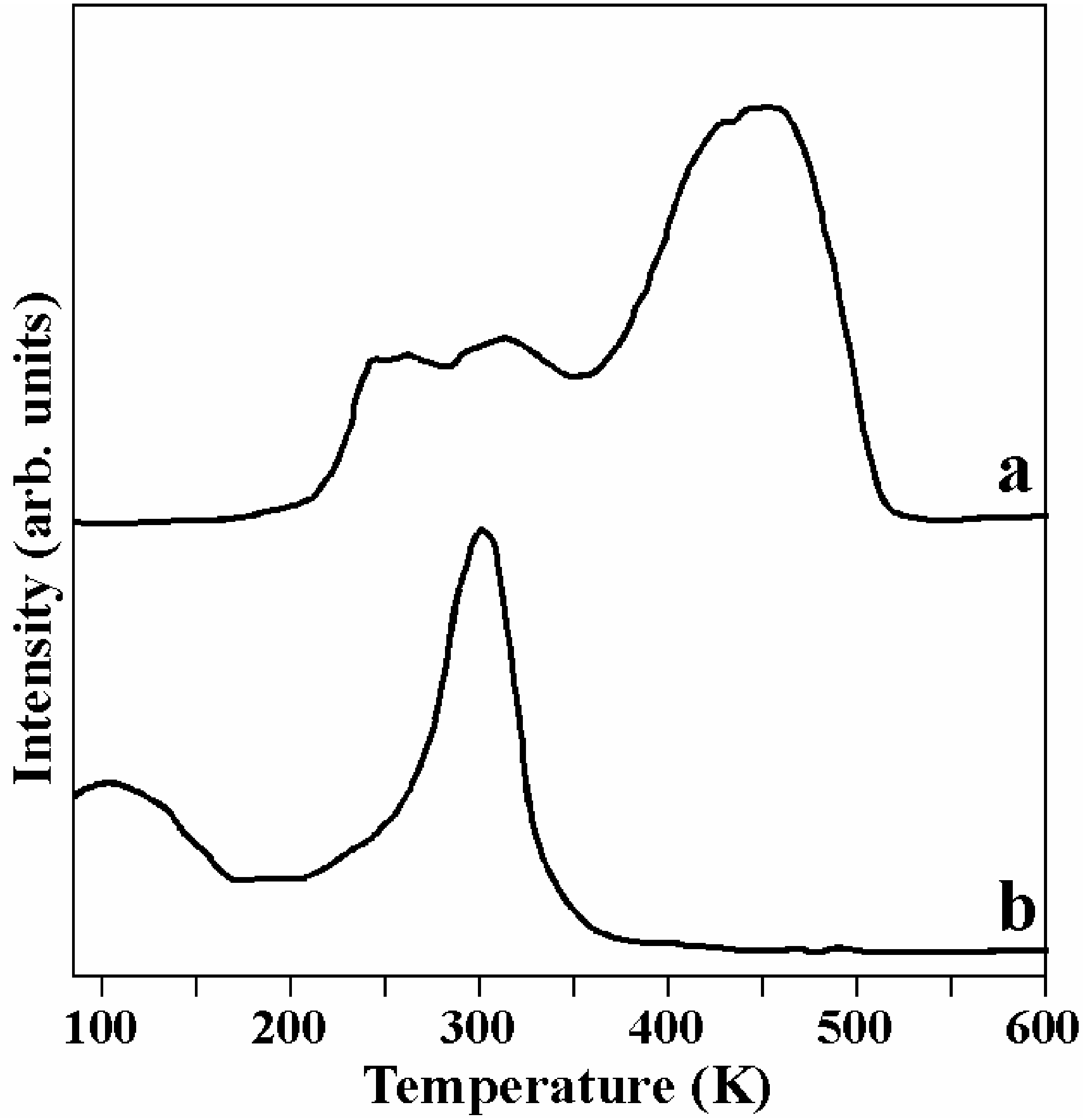

Fig. 53. TPD of CO on: a) 10 ML Pd/Mo(110) and b) 5 ML Pd/5 ML Au/Mo(110) annealed to 800 K for 20 minutes [145].

coverages that correspond to the Au(100)-c(2 x 2)-Pd and Au(111)-(√3 x √3)R30°-Pd structures, respectively [154]. However, since Pd and Au are completely miscible over the entire range of compositions such well-ordered surface structures were not observed. Another reason is that Au has much lower surface energy, and hence, segregates to the surface [128].

The surface coverage of Pd deposited on Au(100) or Au(111) following an anneal increases constantly with increasing Pd coverage. If each surface Pd atom is an active site for VA synthesis, then the activity of VA formation should increase continuously with an increase in the Pd coverage. For example, using CO oxidation experiments ($CO:O_2$ = 2:1, Total pressure = 5.0 Torr) CO_2 formation rate was measured as a function of the Pd coverage on Au(111). The reaction was carried out at 523 K with the total reaction time of 2 hours. As illustrated in Fig. 54, a steady increase in the CO_2 formation rate is observed with the increasing surface Pd coverage on Au(111) surface. This surface is essentially the same as the surface used for VA synthesis and the data shows that isolated Pd monomers have similar activity for CO oxidation as contiguous Pd sites. This is clear from calculation of CO_2 formation rate on a per Pd basis where an almost flat line is visible for any coverage of Pd on Au(111). However, for VA synthesis on Pd/Au(100) and Pd/Au(111) as shown in Fig. 55, the VA TOF does not increase linearly with an increase in the coverage of Pd. Instead VA TOF increases with an increase in the Pd coverage from 0 - 0.1 ML followed by a gradual decline in the rate from 0.1 - 1 .0 ML, equaling the rate observed for Pd(100) at 1.0 ML.

Identification and Properties of the Active Site

The trend portrayed by these results strongly allude to the fact that isolated Pd sites or monomers act as catalytically active sites on Au(100) and Au(111) for VA synthesis. Also, as depicted in

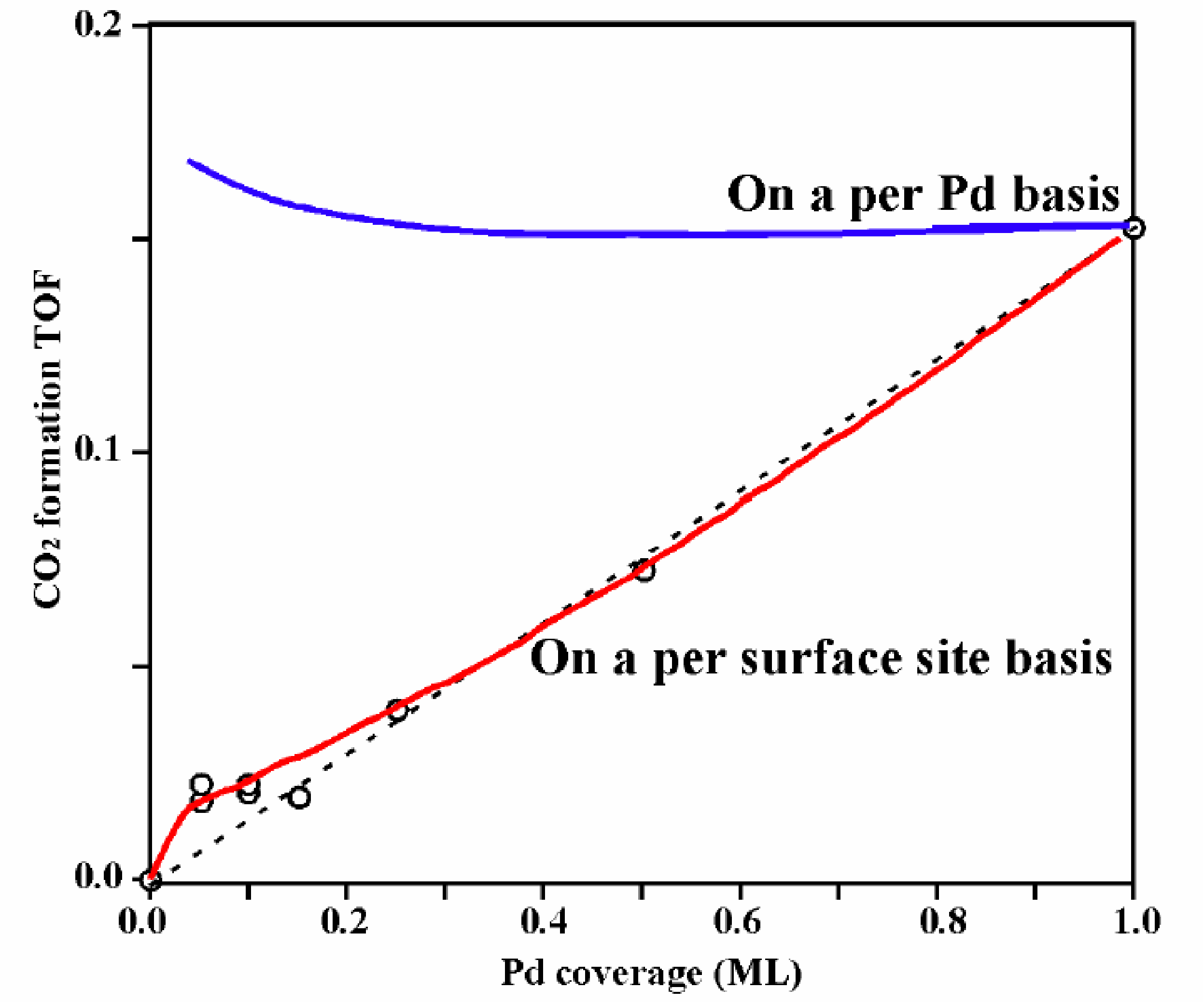

Fig. 54. CO_2 formation rates as a function of Pd coverage on Au(111). CO:O_2 = 2:1, with total pressure of 5 Torr. The reaction was carried out at 523 K with a total reaction time of two hours. The data show that isolated Pd monomers have similar activity for CO oxidation at contiguous Pd sites.

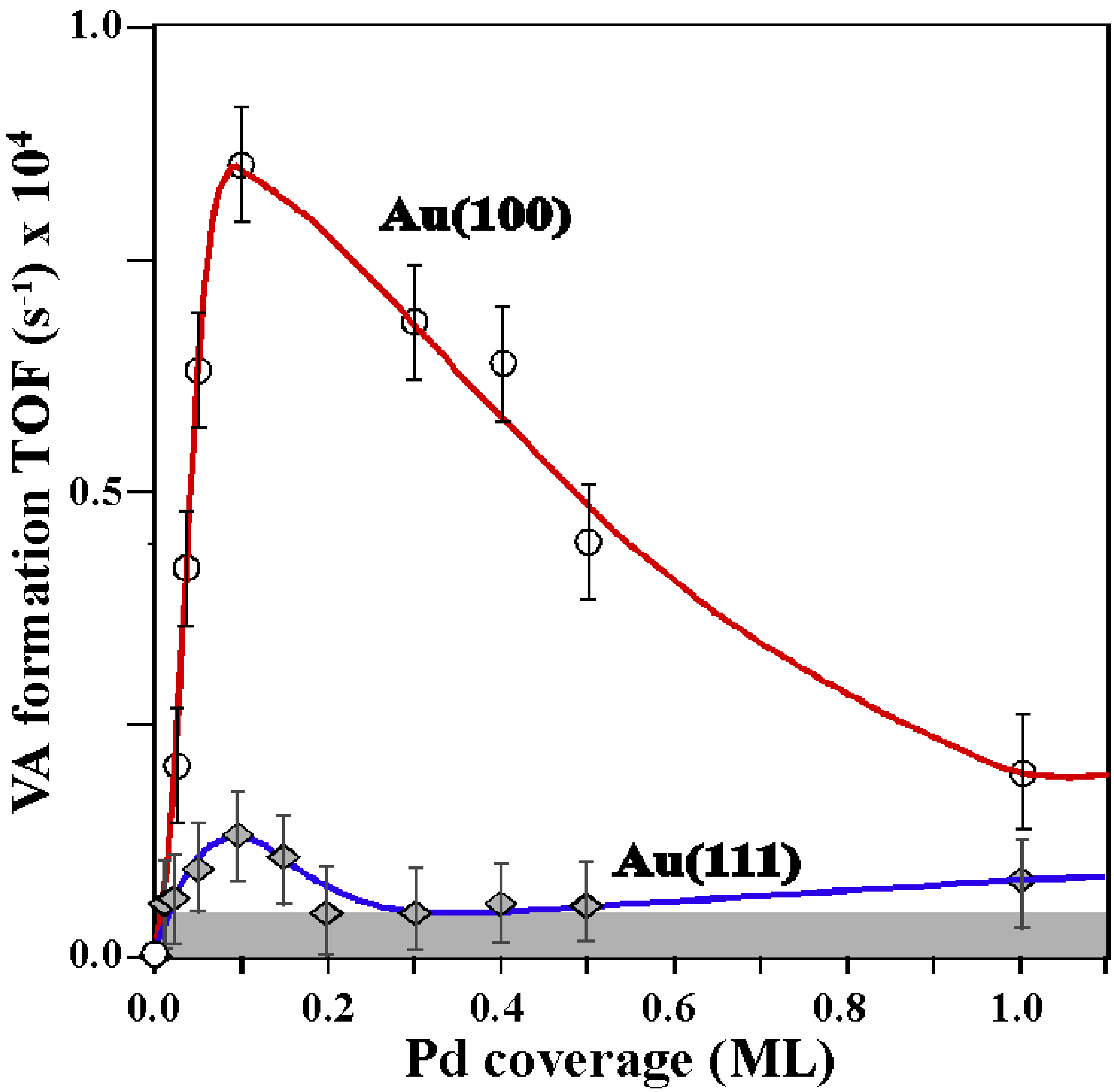

Fig. 55. VA formation rates as a function of Pd coverage. The TOF's are computed with respect to the (1 x 1) surface unit. The VA synthesis was carried out at 453 K for 3 hours, with acetic acid, ethylene and O_2 pressures of 4, 8 and 2 Torr, respectively. The error bars are based on background rate data.

Fig. 56, using a simulation to calculate the number of surface Pd monomers as a function of Pd coverage on Au(100) surface shows that the maximum density is achieved at the Pd coverage of about 0.1 ML. It should be noted that during VA synthesis the subsurface Pd could be extracted onto the surface under the influence of the reactants as is evident from out XPS and LEISS results [158].

VA synthesis rate on Au-only surface is insignificant compared to the Pd-only surface. Hence, it would be ideal to illustrate the VA reaction rate for the Pd-Au alloy catalysts with respect to the atomic fraction of Pd on the surface, as shown in Fig. 57. The formation rate per Pd on Au(100) surface was observed to be varying with the amount of Pd on the surface with the maximum in the activity occurring at a coverage of 0.07 ML. While there is a decrease in the reaction rate with the increase or decrease of the amount of Pd on Au(100), markedly different behavior is exhibited by Pd deposited on Au(111). A continuous increase in the reaction rate is observed with the decrease in the amount of Pd on the surface of Au(111). These data for VA formation rate on Pd on Au(100) and Au(111) surfaces indicate that the isolated Pd atoms are the active sites for the reaction. The apparent difference in the per Pd reaction rates for Au(100) and Au(111) surfaces also indicate that pair of non-contiguous Pd monomer sites are needed to form VA. Again using a simulation, the number of surface Pd monomer pairs as a function of Pd coverage on Au(100) was evaluated and as illustrated in Fig. 58, a maximum density of surface Pd monomer pairs is available at a coverage of about 0.1 ML of Pd.

For Pd/Au(111) the steady increase in the VA rate (see Fig. 57) with decreasing Pd coverage is indicates that isolated Pd atoms are the active sites. But, the VA formation rate on Pd/Au(100) is not similar to Pd/Au(111) and a sharp maximum is seen at a Pd coverage of ~0.07 ML. This implies that a pair of non-contiguous Pd sites, i.e., a pair of Pd monomers (see inset in

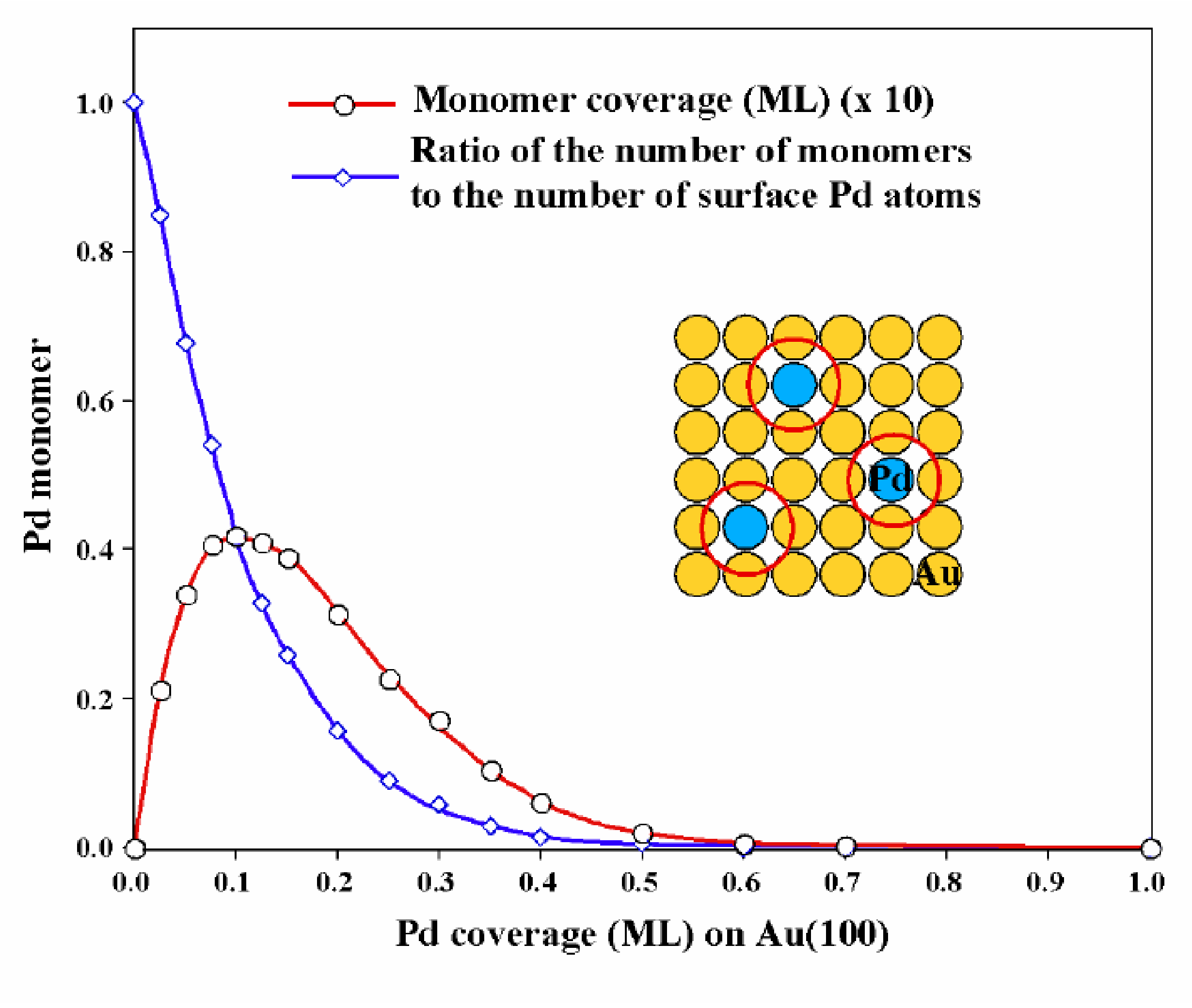

Fig. 56. Simulation of the number of surface Pd monomers as a function of Pd coverage on Au(100) surface. The data were simulated by Z. Dohnalek at Pacific Northwest National Laboratories, USA.

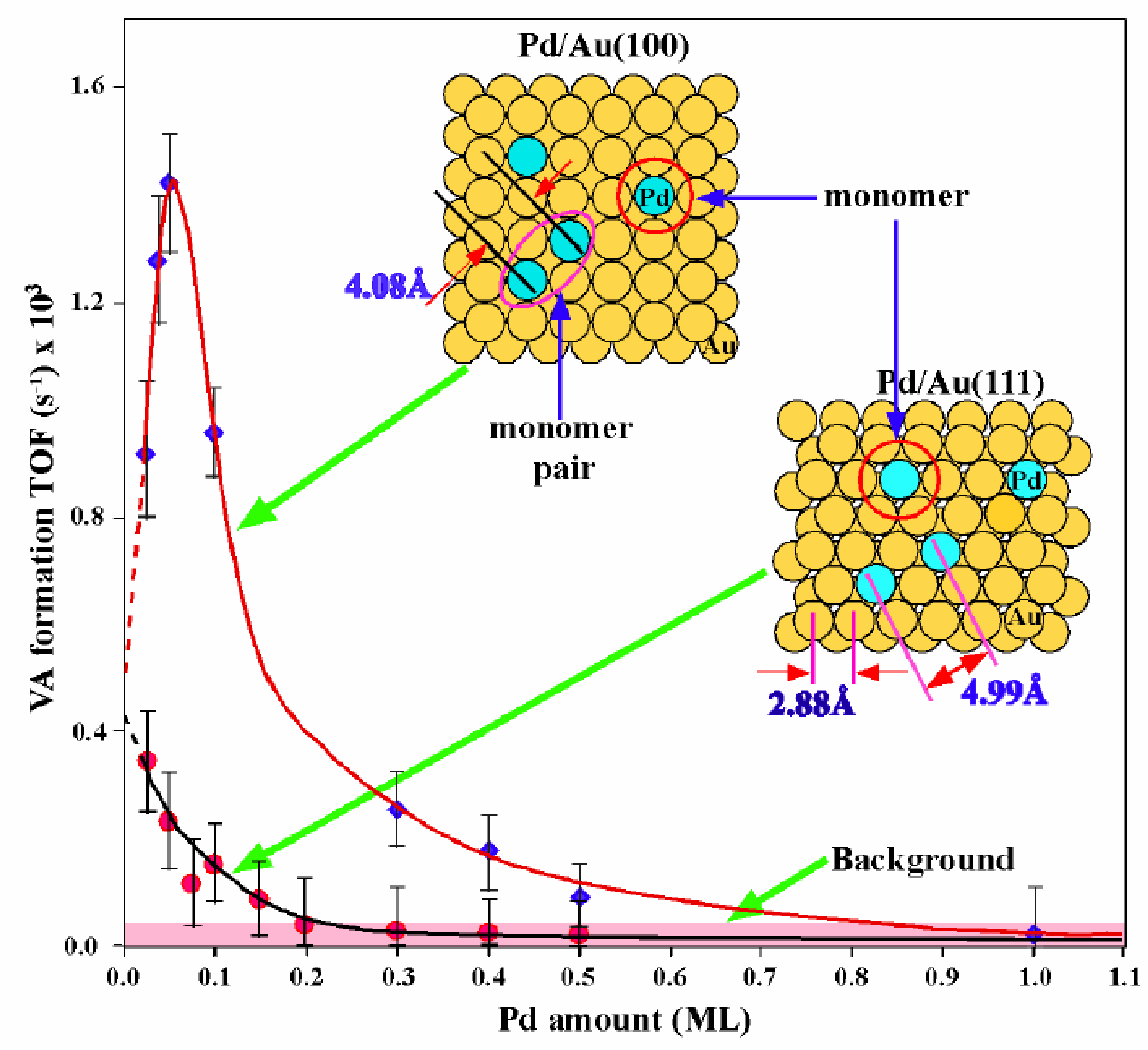

Fig. 57. VA formation rates as a function of Pd coverage. The TOFs are computed with respect to the Pd atom concentration. Pd was deposited on the respective surface at 300 K and annealed to 600 K for 10 min. C_2H_4 = 8 Torr, O_2 = 2 Torr, CH_3COOH = 4 Torr, reaction temperature = 453 K, reaction time = 3 hrs. The error bars are based on background rate data. The inserts show Pd monomers and monomer pairs on the Au(100) and Au(111).

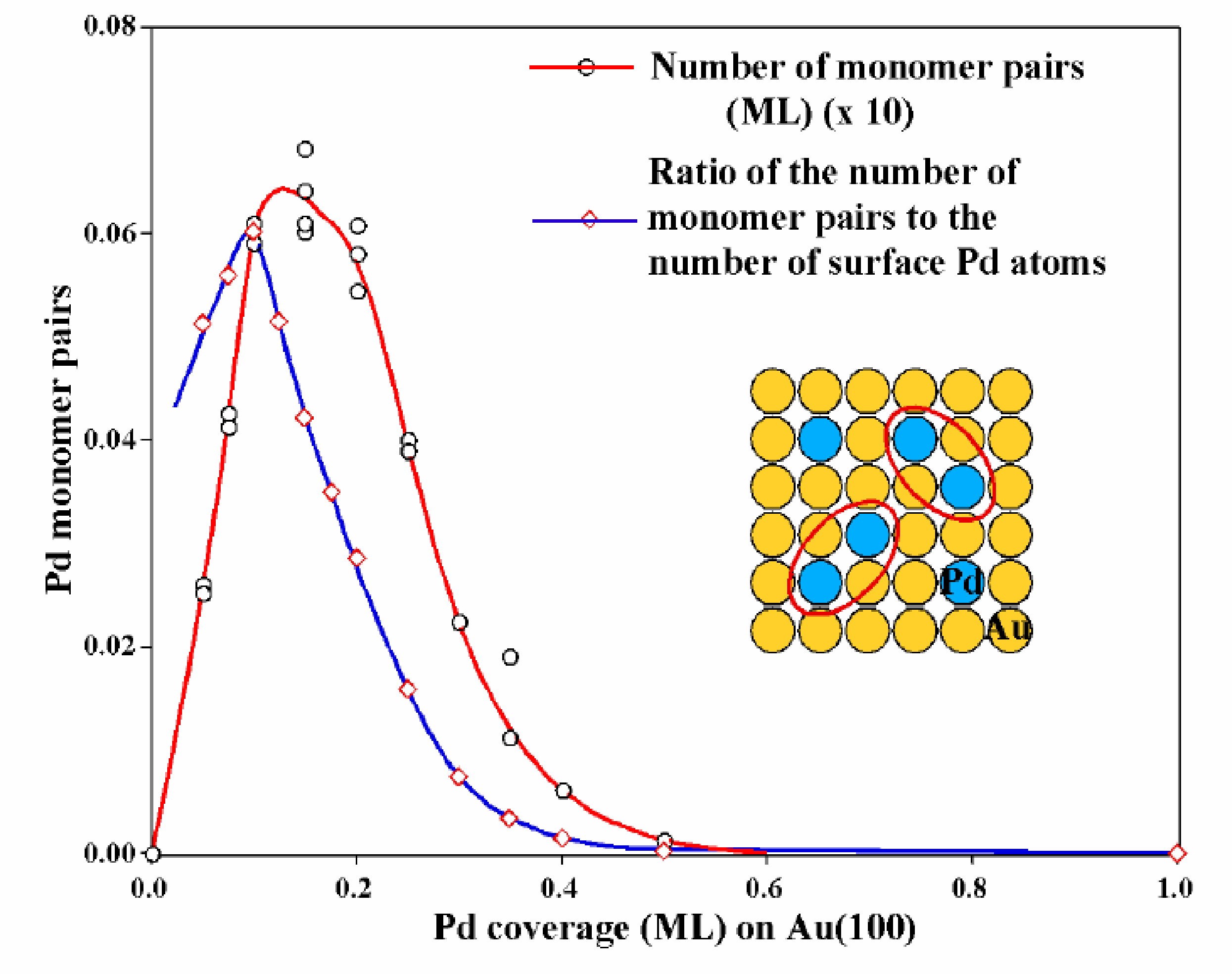

Fig. 58. Simulation of the number of surface Pd monomer pairs as a function of Pd coverage on Au(100) surface. The Pd monomer pairs are encircled by red ellipses in the insert. The data were simulated by Z. Dohnalek at Pacific Northwest National Laboratories, USA.

Fig. 57) is needed for the formation of VA and is more effective than a single isolated Pd site.

Another apparent difference between the reaction rates on Pd/Au(100) and Pd/Au(111) is that the reaction rate on the former is much higher than on the later catalyst. The reason for such obvious difference is explained by understanding the reaction mechanism for VA synthesis where two pathways have been proposed in the literature: (i) adsorption and subsequent activation of ethylene to form a vinyl species which couples with a coadsorbed acetate species to form VA [81]; and (ii) adsorbed ethylene reacts with an adsorbed acetate nucleophile to form an ethyl-acetate-like intermediate which then undergoes a β-H elimination to form VA [63]. The hydrogen removes hydrogen to form water. There are differences between the above mechanism, but they both assume the coupling of surface ethylene species and acetate to form VA is the rate-limiting step [63,68,81]. Recently Tysoe's group found evidence to indicate that insertion of ethylene into an adsorbed acetate species and subsequent β-H elimination to form VA is the rate limiting step [159].

The presence of bidentate acetate species and the π bonding of ethylene on the Pd monomers was evidenced by HREEL spectroscopy (see Fig. 59 left panel). On both the surfaces, with only isolated Pd monomer sites and the surface with continuous Pd sites, the appearance of loss peaks at about 1420 and 2950 cm^{-1} and the absence of a peak at 1700 cm^{-1} clearly imply the presence of a bidentate acetate species. However, on isolated Pd monomer sites only π bonding of ethylene species was observed (see Fig. 59 right panel), whereas di-σ bonding ethylene and ethylidyne species were found on the surface with continuous Pd sites.

Using bond lengths of the acetate and ethylene species adsorbed on two Pd monomer sites in the above described fashion, the optimum spacing between the two Pd active sites to couple to form VA is approximately 0.33 nm as depicted in Fig. 60. The spacing between two neighboring Pd monomers is 0.408 nm on Pd/Au(100) surface. However, on the Au(111) surface, the nearest distance between two neighboring Pd monomers is 0.50 nm. Hence, it is apparent that for Pd on Au(111) yields a much larger distance than the ideal 0.33 nm distance and produces much less VA compared to Pd/Au(100). On the contrary, using density function theory (DFT) calculations larger Pd ensembles have been professed to be necessary for the formation of VA [160]. Our research shows that larger Pd ensembles are not required for efficient formation of VA.

The addition of a second metal component to a catalytically active metal system causes severe changes in the electronic and chemical properties. There are two most commonly and widely accepted mechanisms to explain the changes in terms of geometric and electronic properties. In general, for the adsorption of a reactant, product or an intermediate requires a certain number of atoms in a particular geometry. The chemical properties of the species are thus governed by the coordination and geometry of the two metal atoms in a bimetallic system. This effect is termed as ensemble effect or geometric effect. Electronic effect or ligand effect is related to the electronic influence of one metal atom on the neighboring metal atoms to affect the chemical and physical properties.

In case of bimetallic Pd-Au catalysts, the significantly higher VA formation rate at Pd monomer sites can be explained either by alloying (electronic), strain, and/or ensemble effects. For a Pd-Au alloy, there is only a 4% lattice mismatch between a relaxed Pd overlayer and a Au(100) or Au(111) surface leading to a minimal lattice strain. Furthermore, the work functions for Au and Pd are very similar (5.3 versus 5.6 eV, respectively) and the electronegativities are identical (1.4). Limited charge transfer is observed between Pd and Au in Pd-Au alloys using XPS core-level studies [151]. Hence, it is safe to conclude that there is very little electronic and

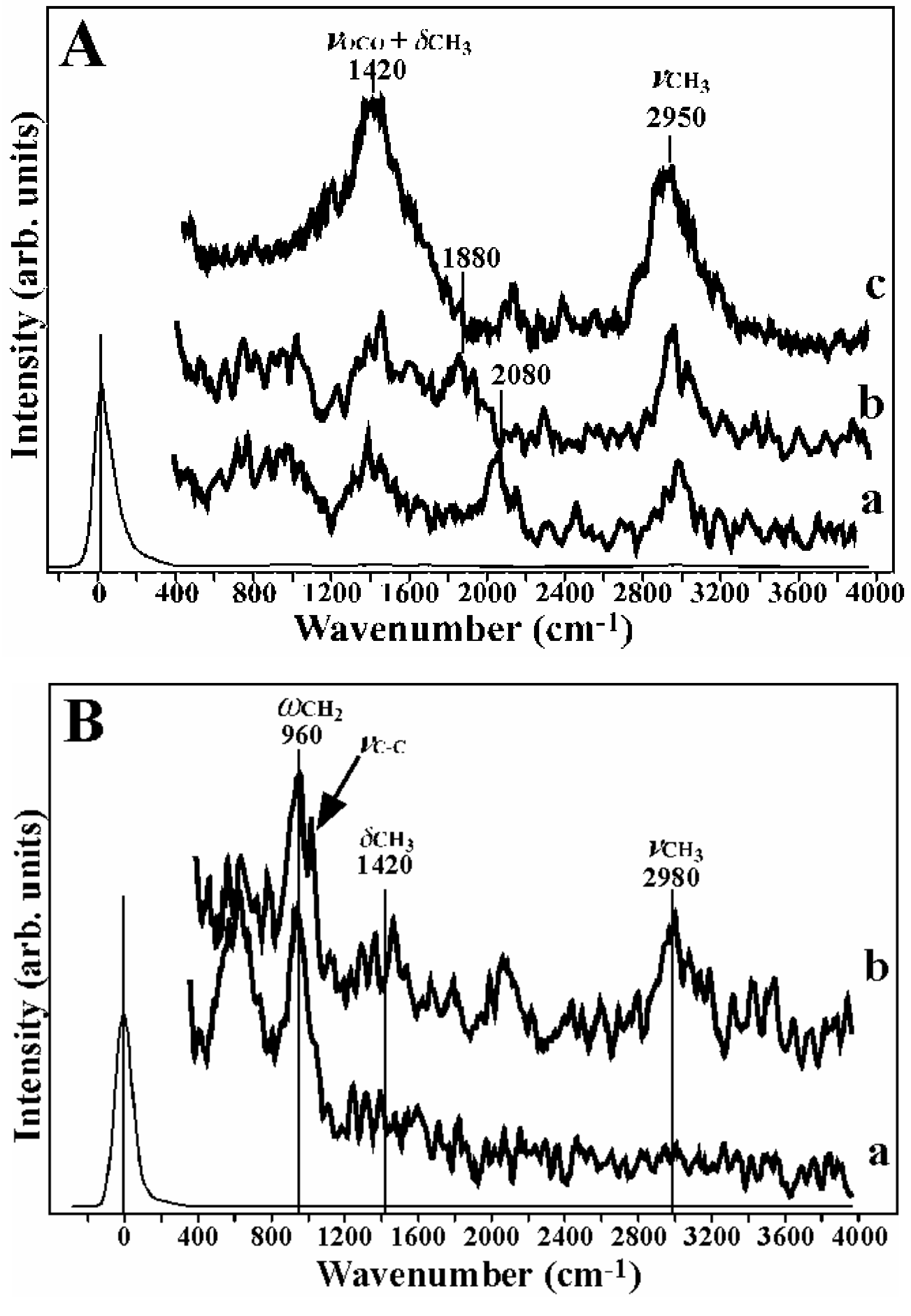

Fig. 59. HREELS spectra of : (A) Acetic acid adsorption on a) Pd/Au(111) with only isolated Pd sites, b) Pd/Au(111) with continuous Pd sites, and c) 1 ML Pd/Au(111) after VA synthesis reaction for 3 h. (B) Ethylene adsorption on a) Pd/Au(111) with only isolated Pd sites, and b) Pd/Au(111) with continuous Pd sites. Acetic acid was dosed into the chamber with a background pressure of 2 x 10^{-8} Torr and cooling the sample from 350 K to 210 K. Ethylene was dosed into the chamber with a background pressure of 2 x 10^{-8} Torr and cooling the sample from 300 K to 170 K.

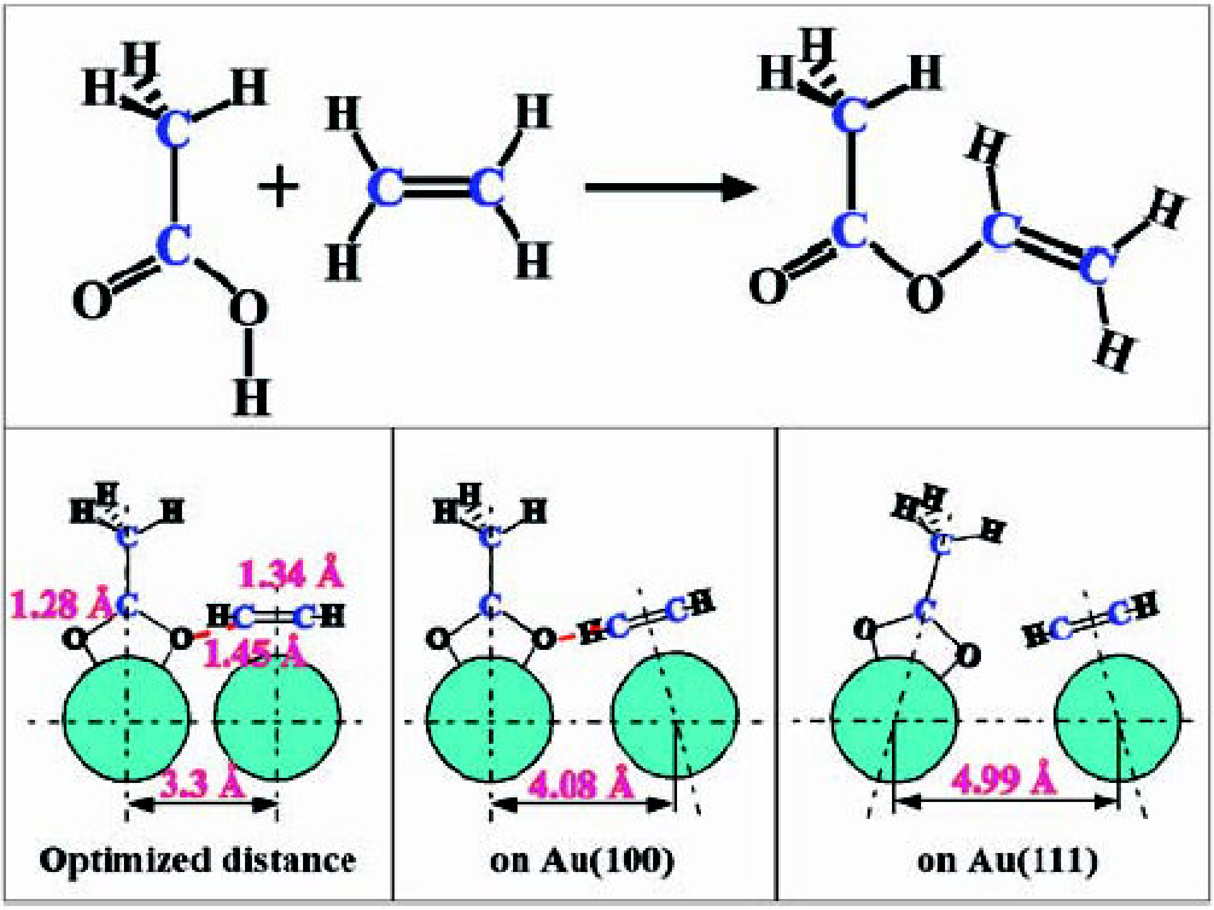

Fig. 60. Schematic for VA synthesis from acetic acid and ethylene. The optimized distance between the two active centers for the coupling of surface ethylene and acetate species to form VA is 3.3 Å. With lateral displacement, coupling of an ethylene and acetate species on a Pd monomer pair is possible on the Au(100), but unlikely on the Au(111).

strain effects in case of Pd-Au alloy catalysts. The exceptionally high activity of a Pd monomer for VA synthesis can be explained using the geometric/ensemble effects.

Among other things, it was observed that the formation of Pd monomers inhibits the formation of undesirable byproducts, e.g. CO, CO_2 and surface carbon. As shown in Fig. 53, CO TPD peak position for CO on a Pd-Au surface is much lower than that from a Pd surface. Since, CO is an intermediate or a by-product in the VA reaction, the strong adsorption of CO on the continuous Pd sites may poison the surface active sites thus decrease the activity as demonstrated earlier using heterogeneous Pd-Au/SiO_2 catalyst. Also, the adsorption of ethylene was also different on Pd-Au and Pd-only surfaces. As shown in Fig. 61, ethylene was found to bind significantly less strongly on an isolated Pd site compared to contiguous Pd sites. Moreover there is a difference in the surface species observed on these two surfaces. The di-σ bonding ethylene and ethylidyne species are formed on the surface with continuous Pd sites. These species may further decompose into carbon containing species on the surface, and thus, block and poison the surface active sites. Hence, it is concluded that the addition of Au to Pd significantly suppresses carbon deposition.

Planar Pd-Sn Catalysts

Similar to the Pd-Au system, Pd-Sn system would be ideal for the formation of these active sites which are isolated Pd monomers separated by a specific distance due to two reasons. Firstly, the distance between the Pd monomers provided by Sn-Pd system is 3.89 Å which close to the ideal distance of 3.3 Å required for the coupling of surface acetate and ethylene species to form VA, as represented in Fig. 62. Secondly, the number of such Pd monomer pairs is expected to be more on Pd-Sn system as compared to Pd-Au system due to the formation of ordered

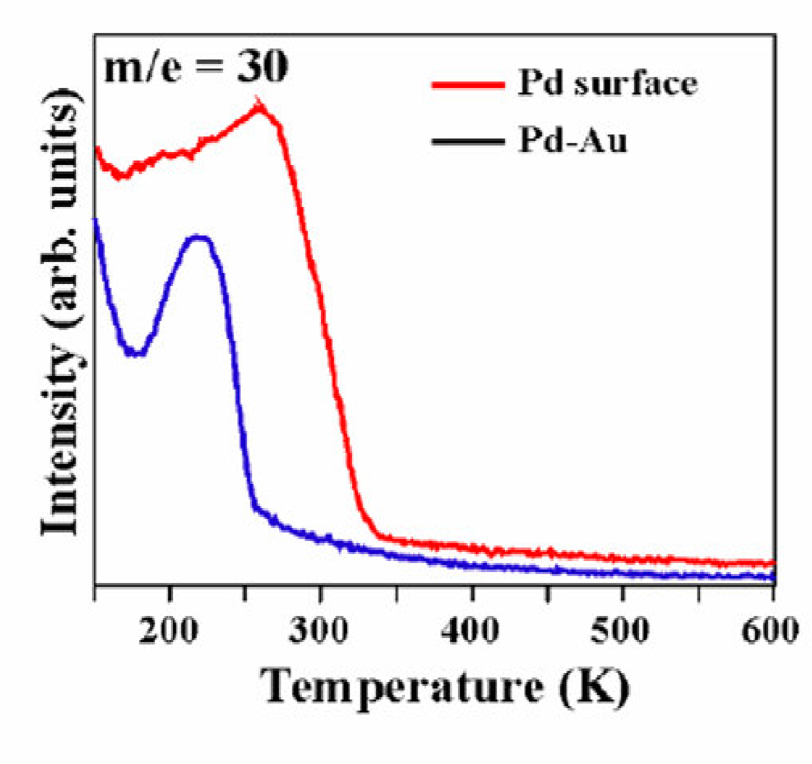

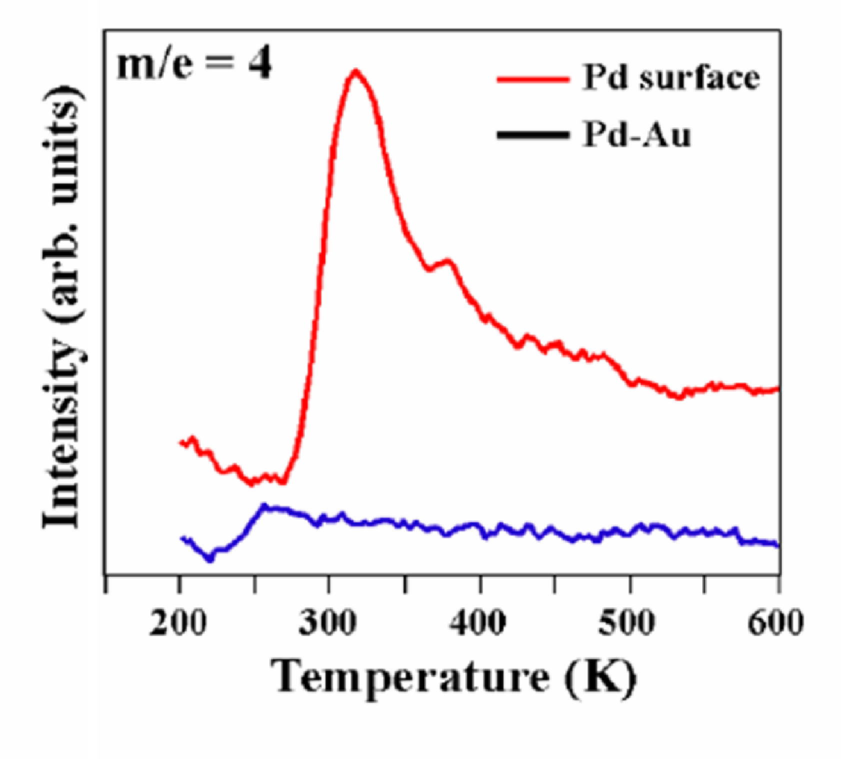

Fig. 61. TPD of ethylene (C_2D_4) from supported Pd and Pd-Au alloy clusters [144].

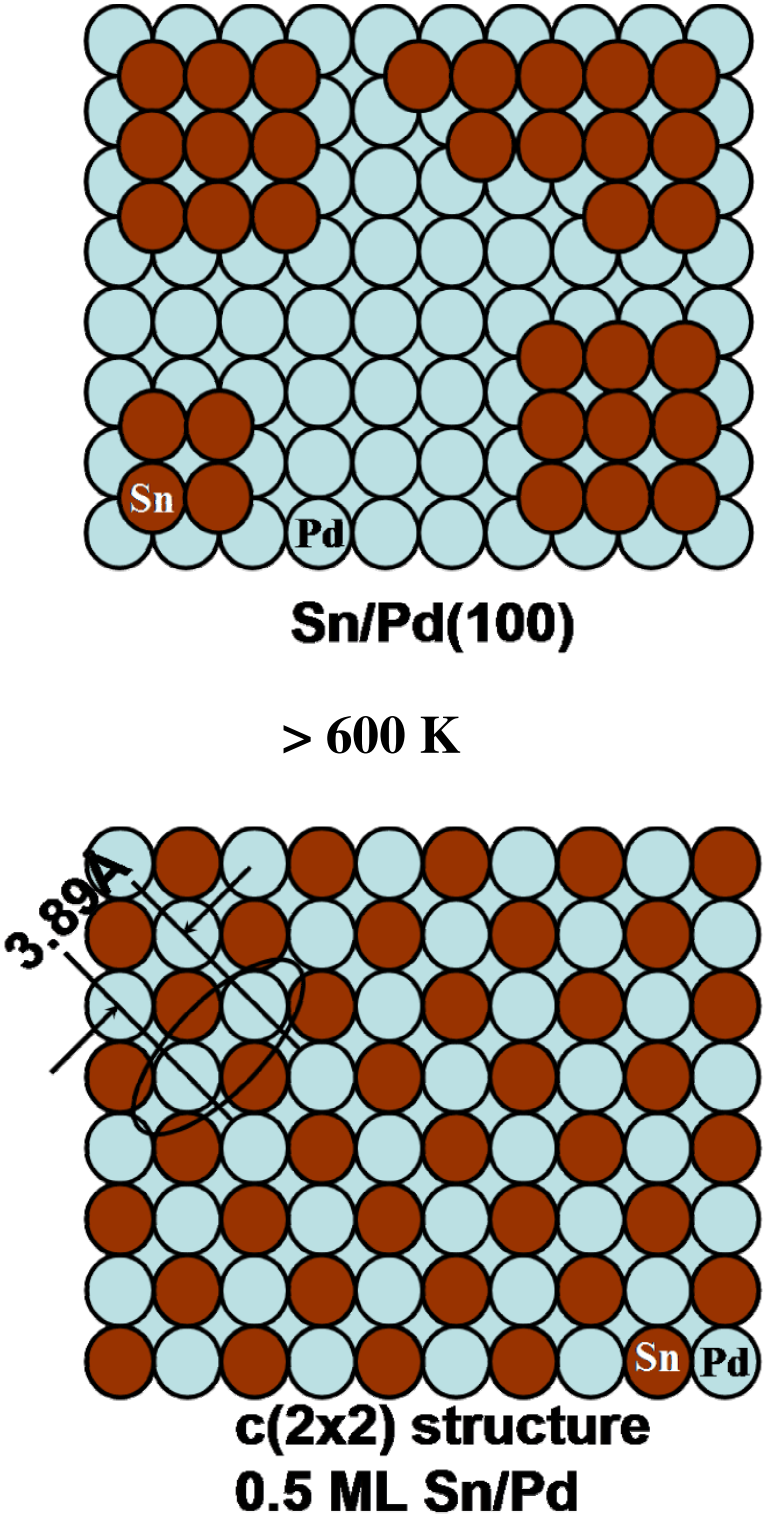

Fig. 62. Schematic depicting the changes in the surface coverage leading to the formation of a c(2 x 2) structure with the surface coverage of both Sn and Pd at 0.5 ML due to annealing the Sn/Pd(100) surfaces to temperatures higher than 600 K. The distance between two Pd atoms on the surface is 3.89 Å as illustrated in the diagram.

surface structures. In the present section we report the synthesis of VA on Pd-Sn system. Research groups of Lambert, Koel and others have studied the deposition of Sn on Pd, Pt and other surfaces [161-165]. Acetylene chemisorption on Sn covered Pd(111), Sn/Pt(100) and Pt(111) to form benzene and other C_4 and C_6 products has been studied and it has been proposed that deposition of Sn on Pt(100) and annealing produces c(2 x 2) Pt-Sn alloy structure with Sn coverage at 0.5 ML [166].

Epitaxial growth of metals on other refractive metal surfaces is a common practice in surface science to simulate the catalytic properties of thin films and nanoclusters. Pd and Sn are known to follow a layer-by-layer growth pattern on many metal substrates [161,162]. Pd was evaporated onto the Rh(100) surface at room temperature in vacuum. The coverage of Pd is estimated from the break point in a plot of Pd/Rh XPS area ratio versus the Pd deposition time as shown in Fig. 63 A. Similarly, Sn doser was calibrated by deposition on Rh(100) single crystal (see Fig. 63 B). A break point was evident at about 25 min of dosing.

VA Reaction Rate Measurements on Pd-Sn/Rh(100)

While no VA formation was observed with Rh(100) and Sn/Rh(100), a stable value of about 1 x 10^{-5} s^{-1} was observed after 3 hours of reaction for 4.0 ML of Pd/Rh(100) annealed to 600 K for 1.0 min which is less than that noted on Pd(100) catalyst [84]. The apparent difference might be due to the coverage; that is, when the deposited Pd is a few monolayers thick, the electronic effect of the substrate Rh(100) might be significant. After confirming that the reaction rate on Pd/Rh(100) is stable, different amounts of Sn was vapor deposited on to this film of Pd and annealed to 600 K for 1.0 min. VA reaction was carried out on this surface for 3.0 hrs and a maximum rate was recorded after depositing about 0.25 ML of Sn as can be seen in Fig. 64.

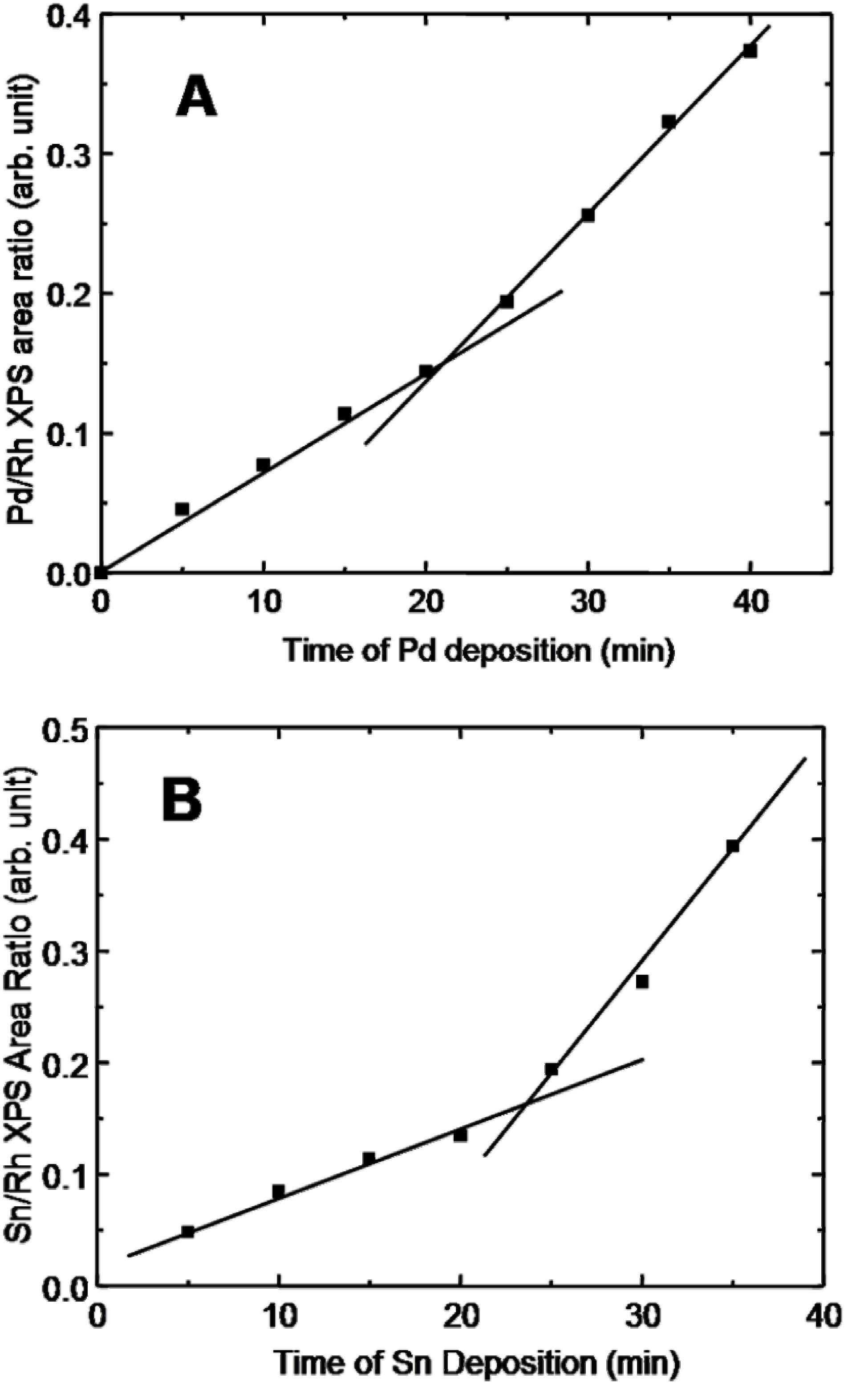

Fig. 63. (A) Calibration of Pd doser on Rh(100) at 300 K. (B) Calibration of Sn doser on Pd(100) at 300 K.

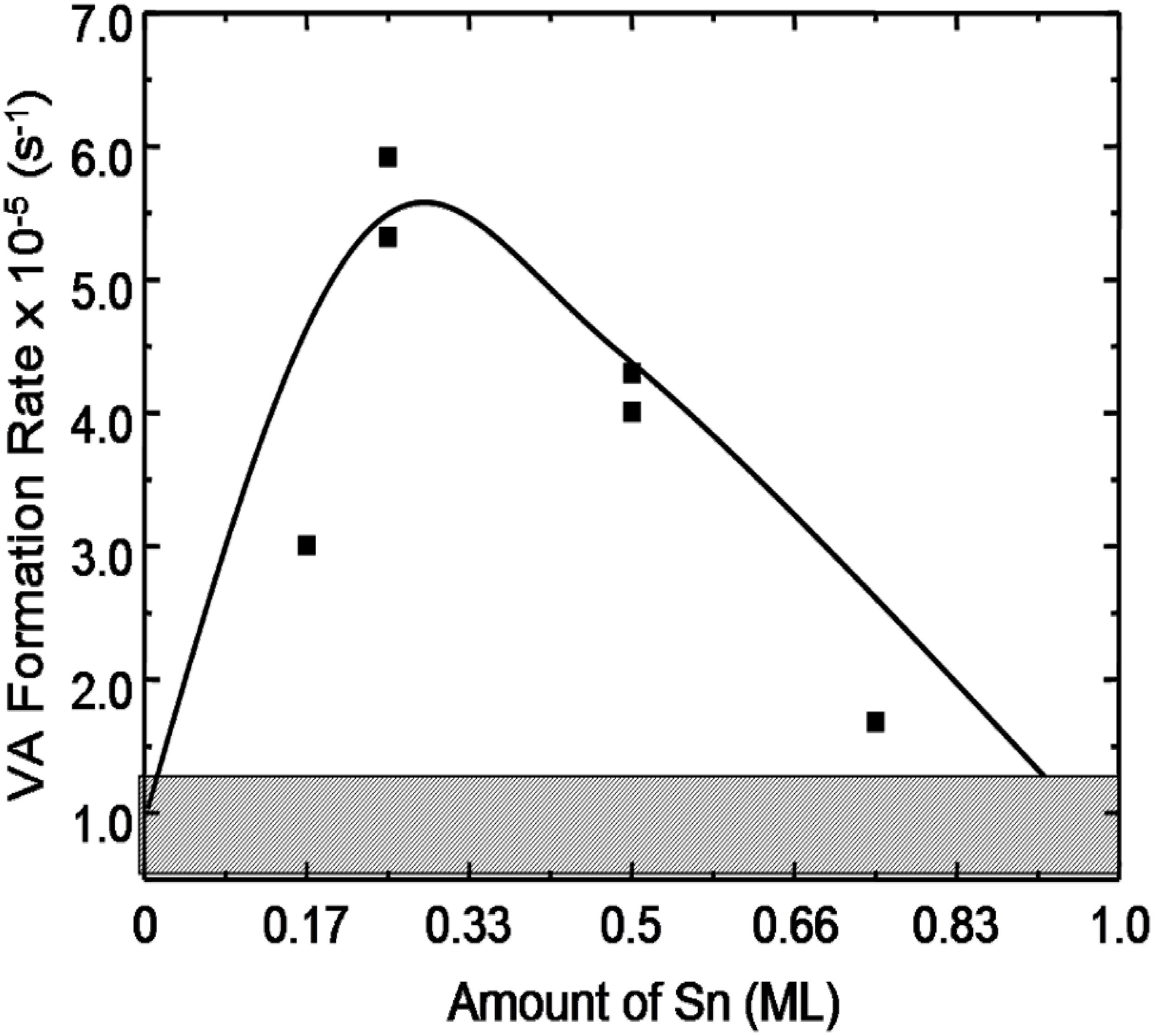

Fig. 64. VA formation rate on Sn/4.0 ML Pd/Rh(100) system annealed to 600 K for 60 sec at different coverages of Sn. Reaction at 450 K; p_{O_2} = 2.0 Torr; $p_{C_2H_4}$ = 9.0 Torr; p_{AcOH} = 4.0 Torr; Time = 3 hrs.

Further increase in the Sn dosage leads to some reduction in the VA formation rate.

Due to the fact that only Pd is active for the synthesis of VA, the VA formation rate is expressed per Pd as shown in Fig. 65. Thus, the maximum VA formation rate per Pd is observed at a coverage of 0.5 ML of Sn on Pd. This maximum activity is significantly higher as compared to Pd-alone on Rh(100). This procedure of depositing and annealing Sn/Pd systems is an established recipe for the production of c(2 x 2) Pd-Sn structures [161,167]. The formation similar structure upon deposition of Sn on Pd(100) was observed using low energy electron diffraction (LEED). The formation of a similar c(2 x 2) geometry was also supported by Koel and Lambert groups on Pd(111), Pd(110), Pt(111) and Pt(100) surfaces [161-165]. The total density of Pd monomer pairs is maximum at this coverage and the distance between each isolated Pd monomer is 3.89 Å. In fact, after the formation of c(2 x 2) structure, ideally the distance between any two contiguous Pd atoms should be the same. Since it has been proposed that a pair of such Pd monomers separated by an ideal distance of 3.3 Å act as the active sites [155], the VA formation rate should be maximum at the coverage when c(2 x 2) structure is formed. Hence, the data represents that isolated Pd sites as active sites for the adsorption of acetate and ethylene species and by the coupling of these species VA is formed.

With further increase in Sn coverage the VA formation rate decreases slightly which might be due to the decrease in the Pd monomer density due to the formation of Sn islands on the surface of the catalyst. Excess Sn that may diffuse into the subsurface of Pd or form Sn overlayer may influence the adsorption and reaction of the neighboring Pd atoms and result in the decrease of the overall activity. Tsud et al. [162] have reported the formation of a c(2 x 2) LEED pattern after the deposition of 0.5 ML Sn on Pd(110) which changed to a (3 x 1) pattern at a coverage of 0.75 ML. With further increase in the coverage the dissolution of Sn into

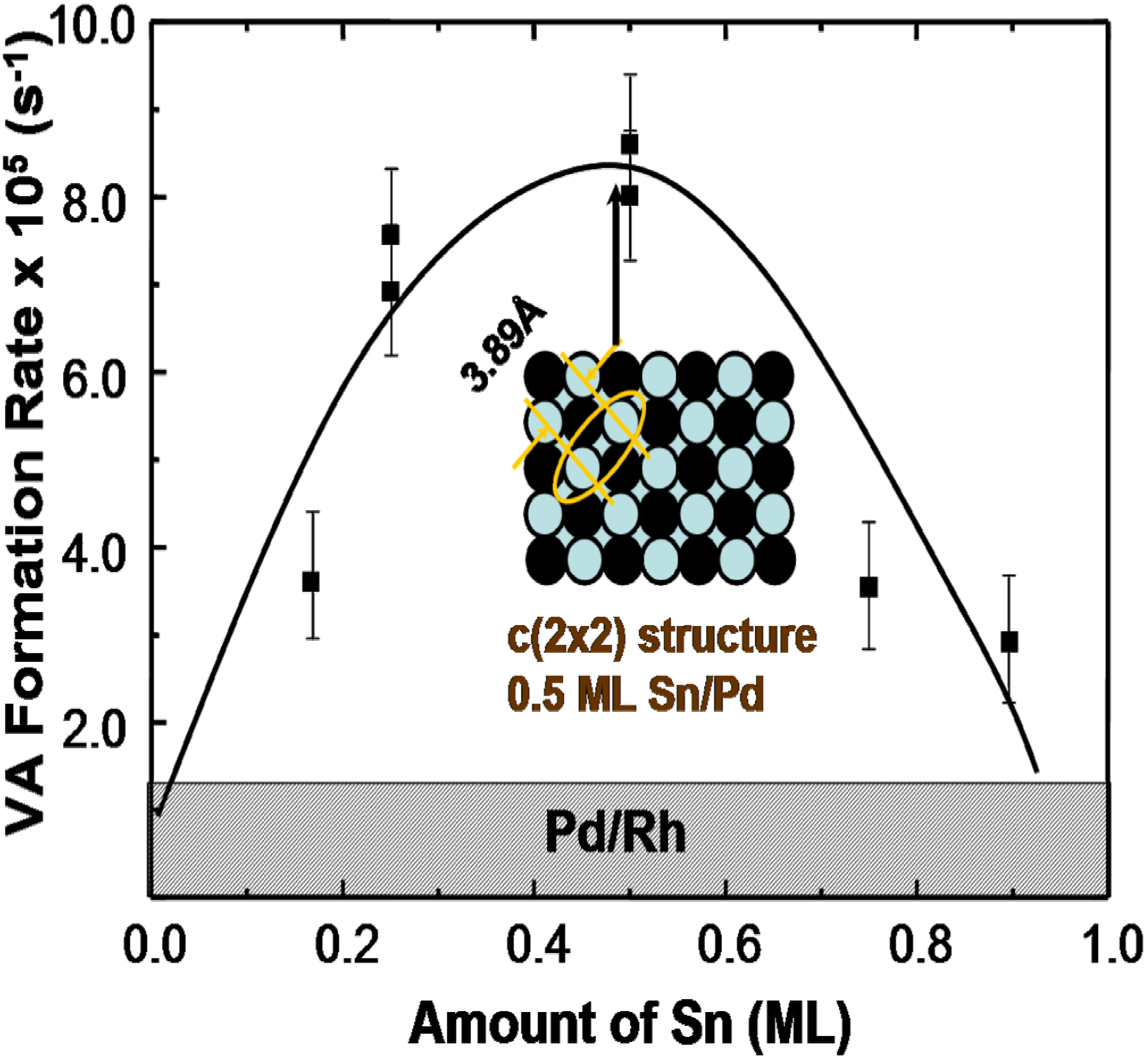

Fig. 65. VA formation rate normalized to per Pd site basis on Sn/ 4.0 ML Pd/Rh(100) annealed to 600 K for 60 sec. Reaction at 450 K; $p_{O_2} = 2.0$ Torr; $p_{C_2H_4} = 9.0$ Torr; $p_{AcOH} = 4.0$ Torr; Time=3 hours.

subsurface layer was noted forming Pd-Sn intermetallic alloys with different stoichiometry. CO adsorption of these surfaces further confirmed the formation of these LEED structures on the surface. Furthermore, the adsorption properties of the surfaces with respect to CO were noted to be dependent on the amount of Sn deposited on Pd(110). The subsurface layer Pd-Sn intermetallic compound affects the adsorption of CO. The formation of this subsurface alloy of Pd-Sn is more probable with the increasing amounts of Sn and hence correspondingly the amount of CO adsorbed decreases. XPS studies using synchrotron radiation were utilized to observe a strong chemical interaction between Sn and Pd. Significant shift in the Pd 3d and Sn 4d core levels and the valence band spectra were observed. The strong interaction between Sn and Pd was also investigated in our laboratory using XPS on Sn/Pd(100) [168].

Catalyst Deactivation

The VA synthesis reaction in our experiments is typically carried out for 3 hrs. Since we noted a significant reduction in the reaction rate, we have investigated the initial activity during formation of VA on Pd-Sn system. Fig. 65 is VA formation rate as a function of time for 0.5 ML coverage of Sn at which a highest density of Pd isolated monomers is expected. The activity of the catalyst system indeed decreases very fast as the reaction proceeds. After 10.0 hrs of reaction time the activity of the catalyst is in fact much less than Pd-alone system. The initial activity is obtained by extrapolating the formation rate curve to zero time which is about 5×10^{-4} s^{-1}. The initial rate on Pd-Sn is at least 10 times higher than Pd-alone system which on the other hand does not show any significant decrease after the same amount of reaction time.

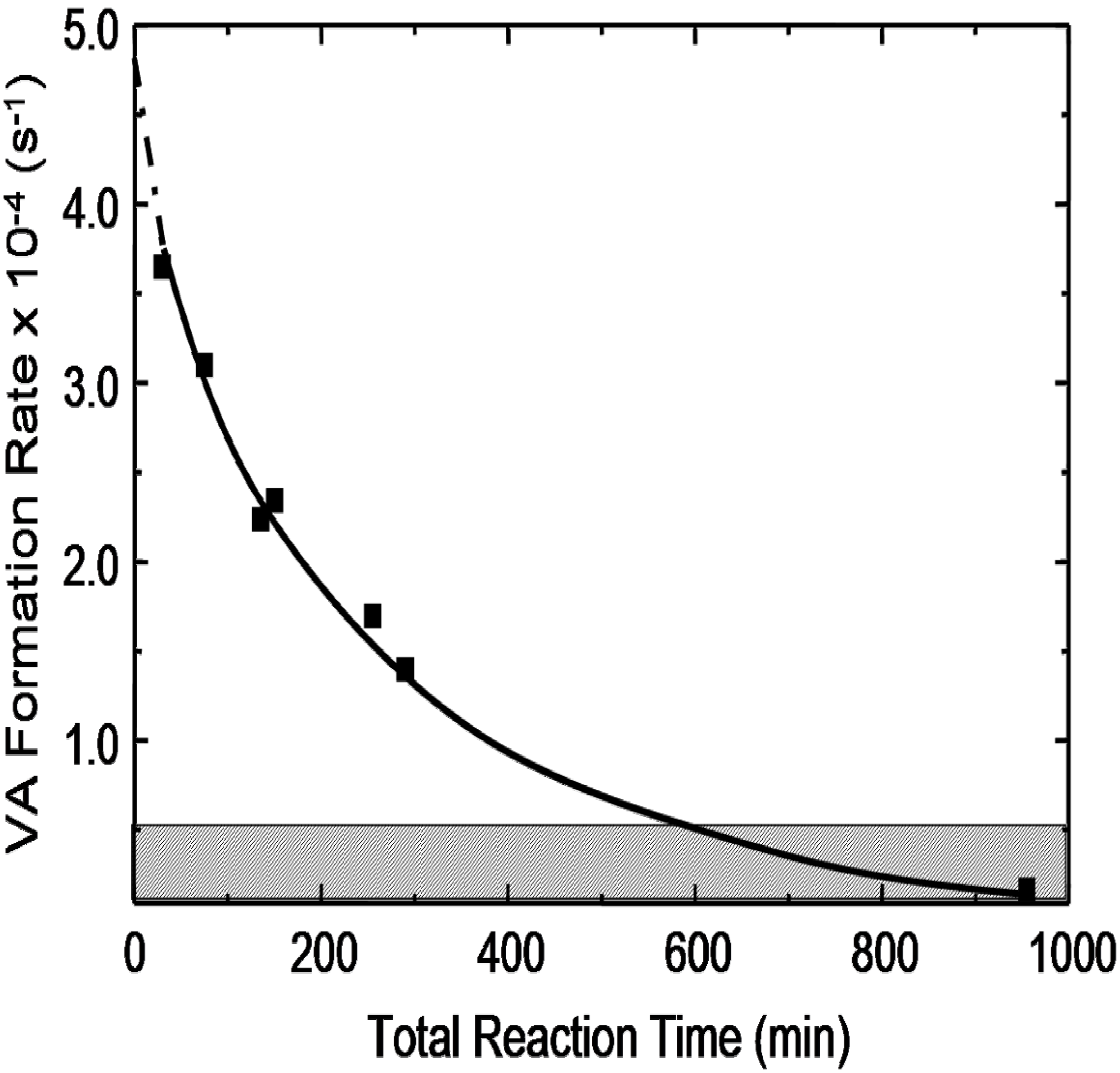

Fig. 66. VA formation rate as a function of time on 0.5 ML Sn/4.0 ML Pd/Rh(100) annealed to 600 K for 60 sec. Reaction at 450 K; p_{O_2} = 2.0 Torr; $p_{C_2H_4}$ = 9.0 Torr; p_{AcOH} = 4.0 Torr.

Due to extremely high density of Pd monomer pairs the initial activity was expected to be much higher than that on Pd/Rh(100). However, on a per pair basis, the rates turn out to be close. The discrepancy might be because of the fact that although the geometric or ensemble effects are favorable for the formation of VA due to the presence of Sn, the ligand effects or the electronic effects might be effectively decreasing the reaction rate. As we have mentioned earlier the ideal distance between Pd monomer sites for VA coupling is 3.3 Å (Fig. 60) [155]. The spacing provided by Sn on Pd is 3.89 Å. The deposition of Pd on Au(100) and Au(111) and annealing to 600 K on the other hand provides a distance of 4.08 and 4.99 Å, respectively between the monomer pairs. The ensemble or the geometric effects although are not very favorable for the Pd-Au systems, the electronic or the ligand effects seem to play some role in enhancing the reaction rate. These latter effects, in case of Pd-Sn are not conducive for the formation of VA.

Another reason for the loss of activity is because of the nature of Sn which is not very resistive to oxidation. Lee and Lambert [169] studied the formation of Sn oxide films from Sn overlayers and the structure and stability of these films on Pd(111) and concluded that both submonolayer and multilayer Sn depositions are not resistive to oxidation. Submonolayer Sn though is oxidized slowly than multilayer films, the former get oxidized much more. The Sn films get oxidized very fast at an exponential rate and at our pressures with the partial pressure of O_2 at 2.0 Torr we would expect a significant oxidation with in 3-4 hours of reaction time based upon their data. We have observed that after reaction the Sn 3d XPS peak becomes a little broader implying the formation of surface Sn oxides which is in agreement with the observations of Lee and Lambert [169]. Meanwhile no changes in the peaks of Pd 3d XPS were observed after reaction reflecting the fact that Pd does not seem to be oxidized. The oxidation of Sn on the other hand may significantly block the adsorption of acetate and ethylene species on the neighboring Pd atoms. Also these Sn oxides are very stable at least up to 700 K [169]. After reaction some decrease in the ratio of Sn/Pd is observed and in the present scenario this might imply that Pd and Sn phase separate or during the reaction islands of Sn and Pd are formed. Légaré et al [170] have addressed the formation of islands of metal substrates and oxide thin films due to oxidation of Al/Pd interface and the same has been proposed for Sn/Pd(111) interfaces [169]. Thus, the overall activity of Sn-Pd system would decrease due to the decrease in the density of the Pd monomer pairs on the surface. The disruptions in the c(2 x 2) structure and the formation of Sn islands implies the formation of contiguous Pd atoms which are not as active as separated isolated Pd monomer for this reaction.

SUMMARY

Vinyl acetate reaction is an important commercial reaction. Although the VA synthesis procedure has been established and being used industrially with great efficiency, questions regarding the role of the additives, the nature of the active sites and the mechanism still remain. The primary objective of this research was to use model catalysts, such as, single crystals, bimetallic alloy films, to replicate the complex properties of heterogeneous Pd-Au catalysts used in industry. The goal of this study was to acquire a fundamental understanding of the VA reaction mechanism by carrying out detailed kinetic and spectroscopic investigations over model catalysts and supported Pd catalysts, and to detail the role of alloying in optimizing the selectivity of this important industrial reaction.

Supported catalysts, 1 wt% Pd/SiO_2 and 5 wt% Pd/SiO_2, and 1 wt% Pd–0.5 wt% Au/SiO_2, were prepared by an incipient wet-impregnation method and characterized using XRD and TEM. On Pd-only catalysts the reaction rates were found to be: Pd(100) < 5 wt% Pd/SiO_2 ($d_{pd} = 4.2$ nm) < 1 wt% Pd/SiO_2 ($d_{pd} = 2.5$ nm). Particle size-dependence of the reaction rates is evident for the Pd-only catalysts, which suggests a degree of structure sensitivity of the reaction. There is an increased availability of uncoordinated, edge atoms on small particles. With a Pd single crystal, fewer less-coordinated surface sites are present compared to a comparable area on a small Pd particle on a supported Pd catalyst.

The formation of Pd carbide (PdC_x) during the synthesis of VA was investigated over Pd/SiO_2 catalysts with two different Pd particle sizes, as well as over a Pd-Au/SiO_2 mixed-metal catalyst. XRD data show that PdC_x was produced in the pure Pd catalysts after reaction based on the downshift of the Pd (111) and (200) XRD features. The smaller Pd particles showed greater

resistance to the formation of PdC_x. The XRD and XPS data are consistent with formation of a PdC_x species at the surface of the Pd-Au catalyst, however, the primary contributor to the downshift of the Pd(111) feature subsequent to reaction in the mixed-metal catalyst is believed to arise from reaction-induced alloying of Au with Pd. The alloying of Au with Pd is apparently very effective in preventing PdC_x formation in Pd-based catalysts for VA synthesis.

LEISS was used to understand the surface versus bulk composition for Pd-Au surfaces. Using IRAS and CO as a probe molecule Au has been identified to isolate Pd on the surface into a monomer Pd site ($PdAu_6$ for Pd-Au bimetal on Mo(110) and for Pd/Au(111) and $PdAu_4$ for Pd/Au(100)) which has been proposed to be the active site for the formation of VA. A pair of such isolated Pd monomers is required for the adsorption of acetic acid and ethylene, and the distance between the constituent monomers is crucial. Hence, Au while separating Pd on the surface into a monomer site also reduces the formation of unwanted surface species and products, such as, CO, CO_2 and surface carbon.

The synthesis of VA on Sn/Pd/Rh(100) at 15 Torr and 450 K was investigated by varying the amount of Sn deposited on Pd/Rh(100) substrate. We have identified that the maximum production rate of VA happens at about 0.5 monolayer coverage of Sn. At this coverage of Sn the Pd and Sn atoms are in c(2 x 2) geometry as indicated by low energy electron diffraction (LEED) spectroscopy. Utilization of Pd-Sn surfaces for the formation of VA thus confirms the idea that a pair of isolated Pd monomers is the active site for this reaction. In this study it has been demonstrated that the complexity of industrial catalysts can be simplified into manageable steps by integrating the modern ultrahigh vacuum surface science and kinetic studies of heterogeneous catalysts.

REFERENCES

[1] C.R. Henry, Surf. Sci. Rep. 31 (1998) 235.

[2] G.A. Somorjai, in: *Introduction to Surface Chemistry and Catalysis*, (Wiley, New York 1994).

[3] G.A. Somorjai and M. Yang, Topics in Catal. 24 (2003) 61.

[4] J. Libuda and H.-J. Freund, Surf. Sci. Rep. 57 (2005) 157.

[5] G.A. Somorjai and K.R. McCrea, Appl. Catal. A 222 (2001) 3.

[6] D.W. Goodman, J. Vac. Sci. & Technol. 20 (1982) 522.

[7] D.W. Goodman, Surf. Sci. 300 (1994) 837.

[8] D.W. Goodman, J. Phys. Chem. 100 (1996) 13090.

[9] H.J. Freund, M. Baumer and H. Kuhlenbeck, Adv. Catal., 45 (2000) 333.

[10] G.A. Somorjai, Catal. Today 12 (1992) 343.

[11] G.A. Somorjai, Appl. Surf. Sci. 121 (1997) 1.

[12] D.W. Goodman, J. Catal. 216 (2003) 213.

[13] J.A. Rodriguez and D.W. Goodman, Surf. Sci. Rep. 14 (1991) 1.

[14] D.W. Goodman, Surf. Rev. Lett. 2 (1995) 9.

[15] M. Baumer and H.-J. Freund, Prog. Surf. Sci. 61 (1999) 127.

[16] D.W. Goodman, Acc. Chem. Res. 17 (1984) 194.

[17] D.W. Goodman, Annu. Rev. Phys. Chem. 37 (1986) 425.

[18] J.H. Sinfelt, Acc. Chem. Res. 10 (1977) 15.

[19] C.T. Campbell, Annu. Rev. Phys. Chem. 41 (1990) 775.

[20] J.A. Rodriguez and D.W. Goodman, J. Phys. Chem. 95 (1991) 4196.

[21] J.A. Rodriguez, R.A. Campbell and D.W. Goodman, J. Phys. Chem. 95 (1991) 5716.

[22] J.A. Rodriguez, R.A. Campbell and D.W. Goodman, J. Vac. Sci. Technol. A 9 (1991) 1698.

[23] J.A. Rodriguez, R.A. Campbell and D.W. Goodman, J. Vac. Sci. Technol. A 10 (1992) 2540.

[24] J.A. Rodriguez and D.W. Goodman, Science 257 (1992) 897.

[25] J.A. Rodriguez, R.A. Campbell and D.W. Goodman, Surf. Sci. 309 (1994) 377.

[26] R. Franchy, Surf. Sci. Rep. 38 (2000) 199.

[27] H.-J. Freund, H. Kuhlenbeck and V. Staemmler, Rep. Prog. Phys. 59 (1996) 283.

[28] S.A. Chambers, Surf. Sci. Rep. 39 (2000) 105.

[29] A.K. Santra and D.W. Goodman, J. Phys.-Condensed Matter 15 (2003) R31.

[30] P.J. Chen and D.W. Goodman, Surf. Sci. 312 (1994) L767.

[31] X. Lai, C.C. Chusuei, K. Luo, Q. Guo and D.W. Goodman, Chem. Phys. Lett. 330 (2000) 226.

[32] M.C. Wu and D.W. Goodman, J. Phys. Chem. 98 (1994) 9874.

[33] J.W. He, X. Xu, J.S. Corneille and D.W. Goodman, Surf. Sci. 279 (1992) 119.

[34] A.K. Santra, B.K. Min and D.W. Goodman, Surf. Sci. 515 (2002) L475.

[35] T. Schroeder, M. Adelt, B. Richter, M. Naschitzki, M. Baumer and H.J. Freund, Surf. Rev. Lett. 7 (2000) 7.

[36] X.P. Xu and D.W. Goodman, Appl. Phys. Lett. 61 (1992) 1799.

[37] M.C. Wu, J.S. Corneille, C.A. Esrade, J.W. He and D.W. Goodman, Chem. Phys. Lett. 182 (1991) 472.

[38] M.C. Wu and D.W. Goodman, Catal. Lett. 15 (1992) 1.

[39] M.C. Wu, C.M. Truong, K. Coulter and D.W. Goodman, J. Am. Chem. Soc. 114 (1992) 7565.

[40] M.C. Wu, J.S. Corneille, J.W. He, C.A. Esrade and D.W. Goodman, J. Vac. Sci. Technol. A 10 (1992) 1467.

[41] J.S. Corneille, J.W. He and D.W. Goodman, Surf. Sci. 306 (1994) 269.

[42] M.C. Wu, C.M. Truong and D.W. Goodman, J. Phys. Chem. 97 (1993) 4182.

[43] M.C. Wu, C.M. Truong and D.W. Goodman, J. Phys. Chem. 97 (1993) 9425.

[44] C.M. Truong, M.C. Wu and D.W. Goodman, J. Chem. Phys. 97 (1992) 9447.

[45] C.M. Truong, M.C. Wu and D.W. Goodman, J. Am. Chem. Soc. 115 (1993) 3647.

[46] B. Cho, E. Choi, S. Chung, K. Kim, T. Kang, C. Park and B. Kim, Surf. Sci. 439 (1999) L799.

[47] J.U. Shin, D.J. Kim, S.H. Park, Y.T. Han, H.K. Sung, J. Kim and S.J. Park, Etri Journal 24 (2002) 398.

[48] Q.Z. Dong, J.D. Hu, Z.X. Guo, J.S. Lian, J.W. Chen and B. Chen, Appl. Surf. Sci. 202 (2002) 114.

[49] W.S. Oh, C. Xu, D.Y. Kim and D.W. Goodman, J. Vac. Sci. Technol. A 15 (1997) 1710.

[50] Q. Guo, S. Lee and D.W. Goodman, Surf. Sci. 437 (1999) 38.

[51] J.S. Corneille, J.W. He and D.W. Goodman, Surf. Sci. 338 (1995) 211.

[52] C. Lemire, R. Meyer, V.E. Henrich, S. Shaikhutdinov and H.J. Freund, Surf. Sci. 572 (2004) 103.

[53] R. Meyer, S.K. Shaikhutdinov and H.J. Freund, Zeitschrift fur Physikalische Chemie-Inter. J. Res. Phys. Chem. Chem. Phys. 218 (2004) 905.

[54] I.I. Moiseev, M.N. Vargaftic and Ya.K. Syrkin, Dokl. Akad. Nauk Az. SSR 133 (1960) 377.

[55] E.A. Crathorne, D. MacGowan, S.R. Morris and A.P. Rawlinson, J. Catal. 149 (1994) 254.

[56] US Patent 3743607, (1973).

[57] US Patent 3775342, (1973).

[58] US Patent 3969271, (1976).

[59] US Patent 3658888, (1972).

[60] US Patent 4048096, (1977).

[61] D.D. Kragten, R.A. van Santen, M.K. Crawford, W.D. Provine and J.J. Lerou, Inorg. Chem. 38 (1999) 331.

[62] I.I. Moiseev, T.A. Stromnova, M.N. Vargaftig and G. Ja Mazo, J. Chem. Comm. 956 (1978) 27.

[63] B. Samanos, P. Boutry and R. Montarna, J. Catal. 23 (1971) 19.

[64] P.M. Henry and R.N. Pandey, Adv. Chem. Ser. 132 (1974) 33.

[65] M. Neurock, W.D. Provine, D.A. Dixon, G.W. Coulston, J.J. Lerou and R.A. Van santen, Chem. Eng. Sci. 51 (1996) 1691.

[66] S. Nakamura and T. Yasui, J. Catal. 23 (1971) 315.

[67] D. Stacchiola, F. Calaza, F. Burkholder and W.T. Tysoe, J. Am. Chem. Soc. 126 (2004) 15384.

[68] N. Macleod, J.M. Keel and R.M. Lambert, Appl. Catal. A 261 (2004) 37.

[69] W.D. Provine, P. Mills and J.J. Lerou, Stud. Surf. Sci. Catal. 101 (1996) 191.

[70] K.W. Kolasinski, in: *Surface Science: Foundations of Catalysis and Nanoscienc*, (Wiley, West Sussex, 2002).

[71] D.P. Woodruff and T.A. Delchar, in: *Modern Techniques of Surface Science-Second Edition. Cambridge Solid State Science Series*, (Cambridge University Press, Cambridge, 1994).

[72] I. Chorkendorff and J.W. Niemantsverdriet, in: *Concepts of Modern Catalysis and Kinetics*, (Wiley-VCH, Weinheim, 2003).

[73] J.W. Niemantsverdriet, in: *Spectroscopy in Catalysis*, (Wiley-VCH, New York, 1993).

[74] E. Taglauer, J. du Plessis and G.N. van Wyk, in: *Surface Science Principles and Applications*, (Springer, Berlin, 1996).

[75] B.E. Hayden, in: *Reflection Absorption Infrared Spectroscopy*, (Plenum Press, New York, 1987).

[76] H. Niehus, W. Heiland and E. Taglauer, Surf. Sci. Rep. 17 (1993) 213.

[77] Y.F. Han, D. Kumar, C. Sivadinarayana, A. Clearfield and D.W. Goodman, Catal. Lett. 94 (2004) 131.

[78] Y.F. Han, D. Kumar and D.W. Goodman, J. Catal. 230 (2005) 353.

[79] Y.-F. Han, D. Kumar, C. Sivadinarayana and D.W. Goodman, J. Catal. 224 (2004) 60.

[80] Y.F. Han, J.H. Wang, D. Kumar, Z. Yan and D.W. Goodman, J. Catal. 232 (2005) 467.

[81] S. Nakamura and T. Yasui, J. Catal. 17 (1970) 366.

[82] G. Bergeret and P. Gallezot, in: *Handbook of Heterogeneous Catalysts*, (Wiley-VCH, Weinheim, 1997).

[83] S.M. Augustine and J.P. Blitz, J. Catal. 142 (1993) 312.

[84] D. Kumar, Y.-F. Han, M.S. Chen and D.W. Goodman, Catal. Lett. 106 (2006) 1.

[85] A.H. Zaidi, Appl. Catal. 30 (1987) 131.

[86] J.A. Mc Caulley, J. Phys. Chem. 97 (1993) 10372.

[87] S.B. Ziemecki, G.A. Jones, D.G. Swartzfager, R.L. Harlow and J. Faber Jr., J. Am. Chem. Soc. 107 (1985) 4547.

[88] M. Bonarowska, J. Pielaszek, V.A. Semikolenov and Z. Karpinski, J. Catal. 209 (2002) 528.

[89] Z. Kaszkur, J. Appl. Cryst. 33 (2000) 87.

[90] Z. Kaszkur, J. Appl. Cryst. 33 (2000) 1262.

[91] S.B. Ziemecki and G.A. Jones, J. Catal. 95 (1985) 621.

[92] R.K. Nandi, R. Pitchai, S.S. Wong, J.B. Cohen, R.L. Burwell Jr. and J.B. Butt, J. Catal. 70 (1981) 298.

[93] T. Yamamoto, M. Adachi, K. Kawabata, K. Kimura and H.W. Hahn, Appl. Phys. Lett. 63 (1993) 3020.

[94] J.A. Mc Caulley, Phys. Rev. B 47 (1993) 4873.

[95] K. Okitsu, Y. Mizukoshi, H. Bandow, T.A. Yamamoto, Y. Nagata and Y. Maeda, J. Phys. Chem. B 101 (1997) 5470.

[96] A. Sarkany, Appl. Catal. A: General 175 (1998) 245.

[97] M. Bonarowska, A. Malinowski, W. Juszczyk and Z. Karpinski, Appl. Catal. B 30 (2001) 187.

[98] Z. Kaszkur, J. Stachurski and J. Pielaszek, J. Phys. Chem. Solids 47 (1986) 795.

[99] C. Xu, X. Lai, G.W. Zajac and D.W. Goodman, Phys. Rev. B 56 (1997) 13464.

[100] Y.Q. Cai, A.M. Bradshaw, Q. Guo and D.W. Goodman, Surf. Sci. 399 (1998) L357.

[101] M. Frank and M. Baumer, Phys. Chem. Chem. Phys. 2 (2000) 3723.

[102] M. Frank, M. Baumer, R. Kuhnemuth and H.-J. Freund, J. Vac. Sci. Technol. 19 (2001) 1479.

[103] C.G. Vayenas, B. Lee and J. Michaels, J. Catal. 66 (1980) 36.

[104] R.E. Kenson and M. Lapkin, J. Phys. Chem. 74 (1970) 1493.

[105] J. Barbier Jr. and D. Duprez, Appl. Catal. B: Environmental 4 (1994) 105.

[106] J.T. Kummer, J. Phys. Chem. 90 (1986) 4747.

[107] J.M.A. Harmsen, J.H.B. Hoebink and J.C. Schouten, Ind. Eng. Chem. Res. 39 (2000) 599.

[108] C. Pliangos, I.V. Yentekakis, V.G. Papadakis, C.G. Vayenas and X.E. Verykios, Appl. Catal. B: Environmental 14 (1997) 161.

[109] X.C. Guo and R.J. Madix, J. Am. Chem. Soc. 117 (1995) 5523.

[110] M. Bowker, C. Morgan, N. Perkins, R. Holroyd, E. Fourre, F. Grillo and A. Mac Dowall, J. Phys. Chem. B 109 (2005) 2377.

[111] Z. Bastl and T. Sarapatka, Collect. Czech. Chem. Commun. 63 (1998) 1793.

[112] C. D. Wagner, W. M. Riggs, L. E. Davis, J. F. Moulder and G. E. Muilenberg (Ed.), in: *Handbook of X-ray Photoelectron Spectroscopy*, (Perkin-Elmer Corporation, Physical Electronics Division, 1979).

[113] M. Sock, A. Eichler, S. Surney, J.N. Andersen, B. Klötzer, K. Hayek, M.G. Ramsey and F.P. Netzer, Surf. Sci. 545 (2003) 122.

[114] I.Z. Jones, R.A. Bennett and M. Bowker, Surf. Sci. 439 (1999) 235.

[115] J.N. Andersen, M. Qvarford, R. Nyholm, S.L. Sorensen and C. Wigren, Phys. Rev. Lett. 67 (1991) 2822.

[116] E.M. Stuve, R.J. Madix and C.R. Brundle, Surf. Sci. 146 (1984) 155.

[117] M. Bowker, C. Morgan and J. Couves, Surf. Sci. 555 (2004) 145.

[118] R.D. Haley, M.S. Tikhov and R.M. Lambert, Catal. Lett. 76 (2001) 125.

[119] D. Kumar, Y.-F. Han and D.W. Goodman, In Preparation.

[120] D. Stacchiola and W.T. Tysoe, Surf. Sci. 513 (2002) L431.

[121] J.A. Gates and L.L. Kesmodel, Surf. Sci. 120 (1982) L461.

[122] P. Cremer, X. Su, Y. Shen and G.A. Somarjai, Catal. Lett. 40 (1996) 43.

[123] S.K. Shaikhutdinov, M. Heemeier, M. Baumer, T. Lear, D. Lennon, R.J. Oldman, S.D. Jackson and H.-J. Freund, J. Catal. 200 (2001) 330.

[124] Q. Smejkal, D. Linke, U. Bentrup, M.-M. Pohl, H. Berndt, M. Baerns and A. Bruckner, Appl. Catal. A 268 (2004) 67.

[125] S.M. Foiles, J. Vac. Sci. Technol., A 5 (1987) 889.

[126] D.G. Swartzfager, S.B. Ziemecki and M.J. Kelly, J. Vac. Sci. Technol. 19 (1981) 185.

[127] P. Varga and G. Hetzendorf, Surf. Sci. 162 (1985) 544.

[128] A. Jablonski, S.H. Overbury and G.A. Somarjai, Surf. Sci. 65 (1977) 578.

[129] J.H. Sinfelt, in: *Bimetallic Catalysts: Discoveries, Concepts and Applications*, (Wiley, New York, 1983).

[130] R.L. Moss and L. Whally, in: *Advances in Catalysis*, (Academic Press, New York, 1972).

[131] V. Ponec, Adv. Catal. 32 (1983) 149.

[132] R. Abel, P. Collins, K. Eichler, I. Nicolau and D. Peters,1997) 2298.

[133] E.G. Allison and G.C. Bond, Catal. Rev. 7 (1972) 233.

[134] P.N. Rylander, in: *Catalytic Hydrogenation in Organic Synthesis*, (Academic Press, London, 1979).

[135] A.M. Venezia, V. La Parola, B. Pawelec and J.LG. Fierro, Appl. Catal. A 264 (2004) 43.

[136] D.L. Trimm and Z.I. Onsan, Catal. Rev. 43 (2001) 31.

[137] A. Maeland and T.B. Flanagan, Can. J. Phys. 42 (1964) 2364.

[138] A. Couper and D.D. Eley, Discussions Faraday Soc. 8 (1950) 172.

[139] C.J. Baddeley, R.M. Ormerod, A.W. Stephenson and R.M. Lambert, J. Phys. Chem. 99 (1995) 5146.

[140] D.D. Eley and P. Luetic, Trans. Faraday Soc. 53 (1957) 1483.

[141] G. Reinacker and S. Engels, Z. Anorg. Allg. Chem. 336 (1965) 259.

[142] W.M.H. Sachtler and P. van Der Planck, Surf. Sci. 18 (1969) 62.

[143] M. Mavrikakis, B. Hammer and J.K. Norskov, Phys. Rev. Lett. 81 (1998) 2819.

[144] K. Luo, T. Wei, C.W. Yi, S. Axnanda and D.W. Goodman, J. Phys. Chem. B 109 (2005) 23517.

[145] C.-W. Yi, K. Luo, T. Wei and D.W. Goodman, J. Phys. Chem. B 109 (2005) 18535.

[146] M. Aschoff, S. Speller, J. Kuntze, W. Heiland, E. Platzgummer, M. Schmid, P. Varga and B. Baretzky, Surf. Sci. 415 (1998) L1051.

[147] M. Aschoff, G. Piaszenski, S. Speller and W. Heiland, Surf. Sci. 402-404 (1998) 770.

[148] H. Niehus, Phys. Status Solidi B 192 (1995) 357.

[149] S. Schomann and E. Taglauer, Surf. Rev. Lett. 3 (1996) 1823.

[150] L. Houssiau and P. Bertrand, Nucl. Instrum. Methods B 125 (1997) 328.

[151] B.E. Koel, A. Sellidj and M.T. Paffett, Phys. Rev. B. 46 (1992) 7846.

[152] A.W. Stephenson, C.J. Baddeley, M.S. Tikhov and R.M. Lambert, Surf. Sci. 398 (1998) 172.

[153] F. Maroun, F. Ozanam, O.M. Magnussen and R.J. Bhem, Science 293 (2001) 1811.

[154] M.S. Chen, K. Luo, T. Wei, Z. Yan, D. Kumar, C.-W. Yi and D.W. Goodman, Catal. Today Submitted (2006)

[155] M.S. Chen, D. Kumar, C.W. Yi and D.W. Goodman, Science 310 (2005) 291.

[156] D.C. Meier and D.W. Goodman, J. Am. Chem. Soc. 126 (2004) 1892.

[157] K. Luo, T. Wei, C.W. Yi, S. Axnanda and D.W. Goodman, J. Phys. Chem. B 109 (2005) 23517.

[158] L. Hilaire, P. Legare, Y. Holl and G. Maire, Surf. Sci. 103 (1981) 125.

[159] D. Stacchiola, F. Calaza, F. Burkholder, A.W. Schwabacher, M. Neurock and W.T. Tysoe, Chem. Int. Ed. 44 (2005) 4572.

[160] M. Neurock, J. Catal. 216 (2003) 73.

[161] A.F. Lee, C.J. Baddeley, M.S. Tikhov and R.M. Lambert, Surf. Sci. 373 (1997) 195.

[162] N. Tsud, T. Skala, F. Sutata, K. Veltruska, V. Dudr, S. Fabik, L. Sedlacek, V. Chab, K.C. Prince and V. Matolin, Surf. Sci. 595 (2005) 138.

[163] A.F. Lee, C.J. Baddeley, C. Hardacre, G.D. Moggridge, R.M. Ormerod, R.M. Lambert, J.P. Candy and J.-M. Basset, J. Phys. Chem. B 101 (1997) 2979.

[164] M. Batzill, D.E. Beck and B.E. Koel, Surf. Sci. 466 (2000) L821.

[165] J.M. Peck, D.I. Mahon and B.E. Koel, Surf. Sci. 410 (1998) 200.

[166] C. Panja, N.A. Saliba and B.E. Koel, J. Phys. Chem. B 105 (2001) 3786.

[167] T. Wei, K. Luo, S. Axnanda and D.W. Goodman, In Preparation.

[168] K. Luo, T. Wei, S. Axnanda and D.W. Goodman, In Preparation.

[169] A.F. Lee and R.M. Lambert, Phys. Rev. B. 58 (1998) 4156.

[170] P. Legare, F. Finck, R. Roche and G. Maire, Surf. Sci. 217 (1989) 167.

VITA

Dheeraj Kumar was born in Nizamabad, India on September 27, 1977. He graduated from St. Francis de sales Boys High School (High School) in 1993 and from Government Junior College (College) in 1995 to gain admission in Indian Institute of Technology, Bombay. There he joined the Department of Chemistry and graduated in 2001 with B.S. and M.S. degrees. He started his graduate studies in the Department of Chemistry at Texas A&M University in 2001 under the direction of Dr. D. Wayne Goodman and received his Ph. D. in chemistry in August 2006. Dheeraj is married to Charu Agrawal. His hobbies include badminton, table tennis, music and books. His permanent address is:

Dheeraj Kumar,
H. No. 11-1-2/137,
New NGO’s Colony,
Nizamabad,
Andhra Pradesh, India, 503002.